STRUCTURAL INSIGHTS INTO THE ROLE OF THE PROLINE RICH REGION IN TAU FUNCTION WITH TUBULIN AND MICROTUBULES

Karen Acosta

A DISSERTATION

In

Biochemistry and Molecular Biophysics

Presented to the Faculties of the University of Pennsylvania

in

Partial Fulfillment of the Requirements for the

Degree of Doctor of Philosophy

2024

Supervisor of Dissertation
Elizabeth Rhoades, PhD
Associate Professor of Chemistry, University of Pennsylvania

Graduate Group Chairperson
Kim Sharp, PhD
Associate Professor of Biochemistry and Biophysics, University of Pennsylvania

Dissertation Committee
Harry Ischiropoulos, PhD – Research Professor of Pediatrics, University of Pennsylvania
Ronen Marmorstein, PhD – George W. Raiziss Professor, University of Pennsylvania
Kelvin Luk, PhD – Research Associate Professor of Pathology, University of Pennsylvania
Peter Baas, PhD – Professor of Neurobiology and Anatomy, Drexel University

ACKNOWLEDGEMENTS

It cannot be overstated that the graduate school experience is not only shaped by the physical time in the lab, whether it be running experiments, or trying to catch up on your lab notebook, etc., but by the people who support you – especially when those experiments fail. For that, I feel so fortunate to have had so many people who came along with me on this journey, regardless of however long or short their stay was in my grad school story.

First, it should go without saying that I would like to thank Dr. Liz Rhoades for her mentorship, which was truly invaluable, particularly given the challenges posed by a 'once in a lifetime' pandemic. Over the years I've also appreciated the advice from my dissertation committee members and for the chair of my committee, Dr. Harry Ischiropoulos, who made it a point to check in on the person behind the 'PhD candidate' after every committee meeting.

I am grateful for Rhoades lab members both past and present for their support in the lab, providing advice, or simply taking a quick break for coffee or a 'fun drink' to catch some sunshine or a pick-me-up. Additionally, to Dr. Sanjula Wickramasinghe and Jenny Ramirez who have become great friends from lab, despite having to endure my sporadic rants.

To the lifelong friendships: for my rock climbing buddies Dr. Sanjula Wickramasinghe, Dr. Leann Miles, Dr. Kiara Berrios, and Iliana Hernandez; and even for those who don't climb, Adriana Naomi Santiago Ruiz, Dr. Adriana Alire, and Kelsey Montoya thanks for all the memories.

Finally, for my unapologetically loud, sometimes embarrassing, and utterly encouraging family – I wouldn't have it any other way. A special thanks to my mom and brother for their never-ending support and encouragement.

ABSTRACT

STRUCTURAL INSIGHTS INTO THE ROLE OF THE PROLINE RICH REGION IN TAU FUNCTION WITH TUBULIN AND MICROTUBULES

Karen Acosta

Elizabeth Rhoades

Tau is a microtubule-associated protein thought to function in the regulation of microtubule stability and dynamics. Normally, tau plays an important role in modulating axonal microtubules in neurons, where it is highly expressed. Intracellular tau aggregates are found in a broad class of disorders, including Alzheimer's Disease, termed tauopathies. As an intrinsically disordered protein, tau lacks stable secondary and tertiary structure, and this structural disorder is maintained even when binding to soluble tubulin and microtubules. Multiple tau-tubulin binding sites have also been identified, spanning the proline-rich region (PRR), microtubule binding repeats (MTBR: R1–R4), and pseudo-repeat, R′. Although dozens of post-translational modifications have been identified on tau, phosphorylation, and specifically hyperphosphorylation, of tau is correlated with disease and alterations to microtubule binding. Intriguingly, potential phosphorylation sites also cluster with high frequency within the PRR. Here, we use single-molecule spectroscopy and structural mass spectrometry techniques to characterize the impact of phosphomimic mutations in the PRR on tubulin binding and probe the structure of the PRR-tubulin complex. We find that phosphomimics cumulatively diminish tubulin binding and slow microtubule polymerization. Additionally, we map two ~15 residue regions of the PRR as primary tubulin binding sites and

propose a model in which PRR enhances lateral interactions between tubulin dimers, complementing the longitudinal interactions observed for MTBR. Together these measurements provide insight into the previously overlooked relevance of tau's PRR in functional interactions with tubulin.

TABLE OF CONTENTS

LIST OF TABLES

LIST OF FIGURES

CHAPTER 4: PRR INTERACTS PREDOMINANTLY WITH THE α-TUBULIN SUBUNIT

CHAPTER 5: CONCLUSIONS AND PERSPECTIVES

APPENDIX: SMALL MOLECULES DEM AND RO INHIBIT ALPHA-SYNUCLEIN OLIGOMERS BUT NOT MONOMER PROTEIN

LIST OF ABBREVIATIONS

AD	Alzheimer's Disease
Amp	ampicillin
ATP	adenosine triphosphate
$CaCl_2$	calcium chloride
DSBU	disuccinimidyl dibutyric urea
DTT	dithiothreitol
EGTA	ethylene glycol-bis(β-aminoethyl ether)-N,N,N',N'-tetraacetic acid
ET_{eff}	energy transfer efficiency
FCS	fluorescence correlation spectroscopy
FRET	Förster resonance energy transfer
HCl	hydrochloric acid
GDP	guanosine-5'-diphosphate
GTP	guanosine-5'-triphosphate
IDP	intrinsically disordered protein
IDR	intrinsically disordered region
IPTG	isopropyl β-D-1-thiogalactopyranoside
KCl	potassium chloride
KH_2PO_4	potassium dihydrogen phosphate
LB	Luria broth
MAP	microtubule associated protein
MEM	Eagle′s minimum essential medium
$MgCl_2$	magnesium chloride
$MgSO_4$	magnesium sulfate
MS	mass spectrometry
MWCO	molecular weight cut off
NA	numerical aperture
NaCl	sodium chloride
Na_2HPO_4	disodium phosphate
Ni-NTA	nitrilotriacetic acid
PEG-PLL	(ethylene glycol)poly(L-lysine)
PIE-FRET	pulsed interleaved excitation Förster resonance energy transfer
PIPES	2,2'-piperazine-1,4-diylbisethanesulfonic acid
PMSF	phenylmethylsulfonyl fluoride
PTM	post-translational modification
SDS-PAGE	sodium dodecyl sulfate-polyacrylamide gel electrophoresis
smFRET	single molecule Förster resonance energy transfer
TCEP	tris(2-carboxyethyl)phosphine
TEV	Tobacco etch virus
2N4R	full length tau
MTBR	microtubule binding region
PRR	proline rich region

CHAPTER 1: INTRODUCTION

1.1 Intrinsically Disordered Proteins

For decades the scientific community operated on the assumption that the unique three-dimensional structure of a protein, derived from its amino acid sequence, would directly shape and predict biological function [1, 2]. Although functional unstructured proteins had been proposed [3], this structure-function paradigm remained largely unchallenged. That is, until the identification of p21, which both lacked a stable secondary structure in solution yet functions to bind and inhibit Cdk2 in the cell cycle [4]. This protein, p21, amongst others would later be classified into a sub-group of proteins termed intrinsically disordered proteins (IDPs) due to their lack of stable secondary or tertiary structures in solution despite being biologically active.

Since their discovery, a large variety of IDPs and intrinsically disordered regions (IDRs) within ordered proteins have been observed. In fact, IDPs/IDRs are present across several kingdoms from viruses and bacteria to multicellular organisms [5]. Intriguingly, the frequency of disordered proteins in the proteome also increases with organism complexity [6] suggesting that there is a relationship between disorder and functional complexity.

Although an overwhelming >40% of the mammalian proteome is estimated to comprise of IDPs or contain an IDR [7], these disordered sequences do share a number of characteristics. Namely, disordered amino acid sequences typically have more polar and charged residues (Arg, Pro, Gln, Gly, Glu, Ser, Ala, and Lys) and fewer “order-promoting” amino acids (Trp, Cys, Tyr, Ile, Phe, Val, Asn, and Leu) [5]. IDPs also commonly include repeats, especially when compared to ordered proteins [8, 9]. Due to the presence of multiple, (often repeating) charged groups, these regions tend to resist forming a hydrophobic core as those in globular, folded structures and instead

adopt a more extended conformation [10]. These features ultimately create dynamically disordered regions and proteins which exist in conformational flux.

IDP conformational heterogeneity is thought to be vital to their biological function, in part, by permitting interactions with multiple potential binding partners. Infamously, tumor suppressor p53 is able to bind to over a hundred proteins with its disordered region [11]. Nonetheless IDPs have been shown to be involved in a number of different processes including the regulation of cell signaling pathways [12], macromolecular machinery such as ribosomes [13], and the controlled assembly and disassembly of cytoskeletal components like microtubules [14].

Despite their biological relevance, these transient conformations are extremely sensitive to environmental conditions and their intrinsic heterogeneity make studying these interactions more technically challenging. Traditional structural techniques often rely on ordered structures, as in x-ray crystallography, which inherently contradict the properties that make IDPs a unique, yet important subclass of proteins. Although cryo-electron microscopy (cryo-EM) is better able to visualize mobile protein domains, co-populated states and certain disordered regions are still not able to be resolved [15]. Conversely Nuclear Magnetic Resonance (NMR) is one of the most commonly used techniques to study IDPs due to its ability to detect transient structural elements, such as helices, but is limited to larger protein concentrations to achieve signal that at times averages out the intricacies of the conformational plasticity of IDPs [16]. Single-molecule fluorescence techniques, including fluorescence correlation spectroscopy (FCS) and single molecule Förster Energy Transfer (smFRET), benefit from allowing for measurements with low concentrations of proteins and are capable of recording transient conformations on millisecond timescales [17]. Additionally, structural mass spectrometry (MS) methods have recently risen in prominence for IDP studies because of the ability for techniques like crosslinking MS and

hydrogen-deuterium exchange MS to capture transient interactions even amongst complex mixtures like intact cells and cell lysates [18, 19].

1.2 Tau as an Intrinsically Disordered Protein

In 1975 a heat-stable protein, then designated as tau, copurified with tubulin and was deemed essential for microtubule assembly [20]. However, tau itself is now broadly categorized into four major domains, the N-terminal domain, proline rich region (PRR), microtubule binding region (MTBR), and the C-terminal region. (Figure 1.1). The full-length isoform of tau (2N4R) contains both N-terminal inserts, and all four repeat sequences. In the brain, tau is expressed as six different isoforms which either contain none, one or two N-terminal inserts (0N, 1N, or 2N respectively) and either three or four repeat sequences in the MTBR (3R or 4R respectively). These isoforms of tau are differentially expressed based on brain regions, tissues, cell lines, intracellular compartments and developmental stages [21-26].

Tau is also classified as an intrinsically disordered protein, and thus has many of the characteristics shared amongst IDPs. Tau is a highly polarized, disordered protein as evident through several predictive analysis tools for IDPs. Specifically, as calculated through CIDER, the net charge per residue (NCPR) of tau's N-terminus (approximately the first 120 amino acids) and C-terminus contains a high degree of acidic residues; whereas, the PRR and MTBR are positively charged at neutral pH and have a large number of basic residues [27]. The Hopp-Woods hydrophobicity plot for tau also highlights a hydrophilic N-terminus, and otherwise weakly hydrophobic protein consistent with disordered proteins [28]. Given tau's amino acid sequence, predictive algorithms PONDR VLXT [29, 30] and IUPred [31] also suggest tau is highly disordered except for some potential secondary structure within the MTBR [32].

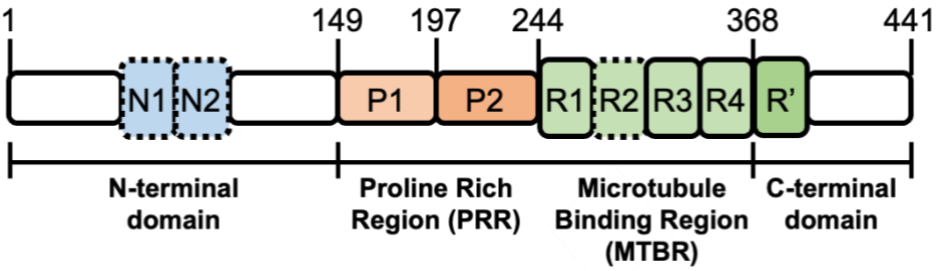

Figure 1.1 Schematic of tau domains.
The longest tau isoform, 2N4R, with each of the major domains labeled: the N-terminal domain containing alternatively spliced N-terminal inserts (N1 and N2, blue), proline-rich region (P1 and P2, orange), microtubule-binding region (MTBR, green) with four repeat regions (R1-R4; R2 may be absent as a result of splicing), and pseudo-repeat (R′), and the C-terminal domain.

Circular dichroism and Fourier transform infrared spectroscopy of tau further confirmed that tau lacks stable secondary or tertiary structure [33]. Several nuclear magnetic resonance (NMR) studies have identified some dynamic, residual secondary structures [34-36]. Namely, transient alpha-helices in the N- and C- terminus (for amino acids 114 – 123, and 428 – 437), polyproline II helices in the PRR (for amino acids 175 – 184, 216 – 223, and 232 – 239), and beta-strands scattered throughout tau (for amino acids 86 – 92, 161 – 166, 224 – 230, 274 – 284, 305 – 315, 336 – 345) [36]. However, subsequent NMR experiments further refine the propensity for these secondary structures and highlight additional regions that do not contain prolines that also show enhanced polyproline II propensities [34].

Experimentally, like other intrinsically disordered proteins, tau maintains an expanded and unfolded structure in solution. Due to the high number of charged and hydrophilic amino acids, tau has no defined radius of gyration and behaves as a random "Gaussian" polymer [33]. However, the mean radius of gyration of tau as evaluated through single molecule Förster resonance energy transfer (smFRET) and small-angle X-ray scattering (SAXS) find that tau is smaller than a random coil of equal length [37, 38]. Shorter tau deletion mutants that still contain the MTBR, are significantly more extended than a random coil, suggesting that despite the extended MTBR, long range contacts between the termini cause the global compaction of tau [37].

Although remaining disordered in solution, several long-range contacts have been identified, including between the N-terminus and PRR [36, 39] and are thought to be mediated at least in part, by electrostatic interactions [34, 36, 40, 41]. These contacts have resulted in the observation of a "paper-clip" like model for tau via smFRET in which the C-terminus is folded towards the MTBR while the N-terminus is in contact with the C-terminus [42]. Further smFRET studies amended this model to indicate a more "S" shaped structure given that the distance between

the MTBR and the N- or C-terminus is smaller than the distance between the termini themselves [43]. However, the behavior of tau domains can be altered by flanking domains, such as the P2-MTBR (K16) which becomes more compact when in isolation [43].

Computational studies in combination with NMR have proposed over 30 conformers for monomeric tau [36]. More recently, distinct conformer species of tau have been detected. Single-molecule fluorescence anisotropy combined with an anti-Brownian electrokinetic trap revealed two tau conformers, a more compact family and less compact family [44, 45]. In spite of this, it is currently unclear how these conformers are connected to function, aggregation or disease etiology.

1.3 Tau and Phosphorylation

Post-translational modifications (PTMs) involve the addition of chemical groups, sugars, or proteins to a specific residue after translation by ribosomes or folding and localization in the cell. These changes made to proteins can alter its properties to influence structure, function, and protein-protein interactions, including aggregation [46, 47]. Essentially all proteins are susceptible to PTMs, and the lack of tertiary structures in IDPs make these "natively unfolded" proteins more vulnerable to these modifications [2, 47-49]. PTMs play a role in the life cycle of a protein and have been shown to be a key factor in the regulation of tau's clearance, conformation and aggregation propensity [50]. However, various PTMs have been identified in tau extracted from healthy brains, suggesting that PTMs play a role in tau function outside of disease [51]. The amino acid residues that are susceptible to modification (Ser, Thr, Tyr, Lys, Arg, Asn, His, and Cys) comprise approximately 35% of tau's sequence [52]. Therefore, it is unsurprising that tau can gain multiple types of modifications: phosphorylation on Ser, Thr, or Tyr; acetylation, ubiquitination,

SUMOylation, and glycation on Lys; methylation on Lys or Arg; O-GlcNAcylation on Asn and Thr, N-glycosylation on nitrogens; nitration on Tyr and oxidation on carbons.

Even though there are several theories for the involvement of PTMs in disease progression it remains unclear which PTMs are associated with normal brain function and those that may function in aggregates. The transition of healthy tau to aggregated tau is likely not due to a singular PTM, but the effects of said modification on the intrinsic properties of tau and extrinsic conditions that work in combination to cause disease. For example, certain PTMs may make tau more susceptible to other modifications, seeing as SUMOylation may enhance phosphorylation at T231 and S262 [40]. Alternatively, acetylation at KXGS tau motifs may inhibit phosphorylation, suggesting a protective role of one PTM over another that may lead towards aggregation [53, 54]. In general this concept, or the PTM code hypothesis, proposes that the combination of PTMs on a protein act as a dynamic "code" that further adds biological complexity [55].

Amongst the proteome, protein phosphorylation is the most common PTM [56] and results in the addition of a phosphate (PO_4) group to the polar group of Ser, Thr, or Tyr [57]. In a cell, the enzyme kinases (phosphorylate) and phosphatases (dephosphorylate) regulate the phosphorylation status of proteins [58]. Many kinases have been shown to phosphorylate the serine and threonine residues of tau; including: glycogen synthase kinase 3 (GSK3β), cyclin dependent kinase 5 (cdk5), casein kinase 1 (CK1), cyclic AMP- dependent protein kinase (PKA), p42/p44 MAPKs (ERKs 1/2), protein kinase C (PKC), calmodulin-dependent protein kinase II (CaMKII), the brain-specific kinases 1 and 2, the tau-tubulin kinases 1 and 2, and some microtubule affinity-regulating kinases (MARKs; also known as PAR1 kinases) [59]. While the tyrosine residues of tau are modified via other kinases: SRC family members (LCK, SYK, and FYN) and the ABL family members (ARG and ABL1) [60]. Conversely, tau can be dephosphorylated by protein phosphatases (PP) 1, 2A,

2B, 2C, and 5 [61]. However, amongst these phosphatases PP2A is responsible for approximately 70% of tau dephosphorylation in the brain [62]. PP2A may also be part of a feedback cycle in which PP2A also dephosphorylates components that lead to GSK3β and its subsequent phosphorylation activity of various proteins, including tau [63]. Though several kinase pathways have been suggested to play a role in tau phosphorylation [64].

Approximately 20% of full-length tau (2N4R) has the potential to be phosphorylated (85 sites: 44 Ser, 35 Thr, and 5 Tyr) [54]. Of these sites, ~20 and ~44 residues were found to be present when extracted from healthy brains and brains with tau-associated disease respectively [61, 65, 66]. Yet, it is also possible that there are other tau phosphorylation sites due to the rapid dephosphorylation of tau observed in biopsy samples of human brain [67]. Adding further complexity, the phosphorylation status of tau is also developmentally regulated, suggesting the importance of phosphorylation in "normal" tau function throughout development [68, 69]. It is unlikely that a single tau molecule is phosphorylated at all available sites at once, but these phosphorylation events are also not completely independent from each other [70]. Ordered phosphorylation has been observed, in which sites associated with tau phosphorylation antibodies AT8, AT180, and PHF1 are primed by Cdk5-p35/25 to be later targeted by GSK3β [71, 72].

1.4 Tau and Neurodegeneration

Tauopathies are a collection of neurodegenerative diseases which contain hyperphosphorylated tau deposits [73]. In fact, immunostaining of postmortem brains for phosphorylated tau (AT8, AT180, and PHF1 antibodies) are often used as definitive diagnosis of Alzheimer's Disease (AD) and tauopathy since phosphorylation sites recognized by these antibodies are modified to an appreciably lesser extent in healthy, control patient brains [74-76].

For AD, tau pathology specifically starts in the entorhinal cortex and hippocampus before spreading throughout the rest of the brain in a spatial pattern, known as Braak staging [77]. It is of note, however, that most AD cases are not associated with tau mutations but are instead sporadic, thereby emphasizing that other factors are involved in disease etiology.

Tau has remained the main focus of AD studies based on the original discovery of neurofibrillary tangles (NFTs) and aggregates, which increase in number alongside clinical AD symptoms [77]. Aggregates of tau form β-sheet rich structures known as amyloid fibrils. High-resolution three-dimensional structures of these fibrils have been achieved due to advancements in cryo-electron microscopy (cryo-EM) technology which has revealed that the tau filaments derived from the brains of patients with various tauopathies have differing filament folds [78, 79]. For example, in Alzheimer's disease (AD) the tau filament core is composed of a double-layered C-shaped arrangement of eight beta-strands [80], and this significantly differs from the double-layered J-shaped arrangement with nine beta-strands in Pick's disease (PiD) [81].

If each tauopathy has its own unique folding pattern, this structural specificity could stem from the presence or absence of certain PTMs [79]. For example in tau, S262 is phosphorylated in AD, and corticobasal degeneration (CBD) filaments but not in patients with PiD [82]. Yet S262 is in the filament core of PiD but not in that of AD, suggesting that the phosphorylation status of a specific residue can affect filament structure and disease susceptibility [79]. It is still unclear if PTMs are necessary or sufficient for tau filament assembly [83]. In paired helical filaments isolated from patients with AD, the 10 major phosphorylation sites identified are within the PRR and C-terminus (20, 117). Specifically, PRR phosphorylation increases with disease progression and is correlated to the AT8 site (S202, T205) [84] and S199 and T231 are predominantly phosphorylated in paired helical filaments (PHFs) [85]. Pseudophosphorylated tau (S202, T205) shows enhanced

aggregation *in vitro* [86] which implies that some sites may have specific effects on fibril formation.

1.5 Microtubules

Microtubules are long hollow tubes formed by heterodimers of α-tubulin and β-tubulin subunits. Tubulin dimers are arranged head-to-tail to create polarized microtubule polymers with typically anchored "minus" ends and dynamic "plus" ends [87]. However, microtubules can grow from either plus or minus ends through the addition of tubulin dimers. Both α-tubulin and β-tubulin bind GTP but upon inclusion of a tubulin dimer, only the GTP bound on β-tubulin is hydrolyzed. If the rate of GTP hydrolysis is faster than the addition of new tubulin dimers, the "GTP cap" on the end of the microtubule is lost, which triggers a switch from growth to shrinkage known as catastrophe [88-90]. The stochastic cycling between polymerization and depolymerization, or the "dynamic instability," intrinsic to microtubules is important for maintaining cellular structure and axonal transport in neurons [91].

Several factors can influence microtubule structure. Generally, GTP-tubulin stabilizes microtubules whereas GDP-tubulin is less stable [92, 93]. Tubulin heterodimers are also curved in solution and straighten out within the microtubule lattice. Even after depolymerizing from a microtubule, tubulin dimers return to a curved, "ram's horn" state in solution [94, 95]. The curvature of this free tubulin dimer does not appear to be appreciably dependent on nucleotide state [96-101]. In addition to lateral changes due to tubulin curvature, longitudinal changes from tubulin compaction can also occur. Although it is unclear if tubulin compaction is affected by nucleotide state or vice versa [93, 102, 103].

In vitro, microtubules can be formed using purified tubulin independent of any accessory proteins but dependent on the concentration of free tubulin [104]. Although spontaneous nucleation of microtubules is possible, it is likely more kinetically favorable to form microtubules from existing templates. Various microtubule associated proteins (MAPs) and microtubule stabilizing agents such as taxol can promote microtubule formation by stabilizing lateral or longitudinal interactions between dimers and thereby favor microtubule formation [105]. One such factor, the GTP analogue GMPCPP, inhibits GTP hydrolysis of β-tubulin and consequently prevents the conformational changes associated with microtubule destabilization [87]. Conversely severing enzymes like katanin can use pre-existing microtubules as templates for additional microtubules. These ends are then stabilized by the addition of GTP-bound tubulin [106], the severing enzyme itself [107-109] or additional MAPs such as the CAMPSAP family which can bind to katanin [110].

1.6 Tau and Microtubules

Tau has multiple proposed binding partners. Bioinformatic analysis showed 73 direct binding partners [2], and a separate study identified 175 additional potential and known interacting proteins [111]. Even though tau is primarily located in neuronal axons, it can also be found within neuronal nuclei where it has been shown bound to DNA and RNA to regulate gene expression [112-114]. Tau has also been shown to interact with the plasma membrane [115], the endoplasmic reticulum [116] and Golgi [117]. In addition to cell membranes, tau may also play a role in cell signaling by interacting with signaling cascade proteins such as 14.3.3, Pin-1, and Fyn [32, 118]. However, the main function of tau is thought to be the modulation of microtubules to affect neurite outgrowth [119, 120], axonal transport [121-123] and synapsis [124].

Microtubules are the primary binding partner for tau. Intriguingly, the interaction of tau with axonal microtubules may be dynamic [125]. In cultured neurons, tau was observed to be quickly binding and detaching from the microtubule lattice, with this "kiss and hop" behavior occurring with an average dwell time in the millisecond regime for single tau molecules [126]. In contrast to this study, tau was suggested to instead promote the GTP caps at microtubule ends [127]. Through promoting GTP caps, tau would therefore decrease the frequency of microtubule catastrophe.

Tau's charge distribution is believed to play a role in tau interactions with microtubules as well as other binding partners [68]. The positively charged MTBR of tau binds to microtubules predominantly through electrostatic interactions [128-132]. The microtubule surface is negatively charged due to the C-terminal regions of tubulin (E-hooks) filled with acidic glutamates [133, 134]. Specifically, electrostatic interactions of the MTBR along the microtubule surface are defined by interactions with H11 and H12 α-tubulin and β-tubulin helices [135]. A recent cryo-EM structure has observed that tau does interact with helices H11 and H12 on tubulin and build upon this finding to ultimately propose a model of the MTBR binding longitudinally along the protofilament ridge [135].

The PRR also contributes to tau-microtubule interactions as observed *in vitro* and in cells [136, 137]. Several studies have emphasized the importance of portions of the PRR, namely, parts of the P2 (215-221), in increasing microtubule affinity and promoting interactions with the MTBR [138-140]. An earlier portion of the PRR (166-246) has also been shown to bind weakly to taxol-stabilized microtubules [138]. Most recently, the isolated PRR was capable both of binding to soluble tubulin, and had the capacity to polymerize tubulin, independent of the MTBR [141].

However, the presence of the PRR across other tau/MAP2/MAP4 family members suggests that it plays a role as a general modifier of microtubule interactions in the entire protein family [136].

Tau-tubulin interactions are dependent on the concentrations of the proteins themselves [142], salt [131], and pH [143]. Adding further complexity, PTMs such as phosphorylation make tau more negatively charged and are proposed to lead to aggregation by decreasing interactions with negatively charged microtubules [68, 144-146]. Specifically, phosphorylation within the MTBR (S262, etc.) and PRR (T231, etc.) reduce tau's affinity for microtubules [83, 147-149]. Individual phosphorylation events in the PRR (S214) [150, 151] as well as phosphorylation-mimicking glutamate clusters [152] have been shown to reduce tau-microtubule interactions and suppress *de novo* microtubule polymerization. Phosphomimic mutations within the PRR (S198, S199, S202, T231, S235 combined) decrease *de novo* microtubule polymerization [152] whereas a tau construct with 10 phosphomimic mutations was able to interact with microtubules with a slower dwell time [136]. In contrast, residues outside of these domains do not seem to impair microtubule binding (S396, S404, and S422) despite being phosphorylated in diseased brains [153, 154], suggesting these regions instead influence aggregation [155].

CHAPTER 2: PHOSPHOMIMICS CUMULATIVELY REDUCE PRR BINDING TO TUBULIN AND MICROTUBULES

Part of this chapter is adapted from Karen Acosta, Christopher Brue, Hee Jong Kim, Polina Holubovska, Leland Mayne, Kenji Murakami, Elizabeth Rhoades, "Structural Insights into the Role of the Proline Rich Region in Tau Function" (*submitted*)

I collected all the data in this chapter except for the imaging of PRR bound to microtubules completed by Polina Holubovska.

2.1 Introduction

Tau is a microtubule-associated protein that is generally thought to function in regulating microtubule stability and dynamics [20, 156]. Even upon binding to soluble tubulin [157, 158] or microtubules [135, 159], tau remains largely disordered. Four major domains can be used to define tau, the N-terminal projection domain, the proline rich region (PRR), the microtubule binding region (MTBR), and the C-terminal region. Although PRR, MTBR, and pseudo-repeat, R′ have all been shown to be involved in interactions with microtubules [132, 140, 159, 160], the MTBR has been the focus of most intensive study, not only because of its role in binding to tubulin and microtubules but also because it forms the core of associated disease aggregates [80, 81, 161]. However, recent work from our lab demonstrated that the isolated PRR was capable both of binding to soluble tubulin, and had the capacity to polymerize tubulin, independent of the MTBR [141].

Nearly a hundred PTMs have been identified on tau, including phosphorylation, acetylation, and ubiquitination, amongst others [76]. While a detailed understanding of how these numerous possible modifications impact tau function as well as its aggregation are lacking, tau phosphorylation has been heavily studied and hyperphosphorylation of tau aggregates found in post-mortem brain tissue has long been observed in disease [162]. The aggregation and deposition

of hyperphosphorylated tau as neurofibrillary tangles is characteristic of a broad class of diseases termed tauopathies, including Alzheimer's Disease [73]. Many studies have focused considerable attention on understanding the molecular and cellular factors that influence tau self-assembly. However, both loss of functional tau and subsequent destabilization of microtubules, as well as gain of toxic function through aggregation, are thought to play roles in the cell death observed in these diseases [163-165].

Intriguingly, potential phosphorylation sites linked both to function and disease also cluster with high frequency within the PRR. In Alzheimer's patient samples some of the most frequently phosphorylated sites, T181, T217, T231, S235, and S262, are located within the PRR [74]. We incorporate phosphomimic mutations (from serine or threonine to glutamate) at several locations within the PRR, both individually and in combination, to probe how modification alters interactions with tubulin and microtubules. We use a combination of techniques to characterize the impact of phosphomimic mutations in the PRR on tubulin binding and microtubule polymerization. These results highlight that phosphomimics in the PRR cumulatively diminish tubulin and microtubule binding and ultimately slow microtubule polymerization.

2.2 Results

2.2A Increasing phosphorylation diminishes PRR-tubulin binding

In Alzheimer's disease patient samples, the most frequently phosphorylated sites within the PRR are T181, T217, T231 and S235 [76]. As these four sites are also abundant in healthy control tissue [76], we chose to make phosphomimic mutations from serine or threonine to glutamate both individually and in combination at each of these sites to observe how these modifications alter behavior with tubulin and microtubules (Figure 2.1). In addition, a cysteine mutation was introduced at the N-terminus (residue 149) to allow for site-specific labeling with Alexa Fluor 488 maleimide.

Fluorescence correlation spectroscopy (FCS) can detect molecular dynamics, and we use this technique to measure binding of PRR as a function of tubulin concentration. In these experiments, we measure the changes in fluorescence intensity of a fluorescently labeled species diffusing through a focused laser. The fluctuations in fluorescence intensity are autocorrelated and these curves are fit to a diffusion model (Figure 2.2A-B). Through this method we can accurately measure the local concentration, hydrodynamic radius, and diffusion coefficient of the labeled species and observe protein interactions [166, 167]. For this work, PRR was fluorescently labeled, and binding was measured with increasing amounts of unlabeled tubulin. Specifically, FCS measurements were made using ~20 nM Alexa 488 labeled PRR and tubulin in concentrations ranging from 0 to 10 μM. As larger complexes are formed, the diffusion time increases and the midpoint of the autocorrelation curve ($G(\boldsymbol{\tau})$) shifts accordingly to longer times (Figure 2.2C). These curves were fit to extract the fraction of PRR bound to tubulin at each concentration measured.

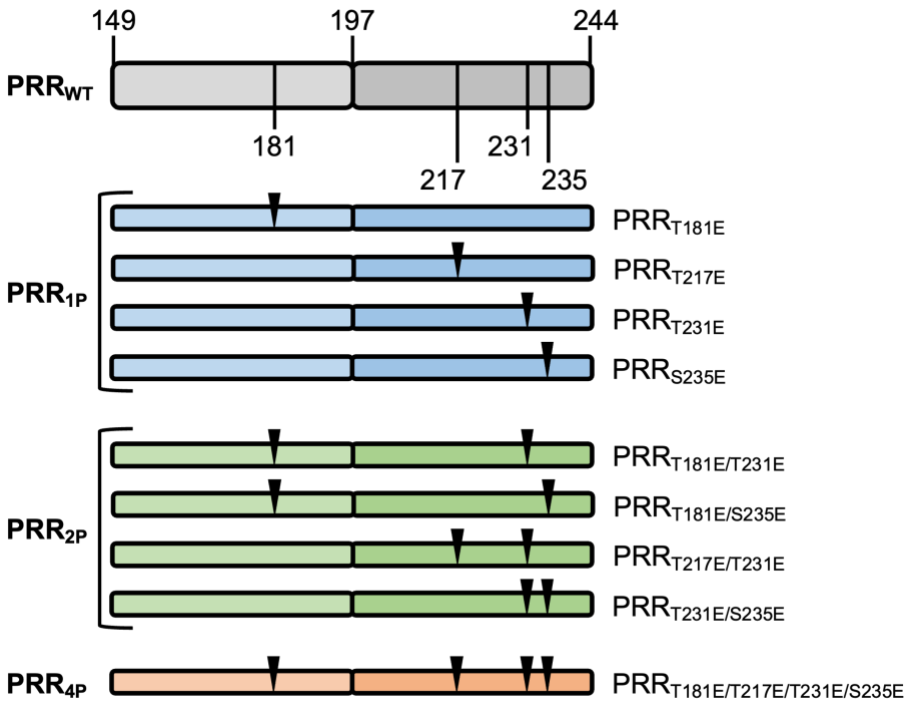

Figure 2.1 Schematic of PRR constructs with phosphomimic sites.
PRR as well as the location of phosphomimic sites (triangles), with numbering of the residues based on 2N4R. Construct abbreviations are as follows: PRR_{WT}; PRR_{1P} = PRR_{T181E} or PRR_{T217E} or PRR_{T231E} or PRR_{S235E}; PRR_{2P} = $PRR_{T181E/T231E}$ or $PRR_{T181E/S235E}$ or $PRR_{T217E/T231E}$ or $PRR_{T231E/S235E}$; PRR_{4P} = $PRR_{T181E/T217E/T231E/S235E}$.

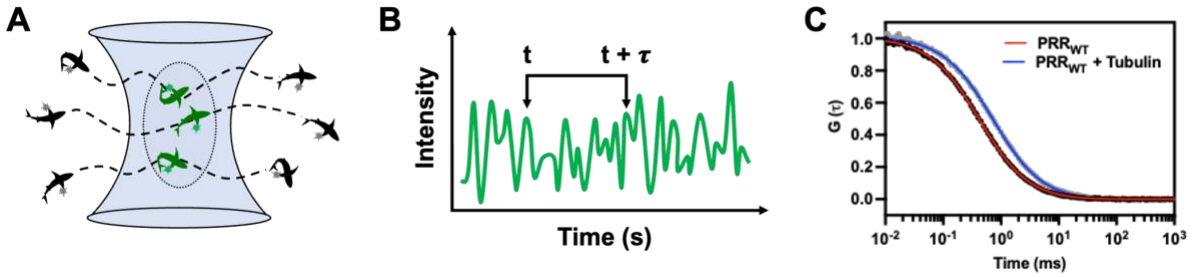

Figure 2.2 Measuring PRR binding to tubulin with FCS.
(A) A protein with a single fluorescent label diffusing through a focused laser within a confocal volume (as defined by the dashed circle). **(B)** As the protein passes through the observation volume, the dye is excited and changes the measured fluorescence intensity over time. The fluctuations in fluorescence intensity are autocorrelated to produce autocorrelation curves G($\boldsymbol{\tau}$). **(C)** Unlabeled tubulin is added to fluorescently labeled PRR and increases the decay time of the autocorrelation curves, the mid-point of which is the diffusion time. Autocorrelation curves of free PRR_{WT} (black) and PRR_{WT} bound to tubulin (gray) with one or two component diffusion fits for PRR_{WT} (red) and PRR_{WT} bound to tubulin (blue), respectively. By repeating measurements with increasing amounts of tubulin added to PRR, we can use FCS to quantify binding interactions.

Wild-type PRR (PRR_{WT}) binding occurs in two phases, with the first phase of binding observed at concentrations less than approximately 1.5 μM tubulin, with full saturation at roughly 5 μM tubulin (Figure 2.3A). This bimodal behavior of PRR_{WT} has been observed [141] and also consistent with previously published data, these diffusion times at the inflection and saturation points correspond to PRR bound to one or two tubulin dimers, respectively [131]. However, upon the introduction of any individual phosphomimic, PRR_{1P}, (Figure 2.3B) PRR shows some reduction in tubulin binding (comparison between PRR phosphomimics, Figure 2.3E). The binding curves cluster together fairly closely, with the exception of PRR_{T231E}, which shows a greater reduction in binding, particularly at low tubulin concentrations, than the other single phosphomimics examined here (PRR_{T181E}, PRR_{T217E}, or PRR_{S235E}).

It is likely that tau is phosphorylated at more than one site at any one time, especially with over a dozen sites observed within the PRR alone in both healthy brains as well as in tauopathy. Therefore, it is of interest to examine these effects on tubulin binding of phosphomimics occurring simultaneously in the same construct. When PRR contains two phosphomimic mutations, PRR_{2P}, we again observe that the binding curves cluster together (Figure 2.3C) and show a greater reduction in tubulin binding capacity compared to PRR_{WT} and PRR_{1P} variants (Figure 2.3E). Although in isolation, PRR_{T231E} showed a greater diminishment in tubulin binding than the other single phosphomimics, this behavior is superseded by the addition of a secondary mutation.

To further examine the role of the presence of multiple phosphomimics in one construct, we measured binding of PRR with all four phosphomimics present, PRR_{4P}. We find that PRR_{4P} has a significantly diminished ability to bind to tubulin dimers (Figure 2.3D-E). These results suggest that, at least for the sites investigated here, that the accumulation of multiple phosphorylation events in a single construct intensify the loss of tubulin binding, without a single

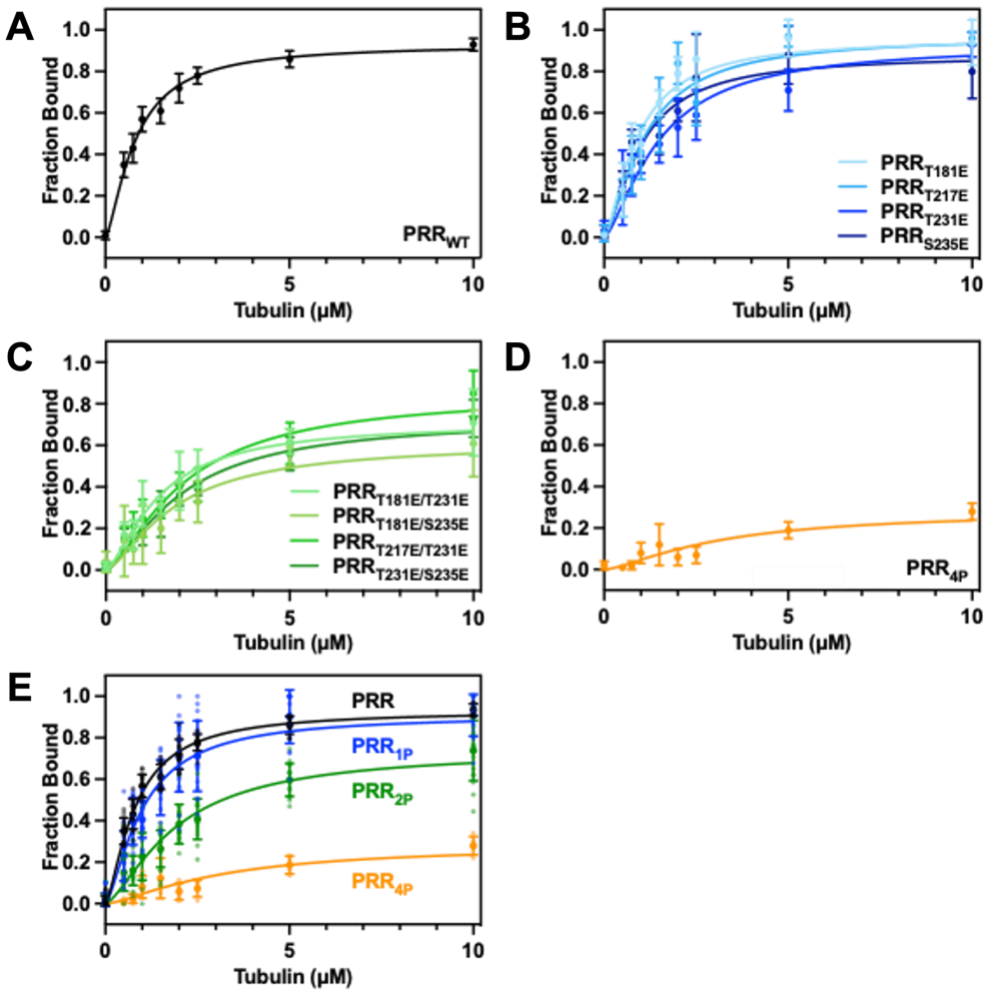

Figure 2.3 Increasing phosphorylation diminishes PRR-tubulin binding.
Binding of PRR constructs to tubulin dimers is quantified via fitting the fraction tau bound as a function of tubulin concentration by the Hill equation. Data is presented as mean ± SD, for $n \geq 3$ independent measurements. Constructs are represented as follows: **(A)** PRR_{WT} (black), **(B)** PRR_{1P} plotted individually (blue) **(C)** PRR_{2P} plotted individually (green) and **(D)** PRR_{4P} (orange). **(E)** Independent measurements are depicted. PRR_{1P} constructs (PRR_{T181E}, PRR_{T217E} , PRR_{T231E} and PRR_{S235E}) and PRR_{2P} ($PRR_{T181E/T231E}$, $PRR_{T181E/S235E}$, $PRR_{T217E/T231E}$, and $PRR_{T231E/S235E}$) were averaged to facilitate comparison. Refer to Table 2.1 and 2.2 for numerical values of fitting coefficients for binding curves and fraction bound for each construct respectively.

PRR Construct	K_D (μM)
PRR_{WT}	0.80 ± 0.06
PRR_{T181E}	0.89 ± 0.07
PRR_{T217E}	1.08 ± 0.08
PRR_{T231E}	1.47 ± 0.11
PRR_{T235E}	0.98 ± 0.08
$PRR_{T181E/T231E}$	1.43 ± 0.14
$PRR_{T181E/S235E}$	1.87 ± 0.21
$PRR_{T217E/T231E}$	2.16 ± 0.18
$PRR_{T231E/S235E}$	2.04 ± 0.19
$PRR_{T181E/T217E/T231E/S235E}$	3.15 ± 0.83

Table 2.1 Fitting coefficients from binding curves.
Binding curves derived from FCS measurements of PRR-tubulin were fit to the Hill equation for constructs shown in Figure 2.3. The Hill coefficient was fit as a global parameter (1.5 ± 0.1), while the dissociation constants (K_D), were determined individually.

site dominating this loss. In the presence of four times the approximate saturation point (20 μM tubulin), the diffusion times of PRR_{WT} and PRR_{1P} do not markedly change (Figure 2.4). For PRR_{2P} and PRR_{4P} there is not an appreciable increase in the diffusion time, further highlighting the depletion of PRR-tubulin binding upon the addition of multiple phosphomimics.

Interestingly, irrespective of the number of phosphomimic mutations present, PRR retains the bimodal binding curve. Attempts to fit the binding curves to a model with two binding sites were not productive; likely the binding affinities for the two sites are too close in magnitude (<10x) to be rigorously differentiated. Instead, the binding curves were fit with the Hill equation to obtain K_D values for comparison (Table 2.1). Fitting of these binding curves yields a global Hill coefficient of $n = 1.5 \pm 0.1$ (Table 2.1), in agreement with our previous measurements [141] emphasizing the association of PRR to more than one tubulin dimer at saturation.

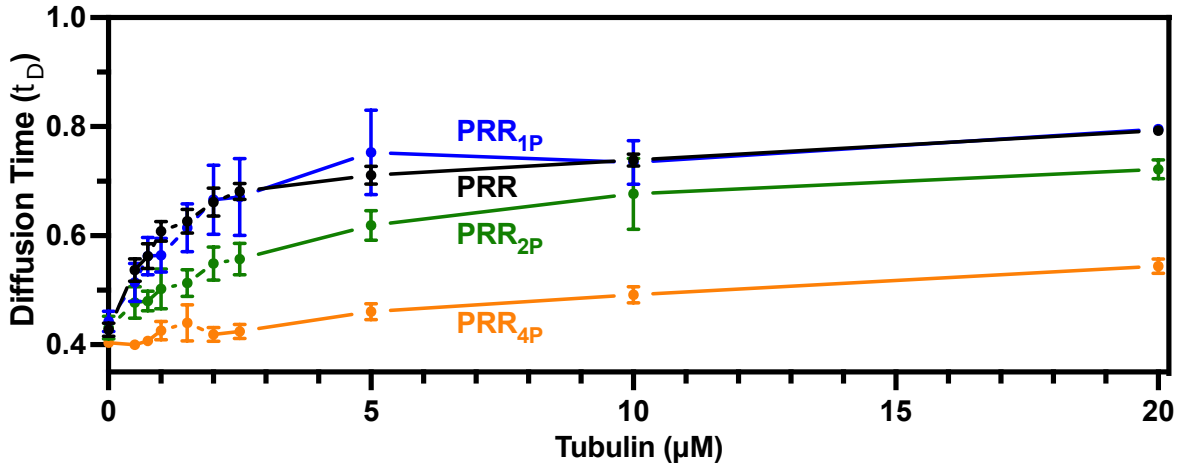

Figure 2.4 Extended PRR-tubulin binding curve.
Diffusion times of PRR constructs binding to tubulin dimers. Data is presented as mean ± SD, for n ≥ 3 independent measurements, except for 20 μM measurements of PRR_{WT} (black) and PRR_{1P} (blue) which contain measurements with n = 1, and n = 2 respectively. PRR_{1P} constructs (blue, PRR_{T181E}, PRR_{T217E}, PRR_{T231E} and PRR_{S235E}) and PRR_{2P} (green, $PRR_{T181E/T231E}$, $PRR_{T181E/S235E}$, $PRR_{T217E/T231E}$, and $PRR_{T231E/S235E}$) were averaged to facilitate comparison. Independent measurements are depicted. Refer to Table 2.2 for numerical values of diffusion times for each construct.

PRR Construct	τ_D (ms)		Fraction Bound	
	- tub	+ tub	- tub	+ tub
PRR_{WT}	0.43 ± 0.01	0.74 ± 0.03	0.01 ± 0.02	0.93 ± 0.03
PRR_{T181E}	0.45 ± 0.01	0.74 ± 0.04	0.01 ± 0.01	0.94 ± 0.11
PRR_{T217E}	0.45 ± 0.04	0.76 ± 0.03	0.02 ± 0.04	0.96 ± 0.03
PRR_{T231E}	0.44 ± 0.03	0.74 ± 0.02	0.03 ± 0.05	0.93 ± 0.06
PRR_{T235E}	0.44 ± 0.02	0.69 ± 0.05	0.03 ± 0.03	0.80 ± 0.13
PRR_{1P}	0.45 ± 0.01	0.74 ± 0.04	0.02 ± 0.03	0.91 ± 0.10
$PRR_{T181E/T231E}$	0.43 ± 0.01	0.66 ± 0.05	0.02 ± 0.02	0.71 ± 0.16
$PRR_{T181E/S235E}$	0.45 ± 0.02	0.63 ± 0.05	0.04 ± 0.05	0.61 ± 0.16
$PRR_{T217E/T231E}$	0.42 ± 0.01	0.68 ± 0.05	0.01 ± 0.02	0.85 ± 0.11
$PRR_{T231E/S235E}$	0.43 ± 0.02	0.67 ± 0.03	0.02 ± 0.02	0.73 ± 0.09
PRR_{2P}	0.43 ± 0.01	0.66 ± 0.05	0.02 ± 0.03	0.74 ± 0.14
$PRR_{T181E/T217E/T231E/S235E}$	0.40 ± 0.01	0.49 ± 0.01	0.02 ± 0.02	0.28 ± 0.04

Table 2.2 Summary of FCS biophysical data of PRR constructs.
All PRR constructs contain T149C mutations and are labeled with Alexa Fluor 488 maleimide at this position. PRR_{1P} constructs (PRR_{T181E}, PRR_{T217E} , PRR_{T231E} and PRR_{S235E}) and PRR_{2P} ($PRR_{T181E/T231E}$, $PRR_{T181E/S235E}$, $PRR_{T217E/T231E}$, and $PRR_{T231E/S235E}$) were averaged to facilitate comparison. Diffusion times (τ_D) of tau constructs and fraction bound in the presence (+ tub) and absence (- tub) of 10 μM tubulin for constructs shown in Figure 2.3 and Figure 2.4. Data is presented as mean ± SD, for $n \geq 3$ independent measurements. Fraction bound is calculated as described in the Material and Methods.

2.2B Increasing phosphorylation diminishes PRR-tubulin polymerization

To investigate the impact of phosphomimics on the polymerization capacity of PRR, both tubulin and PRR were co-incubated in the presence of GTP at 37°C. Polymerization was observed by an increase in light scattered and served as a proxy to track the kinetics of microtubule formation. As has been previously observed [141], tubulin in the absence of PRR does not appreciably polymerize over the approximately ten minute timescale of these measurements (Figure 2.5, *gray*). Upon the addition of PRR_{WT}, the light scatter signal increases almost immediately (Figure 2.5, *black*). In our previous work, we used transmission electron microscopy to confirm that this increase in scatter signal corresponds to microtubule formation [141]. This data is fit with a sigmoidal equation to quantify polymerization half-times (Table 2.3).

We then compared the polymerization kinetics of PRR_{WT} with representative constructs containing one, two or four phosphomimic mutations. For PRR_{1P} the polymerization time is approximately doubled (Figure 2.5, *blue*) relative to PRR_{WT}. Similarly, increases in the polymerization half-times are observed for PRR_{2P} (Figure 2.5, *green*) and PRR_{4P} (Figure 2.5, *orange*) of approximately four and six times relative to PRR_{WT}, respectively. Thus, there is correlation between the reduction in tubulin binding by FCS and inhibition of microtubule polymerization capacity observed as a function of increasing numbers of phosphomimic sites. This polymerization data also supports 1:2 PRR:tubulin stoichiometry for PRR_{4P}:tubulin complexes. While the binding of PRR_{4P} is significantly diminished relative to PRR_{WT}, its tubulin polymerization capacity is retained, although the kinetics are slower. Our prior work has established that simultaneous binding of at least two tubulin dimers are required for tau fragment-mediated tubulin polymerization [131].

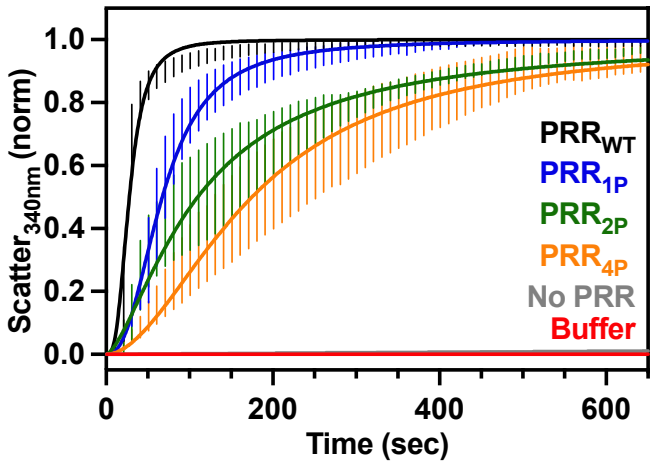

Figure 2.5 Increasing phosphorylation diminishes tubulin polymerization with PRR.
PRR-induced tubulin polymerization is measured by the scattering of light at 340 nm as a function of time. Data is presented as mean ± SD following normalization, for n ≥ 3 independent measurements. The polymerization data is fit with a sigmoidal equation (solid line). Refer to Table 2.3 for numerical values of polymerization half-times for each condition.

PRR Construct	T_{50} (sec)
PRR_{WT}	27.9 ± 0.2
PRR_{1P}	67.4 ± 0.6
PRR_{2P}	110.0 ± 1.6
PRR_{4P}	175.0 ± 1.4

Table 2.3 Sigmoidal fitting of microtubule polymerization assays.
PRR microtubule polymerization curves were fit to a sigmoidal equation to determine polymerization half-times (T_{50}) for constructs shown in Figure 2.5. Values for T_{50} are mean ± SD following normalization, for $n \geq 3$ independent measurements.

2.2C PRR can bind to microtubules and is reduced by phosphorylation

We have previously established that the PRR is sufficient for binding to and polymerizing tubulin [141]. In this work, we reproduce these findings and observe a decrease in PRR-tubulin interactions with respect to the degree of phosphorylation. However, we have not investigated the interaction of the PRR with microtubules when multiple phosphomimics are present. To visualize PRR interactions with microtubules, we labeled PRR with Alexa Fluor 488 maleimide at amino acid position T149C and tubulin with Rhodamine Red-X. Labeled tubulin was polymerized into microtubules and stabilized with taxol. Fluorescently labeled PRR was briefly incubated with the microtubules at a 1:4 PRR:tubulin ratio and imaged with total internal reflection fluorescence (TIRF) microscopy.

Both PRR_{WT} and PRR_{4P} bind to taxol-stabilized microtubules, although the binding of PRR_{4P} is significantly reduced as compared to PRR_{WT} (Figure 2.6). This diminishment is not due to differences in the microtubules present in each sample, as the average PRR_{WT} and PRR_{4P} intensity signal is independent of microtubule length, as is the average intensity of the microtubules (Figure 2.7). Neither is this loss of binding attributable to a difference in brightness between the PRR_{WT} and PRR_{4P} constructs as further validated by measurements of the counts per molecule in the absence of tubulin (Figure 2.8).

This observation is of particular interest, as structural models of full-length tau resolved only the MTBR bound to the microtubule lattice [135]. We note that while PRR_{WT} binds relatively uniformly to the MT lattice, PRR_{4P} binding is more variable (Figure 2.6). This has also been observed for full length tau as well as PRR-containing tau fragments on microtubules and mouse hippocampal neurons [168].

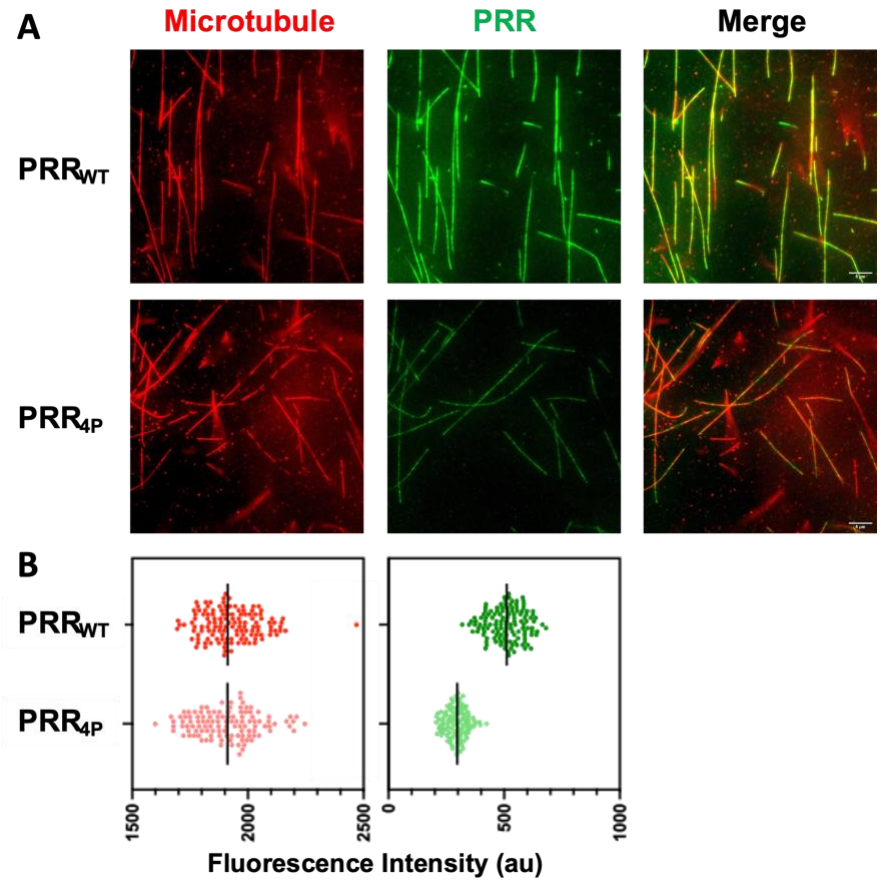

Figure 2.6 PRR binds to microtubules and phosphomimic presence reduces binding.
(A) Images of microtubules (labeled with Rhodamine Red-X) co-incubated with PRR_{WT} or PRR_{4P} (labeled with Alexa 488) in a 0.5:1 tau:tubulin ratio. **(B)** Plots of average fluorescence intensity per microtubule. Each point represents the average intensity of tubulin-Rhodamine Red-X (left) or PRR-Alexa 488 (right) for a single microtubule, with the median intensity indicated by a line. N = 131 and N = 115 for PRR_{WT} microtubules and PRR_{4P} microtubules, respectively. Two-tailed unpaired t-tests for tubulin-Rhodamine Red-X showed no significant difference between PRR_{WT} or PRR_{4P}. However, two-tailed unpaired t-tests for PRR-Alexa 488 showed a significant difference between PRR_{WT} or PRR_{4P} (green, $p < 0.0001$).

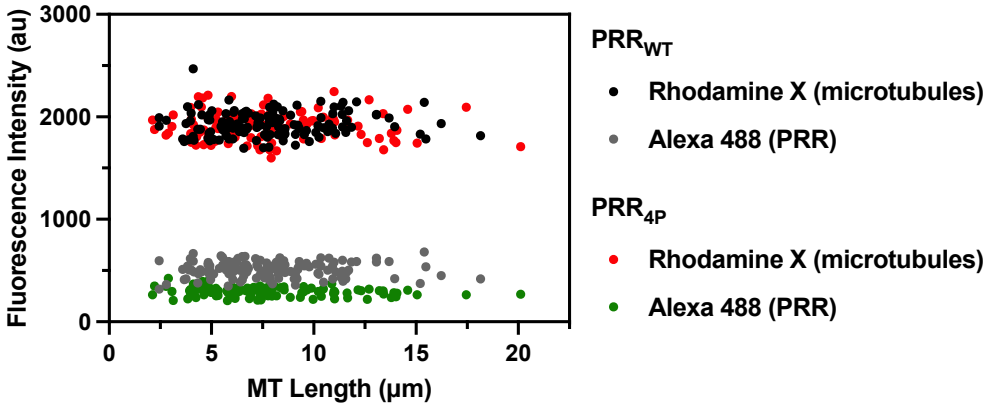

Figure 2.7 Fluorescence intensities of microtubules and PRR imaging are independent of microtubule length.

Each point represents the average fluorescence intensities of microtubules (black, red) and PRR (gray, green) as a function of measured microtubule length for individual microtubules. N = 131 and N = 115 for PRR_{WT} microtubules and PRR_{4P} microtubules, respectively, for images shown in Figure 2.6.

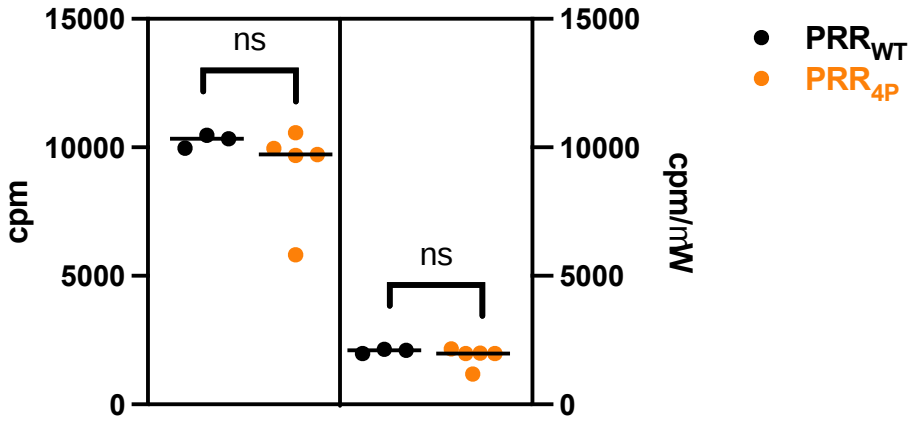

Figure 2.8 Counts per molecule of PRR constructs used for TIRF imaging.
Each point represents the counts per molecule (cpm) or counts per molecule per laser power in microwatts (cpm/μW) of PRR_{WT} (black) or PRR_{4P} (orange) from independent FCS measurements in the absence of tubulin, with the median intensity indicated by a line. Data is for $n \geq 3$ independent measurements. Two-tailed unpaired t-tests for both cpm and cpm/μW showed no significant difference between PRR_{WT} or PRR_{4P}.

2.2D PRR conformation does not change in the presence of multiple phosphomimics or saturating tubulin concentrations

Tau is an intrinsically disordered protein and like other IDPs, maintains an expanded and unfolded structure in solution. This native disorder is largely maintained even when tau is bound to soluble tubulin [157, 158] or microtubules [135, 159]. To investigate if there are conformational dynamics at play for the PRR region, both in the presence and absence of either phosphomimics or tubulin, pulse-interleaved excitation-Förster resonance energy transfer (PIE-FRET) experiments were conducted.

In FRET the energy transfer between two fluorescent dyes on a single protein can be used to measure intramolecular distances [169-171]. When a double fluorescently labeled protein diffuses through a focused laser the donor dye is excited. This donor dye then fluoresces or transfers energy non-radiatively via a dipole-dipole interaction to an acceptor fluorophore. The efficiency of the energy transfer is dependent on the distance between the donor and acceptor fluorophores; therefore, the closer the two dyes are to each other, the higher the probability of energy transfer and the larger the efficiency measured [171]. Conversely, if the two dyes are too distant, the probability of energy transfer is effectively zero.

Here, we have mutated amino acid positions T149 and Q244 to cysteines of PRR constructs for fluorescent labeling with Alexa Fluor 488 (donor) or Alexa Fluor 594 (acceptor) maleimide. Due to the double labeling process, a mixture of labeled proteins with donor-only, acceptor-only, and donor-acceptor population are present. Through PIE-FRET the donor and acceptor fluorophores are excited separately with two pulsed lasers. This allows for the distinction of proteins with missing or non-fluorescing acceptors, and for direct excitation of the acceptor to

differentiate between low energy transfer efficiencies (ET_{eff}) events and those associated with the donor-only protein of the 'zero-peak' ($ET_{eff} = 0$) [172].

Typically, tens of thousands of events are collected, and the energy transfer efficiencies are individually calculated and plotted as a histogram. These histograms are then fit with a model to convert the distribution of energy transfer efficiencies into a distance distribution, which for IDPs, typically involve some sort of polymer model [173]. In this case, we fit our data using a Gaussian polymer chain model which assumes that each residue is treated as a randomly oriented monomer within a chain, restrained only by the peptide bond length.

In solution, no shift between PRR_{WT} and PRR_{4P} histograms were detected (Figure 2.9). This suggests that the presence of multiple phosphomimics does not alter the conformation of the region. A saturating concentration of tubulin was defined based on the concentration at which the diffusion time of PRR_{WT} does not significantly change (Figure 2.3). Upon the addition of twice the saturation point of tubulin (10 μM tubulin) neither PRR_{WT} nor PRR_{4P} significantly shifts in ET_{eff} (Table 2.4).

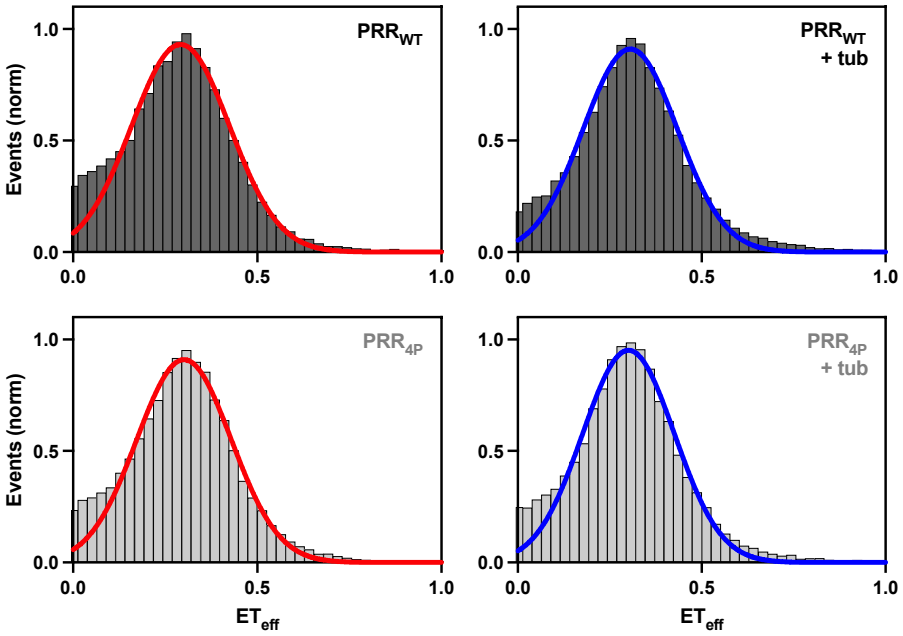

Figure 2.9 PIE-FRET of PRR constructs with tubulin show no significant conformational changes.

PIE-FRET histograms of PRR_{WT} (dark) or PRR_{4P} (light) in the absence (red) and presence (blue) of 10 µM tubulin. Both PRR_{WT} and PRR_{4P} are labeled at T149C and Q244C with Alexa Fluor 488 or 594 maleimide. Histograms are fit to a Gaussian distribution to determine the mean ET_{eff} as described in the Materials and Methods. Data is presented for $n \geq 3$ independent measurements. Refer to Table 2.4 for numerical values of $ET_{eff} \pm$ SD for each construct.

PRR Construct	ET_{eff}	
	- tub	+ tub
PRR_{WT}	0.29 ± 0.13	0.31 ± 0.13
PRR_{4P}	0.30 ± 0.13	0.30 ± 0.12

Table 2.4 Mean energy transfer efficiency (ET_{eff}) of PRR constructs with tubulin.
PIE-FRET measurements of PRR_{WT} or PRR_{4P} in the absence and presence of 10 μM tubulin. Data is presented as mean ET_{eff} values ± SD for Gaussian fits of histograms for $n \geq 3$ independent measurements as shown in Fig. 2.9.

2.3 Discussion

The PRR has long been recognized for its role in enhancing tau's interactions with microtubules [174]. More recent work from our own lab proposed that, at least under some conditions, the PRR is tau's primary tubulin and microtubule-binding domain [141]. Here we use select phosphomimic mutations to probe their impact on PRR binding to soluble tubulin and microtubules. Our data suggests that the accumulation of phosphomimic modifications is the primary driver for the decrease in tubulin (Figure 2.3) and microtubule (Figure 2.6) binding affinity, and subsequent decrease in tubulin-polymerization capacity (Figure 2.5).

Phosphorylation of multiple sites is a common means of titrating the interaction affinity between disordered proteins and their partners [12]. The PRR contains a high fraction of the ~55 putative phosphorylation sites that have been identified in tau [76], and it is feasible that multiple residues will be phosphorylated concurrently to alter the functional interactions between tau and tubulin. Prior studies have shown that phosphorylation sites within the PRR have differential effects on interactions with microtubules; phosphorylation at residue 212, 214 and 231 lower the affinity for microtubules, with other sites having only minor effects [83]. Here, we find that while modification of one individual site may have a mild impact on binding affinity relative to another site (Figure 2.3B), these differences are minor in comparison to the impact of multiple phosphomimic modifications simultaneously (Figure 2.3E). Thus, the relative strength of the interaction between tau and tubulin can be 'tuned' by the addition or loss of a phosphate modification. Additionally, the phosphorylation status of tau is developmentally regulated, underscoring the importance of phosphorylation in normal tau function throughout development [68, 69]. Phosphorylation patterns and frequencies may be different in the adult brain, commensurate with different requirements for microtubule growth and stability.

Much of the tau population in cells is bound to microtubules [156, 175]. It is possible that tau may be quickly binding and detaching from the microtubule lattice as previously observed [126, 176, 177]. Similar to other microtubule associated proteins, like EB1, which also promote polymerization of microtubules [178-181], tau has been suggested to interact with GTP caps at microtubule ends [127]. Our TIRF imaging does not appear to align with these models since we observe discontinuous binding of the PRR throughout the microtubule as well as the microtubule ends (Figure 2.6). However, it is known that paclitaxel (taxol) can influence tau's interactions with microtubules [182]. Further studies will be needed to properly examine PRR_{WT} or PRR_{4P} potential nucleotide preference and position on the microtubule.

Speculatively, PRR_{WT} also appears to encourage straight microtubules, compared to the higher incidence of more curvilinear PRR_{4P} associated microtubules (Figure 2.6). Relative to PRR alone, a full-length construct of tau missing the PRR also appeared to have microtubules that were less straight in TEM images [141]; suggesting that the presence of PRR promotes straight microtubules. This provides an interesting potential mechanism is which the PRR helps to stabilize and form straight microtubules. Simultaneously, this would also deter curled protofilaments when a microtubule depolymerizes. Furthermore, phosphorylation reduces tau:tubulin interactions by allowing for more curled microtubules and can be used to tune microtubule dynamics. Which could help address why fetal and AD tau have similarly high phosphorylation levels although fetal tau is not aggregated during neuronal development [69, 183, 184], or the reversible high phosphorylation of tau observed as a normal biological process for hibernating animals [185] and during sleep [186].

Interestingly the PRR alone does not appear to be as conformationally dynamic. Both PRR_{WT} or PRR_{4P} constructs exhibited no significant difference in conformation due to

phosphomimic presence nor tubulin addition (Figure 2.9).In the presence of the polyanionic, aggregation promoter polyphosphate, PRR_{WT} had approximately half the shift in ET_{eff} relative to 2N4R with the same labeling positions (T149C and Q244C) [187]. Whereas longer tau constructs fluorescently labeled to probe the PRR also had similar ET_{eff} in solution with only small expansions due to the addition of tubulin as measured by smFRET [141]. In general, this region appears to remain in an extended conformation despite the addition of binding partners or phosphomimic presence. To fully characterize this region additional labeling positions such as Y197 to probe P1 and P2 separately are required to potentially define dynamics that are otherwise obscured when examining the entire region at once. Similarly, by measuring at saturating tubulin concentrations we may lose transient states that are present at smaller PRR:tubulin ratios.

CHAPTER 3: PHOSPHOMIMICS REDUCE PRR:TUBULIN DYNAMICS FOR THE PRR ALONE AND IN THE PRESENCE OF TUBULIN

Part of this chapter is adapted from Karen Acosta, Christopher Brue, Hee Jong Kim, Polina Holubovska, Leland Mayne, Kenji Murakami, Elizabeth Rhoades, "Structural Insights into the Role of the Proline Rich Region in Tau Function" (*submitted*)

I collected all the data in this chapter except for the HDX-MS measurements completed by Christopher Brue.

3.1 Introduction

By using a combination of spectroscopic techniques, we demonstrate how the presence of phosphomimic mutations in the PRR alone diminishes tubulin and microtubule binding. This loss of PRR affinity subsequently creates a decrease in the ability of PRR to promote microtubule polymerization, and these effects occur more dramatically as phosphomimics increase in number in a single PRR construct. To further characterize the interplay between PRR and tubulin, we utilize hydrogen-deuterium exchange mass spectrometry (HDX-MS) to provide insight into the regions of PRR involved in tubulin binding.

Structural mass spectrometry methods, like HDX-MS, can capture transient interactions that do not require a folded form even amongst complex mixtures like intact cells and cell lysates [18, 19]. In HDX-MS, a protein of interest is placed in a deuterated buffer and the deuterium in the solution exchanges with backbone amide hydrogens. After a determined amount of time, the reaction is quenched with a low-pH buffer and digested with an acidic protease, typically pepsin, to minimize deuterium-labeled protein from exchanging back to hydrogen [188]. The deuterium uptake of each peptide is measured with liquid chromatography-MS (LC-MS) and the rate of

exchange between hydrogen and deuterium is dependent on solvent accessibility and protein structure.

Due to the significant loss of tubulin binding and polymerization by PRR_{4P} relative to PRR_{WT}, we chose these constructs for comparison by HDX-MS. Measurements of PRR_{WT} and PRR_{4P} in the presence and absence of tubulin were prepared for HDX-MS. Peptides were generated using a coupled pepsin and *Aspergillus niger* prolyl endopeptidase (AnPEP) column to improve peptide generation and PRR coverage. We find that the presence of either phosphomimics or tubulin diminish PRR dynamics and simultaneously map two ~15 residue regions of the PRR as primary tubulin binding sites.

3.2 Results

HDX-MS is a technique capable of resolving conformational dynamics that occur during protein binding [189] based on the changes in mass of amide hydrogens on the protein backbone, upon exchange with heavier deuteriums in solution. Pepsin is often used in HDX-MS experiments for generating peptides, in part, due to its broad specificity, mostly cleaving after methionine, leucine, and phenylalanine residues. However, enzymes like pepsin struggle to digest disordered protein regions that contain limited hydrophobic residues [190]. The PRR in particular has a large number of basic residues and lacks any methionine or phenylalanine residues. Further complicating analysis of the PRR are the large number of prolines which are more difficult to digest by many proteases due to the cyclic nature of the residue. The absence of suitable cleavable sites distributed throughout the sequence ultimately decreases the efficiency of pepsin to generate peptides spanning the entire region.

Aspergillus niger prolyl endopeptidase (AnPEP) is currently used in tests for the mitigation of celiac disease symptoms due to its enzymatic preference for digesting prolines [191-193]. However, AnPEP has also been shown to cleave alanines and other amino acids with lower efficiency [194, 195]. To improve peptide coverage, we purified AnPEP (Figure 3.1) and examined its activity with PRR and tubulin (Figure 3.2). We find that PRR_{WT} was able to be cleaved almost entirely by AnPEP, whereas a protein with relatively less prolines, tubulin, was cleaved less efficiently on the same time scale (Figure 3.2).

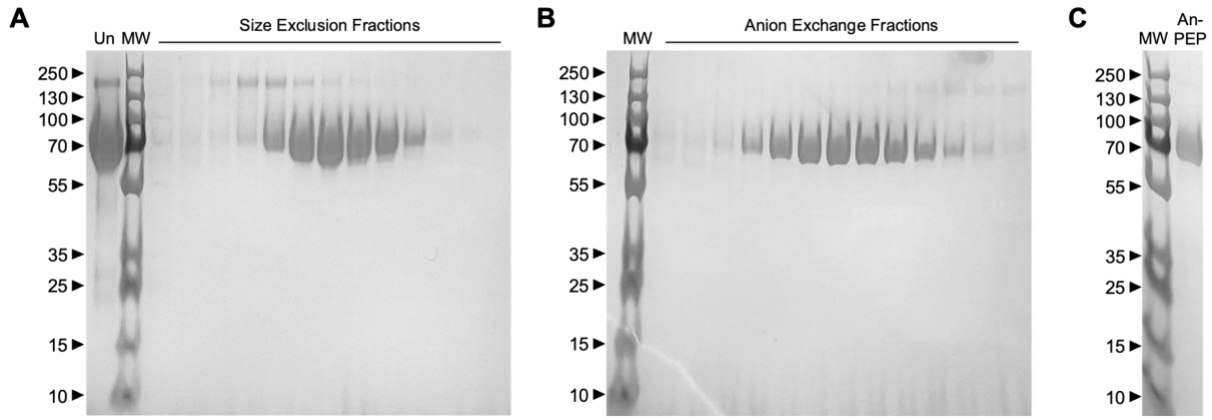

Figure 3.1 Purification of *Aspergillus niger* prolyl endopeptidase (AnPEP).
For HDX-MS, *Aspergillus niger* prolyl endopeptidase (AnPEP) was purified from dietary supplement (GliadinX, AVI Research) by dissolving the contents of one capsule in 2 mL 100 mM phosphate pH 4, 100 mM NaCl. **(A)** The initial solution (Un) was further purified by size exclusion column (Superdex 200 HiLoad 16/600). Fractions containing protein were pooled, concentrated and buffer exchanged into 100 mM phosphate pH 8, 20 mM NaCl. **(B)** Remaining impurities were separated from AnPEP by elution from an anion exchange column (HiTrap Q HP) using a 1 M NaCl gradient. **(C)** Purified AnPEP from one capsule.

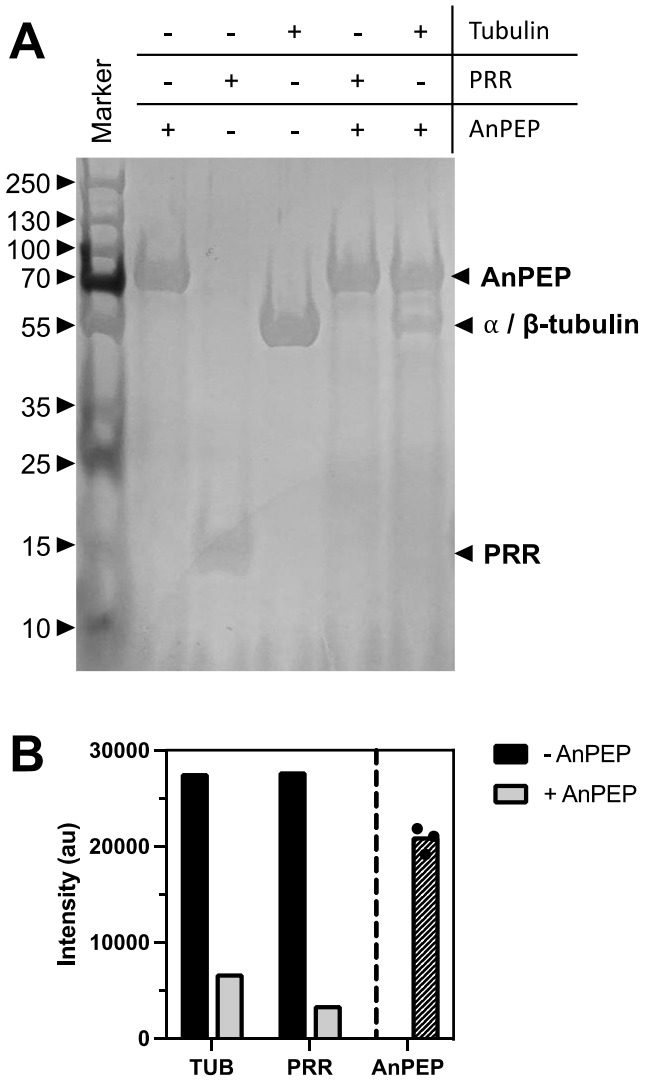

Figure 3.2 AnPEP digestion of PRR and tubulin.
(A) Purified *Aspergillus niger* prolyl endopeptidase (AnPEP) was co-incubated with either 50 µg of tubulin or PRR at 4°C then analyzed by SDS-PAGE. **(B)** Gel bands were quantified using ImageJ. Protein in the absence of AnPEP (*black*) exhibits a loss of signal upon AnPEP addition (*grey*). The average intensity of all PEP bands depicted as a *dashed grey* bar, with dots representing each individual measurement.

By coupling a commonly used pepsin column with an *Aspergillus niger* prolyl endopeptidase (AnPEP) column for PRR digest prior to mass spectrometry analysis, we were able to obtain complete coverage of the PRR, with multiple peptides for all regions (Figure 3.3). Our results returned digestion patterns similar to a prior application of AnPEP in HDX-MS [196], in that we observed short peptides (>4 residues, likely due to AnPEP activity) alongside longer peptides (up to 47 residues) that can be generated with pepsin alone. Shorter peptides can increase sequence resolution and therefore may more accurately reflect changes in exchange than longer peptides covering the same region [196].

We sought to not only characterize PRR and its dynamics with tubulin but also to understand how phosphomimics could potentially alter this interaction. Due to the significant diminishment in tubulin binding and polymerization by PRR_{4P} relative to PRR_{WT}, we chose these constructs for comparison. For both constructs, deuterium exchange occurred rapidly (Figure 3.4), a behavior that has also been observed for tau in other HDX-MS experiments [197]. In our case, deuterium dynamics for most peptides stabilized by the 30 sec timepoint, and thus this timepoint was chosen as a point of comparison between samples (Figure 3.4).

Our initial measurements compared PRR_{WT} with PRR_{4P} in the absence of tubulin. We identified 71 and 75 unique peptides for PRR_{WT} and PRR_{4P}, respectively, with 40 of these peptides present in both samples (Figure 3.3). A smaller number of peptides were identified in PRR_{4P} than in PRR_{WT} (240 as compared to 284), plausibly due to the presence of phosphomimics altering protease digestion patterns. For comparison, we constructed a difference map of the percent deuterium exchange for all peptides shared between the two samples (Figure 3.5).

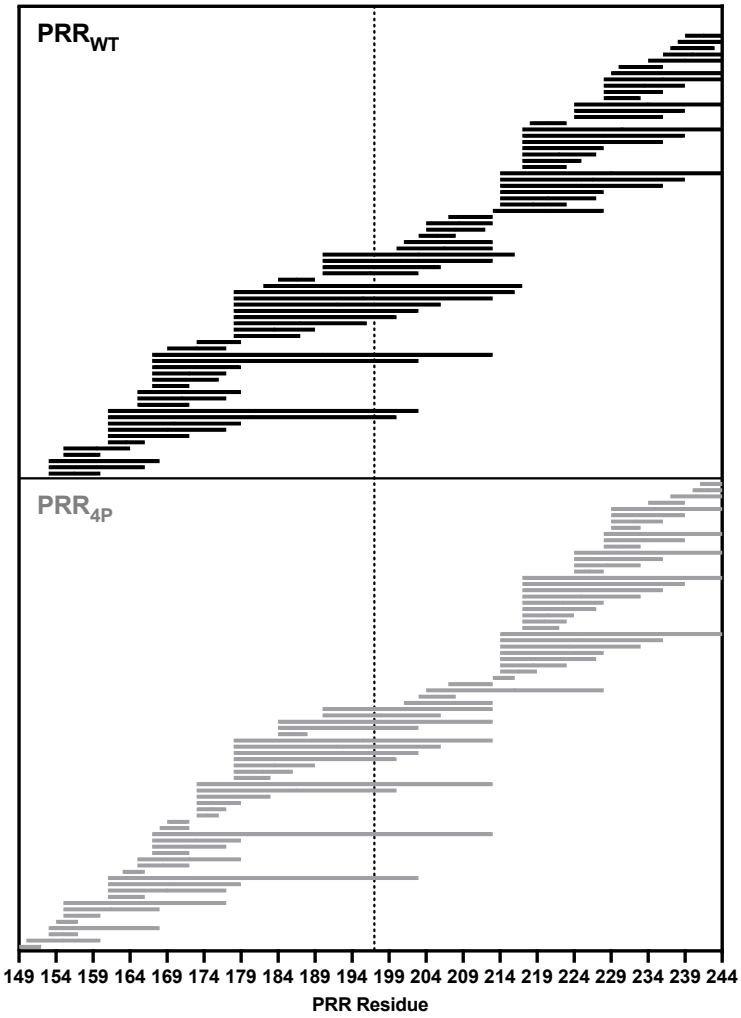

Figure 3.3 Peptide coverage for PRR$_{WT}$ and PRR$_{4P}$ in HDX-MS experiments.
Aspergillus niger prolyl endopeptidase (AnPEP) is complementary to pepsin and allows for nearly complete coverage of the PRR$_{WT}$ (black) or PRR$_{4P}$ (gray). Each horizontal bar represents a unique peptide identified (71 and 75 peptides for PRR$_{WT}$ and PRR$_{4P}$ respectively). For the PRR constructs investigated here, 40 peptides were present in both peptide lists. The dotted line delineates P1 (left) and P2 (right) of PRR$_{WT}$ or PRR$_{4P}$ as indicated. For complete peptide lists refer to 3.4 Appendix.

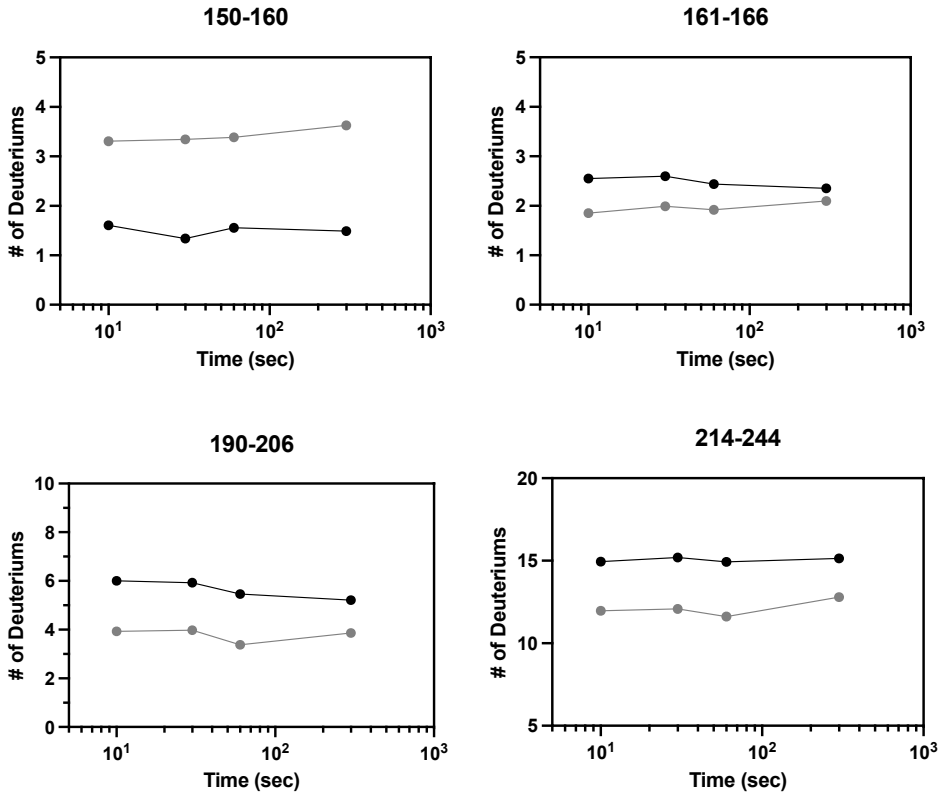

Figure 3.4 Kinetic deuterium uptake profiles for selected peptides.
Deuterium uptake measurements for PRR_{WT} (black) or PRR_{4P} (gray) in the absence of tubulin at several time points from HDX-MS experiments. Select peptides are representative of behaviors observed in individual peptides for PRR constructs.

Overall, PRR_{WT} demonstrates more exchange than PRR_{4P} (Figure 3.5B). Peptides covering residues ~165-179, ~207-223 and ~224-239 show a greater protection from exchange in PRR_{WT} than they do in PRR_{4P} (Figure 3.5B). Three of the four phosphomimic sites are found within these peptides, suggesting that while differences are seen throughout the protein sequence, the major impact is near the mutation sites.

HDX-MS measurements were also carried out for PRR constructs in the presence of tubulin. For PRR_{WT}, tubulin binding generally decreased deuterium uptake across the entire length of the protein (Figure 3.5C). This suggests that the much of this domain interacts with tubulin, at least transiently. Peptides covering two regions ~165-179 and ~224-239 reflect more enhanced protection, followed by ~207-223; interestingly, the former is directly adjacent to the T181 phosphorylation site while the latter region encompasses the T231 and S235 phosphorylation sites. In contrast, PRR_{4P} shows much less protection in the presence of tubulin (Figure 3.5D). This is likely because much of the protein is not bound to tubulin, or bound only very transiently, due to its reduced affinity as seen in the previous chapter. However, the regions that show the most protection from exchange in PRR_{WT} are also amongst the more highly protected in PRR_{4P}. This suggests that while the phosphomimics reduce binding of PRR to tubulin, the regions involved in binding are not significantly altered.

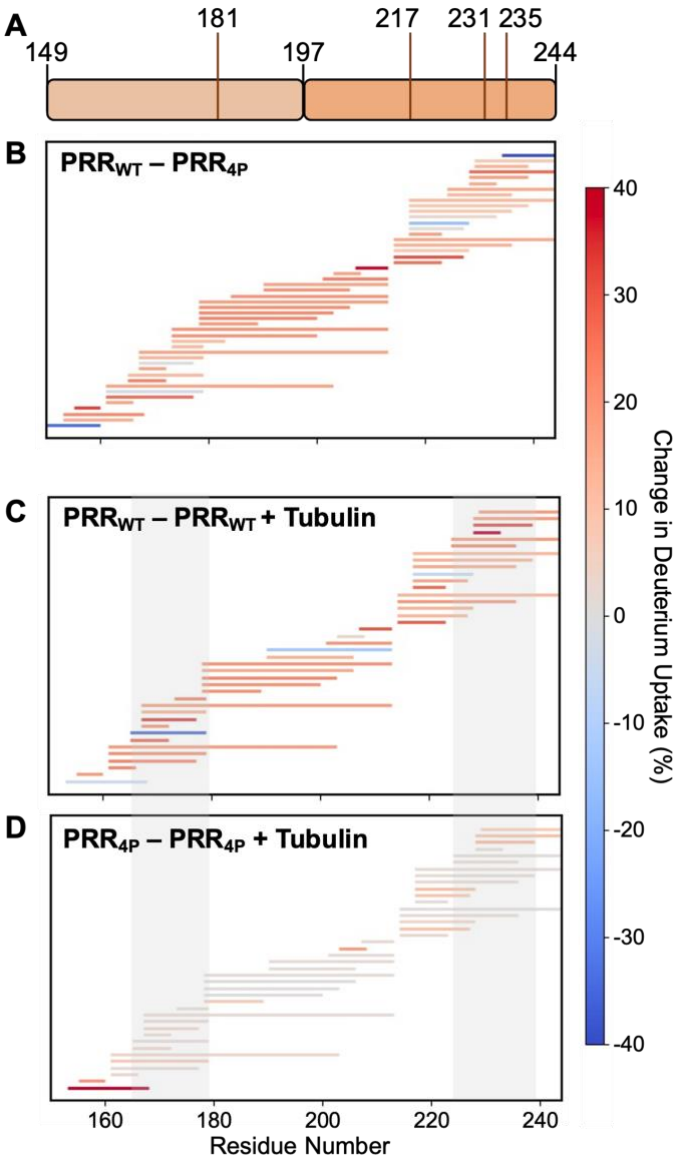

Figure 3.5 Phosphorylation and tubulin binding result in reduced protein dynamics.
(A) Schematic of PRR with phosphomimic sites indicated. **(B-D)** Map of digested PRR_{WT} or PRR_{4P} peptides observed in HDX-MS experiments. Each horizontal bar represents a unique peptide identified in both samples. Data for each peptide is representative of $n \geq 3$ independent measurements. The ratio of measured over maximum expected deuteriums were determined for each peptide. The horizontal bars are color coded based on the average difference in deuterium uptake reported as percent uptake. The regions shaded in gray highlight PRR residues 165-179 and 224-239.

3.3 Discussion

HDX-MS can identify regions of a protein that are exposed differentially based on structural changes that can occur upon ligand or cofactor binding [198]. Here, we examined both PRR_{WT} with PRR_{4P} in the presence and absence of tubulin to identify regions of PRR involved in tubulin binding and how these regions are impacted by phosphomimics.

Generally, PRR_{WT} has an increase in protection throughout the PRR sequence in the presence of tubulin, suggesting that much of the protein associates, at least transiently, with the tubulin surface (Figure 3.5C). Similar binding models have been suggested for MTBR binding to microtubules, in which, although specific residues are important for binding, the entire region is associated with the microtubule lattice. IDPs have been observed to bind to multiple binding partners transiently but with high specificity [12].

Disordered proteins often interact with binding partners through short stretches of residues or short linear motifs or SLiMs [199]. Our HDX-MS measurements identify two stretches of residues within the PRR that are more protected from exchange in the PRR-tubulin complex, ~165-179 and ~224-239 (Figure 3.5). Part of the PRR (166-246) was also shown to bind weakly to taxol-stabilized microtubules by electron microscopy [138] which includes the ~165-179 region we observe to be more protected from exchange by HDX-MS. Interestingly, the latter ~224-239 region encompasses a stretch of residues first identified by Feinstein and coworkers more than 25 years ago [174], 224-230 (identical to 215-221 in their study) as strongly influencing microtubule binding and assembly in fragments of tau containing the MTBR. Although the PRR was not resolved in a recent cryo-EM structure of tau bound to tubulin, the P2 (197-244) was used to enhance binding to obtain higher resolution structures [135].

Relative to PRR_{WT}, PRR_{4P} has less deuterium exchange overall (Figure 3.5A). With PRR_{4P} exhibiting little protection from exchange outside of the primary binding sites (Figure 3.5D) suggesting that PRR_{4P} is not stably associated with tubulin over the timescale of the HDX-MS measurements. Even though HDX-MS reports on the average behavior of the complex, the lack of association between PRR_{4P} and tubulin is supported by our FCS data which also indicates faster off-rates for PRR_{4P}.

These regions not only include or are directly adjacent to three of the four phosphomimics examined here, but also cover many of the other phosphorylation sites that are potentially phosphorylated both in healthy control and Alzheimer's disease brains [74]. Together, this suggests that the regions involved in PRR:tubulin binding are not significantly altered despite phosphomimics reducing binding capability of PRR to tubulin. However, future HDX-MS studies should focus on characterizing changes in tubulin dynamics due to the PRR.

3.4 Appendix: Peptide lists used for HDX-MS

A coupled *Aspergillus niger* prolyl endopeptidase (AnPEP) and pepsin column were used to digest PRR_{WT} or PRR_{4P} in the presence and absence of tubulin. The peptide lists generated by these reactions are tabulated with numbering of the residues based on 2N4R. There are 106 unique peptides identified, and of these, 40 peptides are shared between both PRR constructs (indicated with an asterisk). For peptides present in both PRR_{WT} and PRR_{4P} peptide lists, phosphomimic mutations within these peptides are indicated as follows: (PRR_{WT} residue / PRR_{4P} residue).

	Peptide	Peptide Length
	149-CKIA-152	4
	150-KIATPRGAAPP-160	11
	153-TPRGA-157	5
	153-TPRGAAPP-160	8
	153-TPRGAAPPGQKGQA-166	14
*	153-TPRGAAPPGQKGQANA-168	16
	154-PRGA-157	4
*	155-RGAAPP-160	6
	155-RGAAPPGQKG-164	10
	155-RGAAPPGQKGQANA-168	14
	155-RGAAPPGQKGQANATRIPAKTPP-177	23
*	161-GQKGQA-166	6
	161-GQKGQANATRIP-172	12
*	161-GQKGQANATRIPAKTPP-177	17
*	161-GQKGQANATRIPAKTPPAP-179	19
	161-GQKGQANATRIPAKTPPAPKTPPSSGEPPKSGDRSGYSSP-200	40
*	161-GQKGQANATRIPAKTPPAPK(T/E)PPSSGEPPKSGDRSGYSSPGSP-203	43
	163-KGQA-166	4
*	165-QANATRIP-172	8
	165-QANATRIPAKTPP-177	13
*	165-QANATRIPAKTPPAP-179	15
*	167-NATRIP-172	6
	167-NATRIPAKTP-176	10
*	167-NATRIPAKTPP-177	11
*	167-NATRIPAKTPPAP-179	13
	167-NATRIPAKTPPAPKTPPSSGEPPKSGDRSGYSSPGSP-203	37
*	167-NATRIPAKTPPAPK(T/E)PPSSGEPPKSGDRSGYSSPGSPGTPGSRSRTP-213	47
	168-ATRIP-172	5
	169-TRIP-172	4

	169-TRIPAKTPP-177	9
	173-AKTP-176	4
	173-AKTPP-177	5
*	173-AKTPPAP-179	7
	173-AKTPPAPKEPP-183	11
	173-AKTPPAPKEPPSSGEPPKSGDRSGYSSP-200	28
	173-AKTPPAPKEPPSSGEPPKSGDRSGYSSPGSPGTPGSRSRTP-213	41
	178-APKEPP-183	6
	178-APKEPPSSG-186	9
	178-APKTPPSSGE-187	10
*	178-APK(T/E)PPSSGEPP-189	12
	178-APKTPPSSGEPPKSGDRSG-196	19
*	178-APK(T/E)PPSSGEPPKSGDRSGYSSP-200	23
*	178-APK(T/E)PPSSGEPPKSGDRSGYSSPGSP-203	26
*	178-APK(T/E)PPSSGEPPKSGDRSGYSSPGSPGTP-206	29
*	178-APK(T/E)PPSSGEPPKSGDRSGYSSPGSPGTPGSRSRTP-213	36
	178-APKTPPSSGEPPKSGDRSGYSSPGSPGTPGSRSRTPSLP-216	39
	182-PPSSGEPPKSGDRSGYSSPGSPGTPGSRSRTPSLPT-217	36
	184-SSGEP-188	5
	184-SSGEPP-189	6
	184-SSGEPPKSGDRSGYSSPGSP-203	20
	184-SSGEPPKSGDRSGYSSPGSPGTPGSRSRTP-213	30
	190-KSGDRSGYSSPGSP-203	14
*	190-KSGDRSGYSSPGSPGTP-206	17
*	190-KSGDRSGYSSPGSPGTPGSRSRTP-213	24
	190-KSGDRSGYSSPGSPGTPGSRSRTPSLP-216	27
	200-PGSPGTPGSRSRTP-213	14
*	201-GSPGTPGSRSRTP-213	13
*	203-PGTPGS-208	6
	204-GTPGSRSRT-212	9
	204-GTPGSRSRTP-213	10
	204-GTPGSRSRTPSLPEPPTREPKKVAV-228	25
*	207-GSRSRTP-213	7
	213-PSLP-216	4
	213-PSLPTPPTREPKKVAV-228	16
	214-SLPEPP-219	6
*	214-SLP(T/E)PPTREP-223	10
*	214-SLP(T/E)PPTREPKKVA-227	14
*	214-SLP(T/E)PPTREPKKVAV-228	15

	214-SLPEPPTREPKKVAVVREPP-233	20
*	214-SLP(T/E)PPTREPKKVAVVR(T/E)PPK(S/E)P-236	23
	214-SLPTPPTREPKKVAVVRTPPKSPSSA-239	26
*	214-SLP(T/E)PPTREPKKVAVVR(T/E)PPK(S/E)PSSAKSRLQ-244	31
	217-EPPTRE-222	6
*	217-(T/E)PPTREP-223	7
	217-EPPTREPK-224	8
	217-TPPTREPKK-225	9
*	217-(T/E)PPTREPKKVA-227	11
*	217-(T/E)PPTREPKKVAV-228	12
	217-EPPTREPKKVAVVREPP-233	17
*	217-(T/E)PPTREPKKVAVVR(T/E)PPK(S/E)P-236	20
*	217-(T/E)PPTREPKKVAVVR(T/E)PPK(S/E)PSSA-239	23
*	217-(T/E)PPTREPKKVAVVR(T/E)PPK(S/E)PSSAKSRLQ-244	28
	218-PPTREP-223	6
	224-KKVAV-228	5
	224-KKVAVVREPP-233	10
*	224-KKVAVVR(T/E)PPK(S/E)P-236	13
	224-KKVAVVRTPPKSPSSA-239	16
*	224-KKVAVVR(T/E)PPK(S/E)PSSAKSRLQ-244	21
*	228-VVR(T/E)PP-233	6
	228-VVRTPPKSP-236	9
*	228-VVR(T/E)PPK(S/E)PSSA-239	12
*	228-VVR(T/E)PPK(S/E)PSSAKSRLQ-244	17
	229-VREPP-233	5
	229-VREPPKEP-236	8
	229-VREPPKEPSSA-239	11
*	229-VR(T/E)PPK(S/E)PSSAKSRLQ-244	16
	230-RTPPKSP-236	7
	234-KEPSSA-239	6
	234-KSPSSAKSRLQ-244	11
	236-PSSAKSRLQ-244	9
	237-SSAKSRL-243	7
	237-SSAKSRLQ-244	8
	238-SAKSRLQ-244	7
	239-AKSRLQ-244	6
	240-KSRLQ-244	5
	241-SRLQ-244	4

CHAPTER 4: PRR INTERACTS PREDOMINANTLY WITH THE α-TUBULIN SUBUNIT

Part of this chapter is adapted from Karen Acosta, Christopher Brue, Hee Jong Kim, Polina Holubovska, Leland Mayne, Kenji Murakami, Elizabeth Rhoades, "Structural Insights into the Role of the Proline Rich Region in Tau Function" (*submitted*)

I collected all the data in this chapter except for the XL-MS measurements completed by Hee Jong Kim.

4.1 Introduction

We have established that phosphomimics in the PRR region decrease tubulin and microtubule binding. This loss of PRR affinity for tubulin due to phosphomimics diminishes microtubule polymerization and PRR:tubulin dynamics ultimately suggesting faster off rates of phosphorylated constructs relative to PRR_{WT}. In this chapter, we use a structural mass spectrometry technique, cross-linking mass spectrometry (XL-MS), to examine PRR:tubulin interaction sites.

XL-MS can be used to identify interaction sites between or within proteins and provide distance restraints to predict and validate protein models [200-202]. In XL-MS the protein of interest is incubated with a crosslinking reagent that covalently binds reactive groups of residues that are in close proximity. Thereafter, the cross-linking reaction is enzymatically digested, and the peptide mixture is evaluated by liquid chromatography-tandem mass spectrometry (LC-MS/MS). Both connected peptides and cross-link positions can be determined from the tandem mass spectra. Typically, crosslinkers used in these reactions contain two NHS- (N-hydroxysuccinimide-) ester functional groups on each end of a spacer arm that primarily targets lysine amino acids [203, 204]. The inclusion of MS-cleavable groups, and other functionalities, to decorate the spacer arm can also aide in the identification or enrichment of cross-linked peptides

[205-207]. Since a cross-linker has a defined length connected by covalent bonds between the functional groups of amino acids, cross-links impose distance constraints on proteins or protein-protein complexes.

As before, due to the significant differences between PRR_{WT} and PRR_{4P} binding, polymerization, and dynamics with both tubulin and microtubules, we focused on these two constructs to examine by XL-MS. For these experiments, DSBU was used for cross-linking reactions containing tubulin and PRR (PRR_{WT} or PRR_{4P}) to identify interactions between PRR:tubulin residues. By mapping these cross-links on a cryo-EM structure of taxol-stabilized microtubule, we develop a model in which PRR enhances lateral interactions between tubulin dimers.

4.2 Results

Cross-linking mass spectrometry (XL-MS) can be used to provide information on the structure of proteins and protein complexes by identifying residue pairs within close spatial proximity [208-210]. To develop further insight into tau-tubulin interactions, we used XL-MS to map sites of interaction between PRR and tubulin. For these reactions, we used disuccinimidyl dibutyric urea (DSBU) as our cross-linker. DSBU has an amine-reactive NHS-ester with an 11-atom spacer arm (12.5 Å) and is MS-cleavable, which assists in the identification of cross-linked peptides.

The addition of DSBU to PRR-tubulin mixtures results in several bands that run larger than the ~55 kDa α/β-tubulin monomer band by SDS-PAGE (Figure 4.1), corresponding to various stoichiometries of α/β-tubulin and PRR. Our FCS results would suggest that PRR would be found associated to tubulin with a 1:2 PRR:tubulin stoichiometry consistent with an expected molecular weight of ~125 kDa. We observe pronounced bands for each PRR construct and tubulin; however, the next major band corresponds to a molecular weight of ~130 kDa further suggesting that this 1:2 ratio of PRR:tubulin is the preferred binding ratio. We excised lower gel bands ~55 – 115 kDa and higher gel bands ~115 – 300 kDa for further analysis. Hereafter, unless otherwise indicated, the cross-linked results are representative of the cumulative cross-linking reactions of both the "lower" and "higher" gel bands combined to facilitate comparison. To examine the effect of phosphomimics on PRR:tubulin cross-linking sites, both PRR constructs (PRR_{WT} or PRR_{4P}) were evaluated in the presence of tubulin (Figure 4.1). Cross-linked peptides were identified by mass spectrometry and cross-links with a false discovery rate (FDR) of 1% or lower were not interpreted.

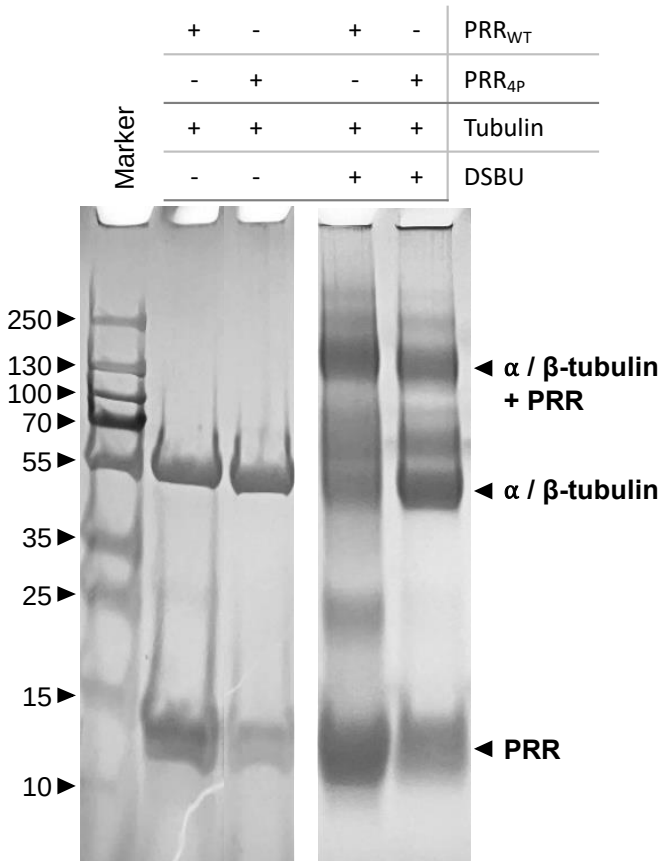

Figure 4.1 Cross-linking gel of PRR constructs and tubulin.
50 μg of purified PRR (PRR$_{WT}$ or PRR$_{4P}$) and 50 μg of purified tubulin were mixed with 6 mM DSBU in phosphate buffer (20 mM phosphate buffer pH 7.4, 20 mM KCl, 1 mM MgCl2, 0.5 mM EGTA, and 1 mM DTT). The cross-linked reactions were quenched with ammonium bicarbonate and analyzed by SDS-PAGE. Both PRR$_{WT}$ and PRR$_{4P}$ form high molecular weight assemblies with tubulin upon the addition of crosslinker DSBU.

Our HDX-MS measurements suggest that like the MTBR, much of the PRR interacts with the tubulin surface upon binding, although dynamically. We collected a total of 595 cross-links containing either our PRR construct or tubulin, with 188 and 407 cross-links associated with the PRR_{WT} and PRR_{4P} reactions, respectively. For both samples, cross-links were observed within and between the α/β tubulin monomer units, as well as between PRR peptides (Figure 2.3).

We primarily focus our analysis on PRR-tubulin cross-links, where there is significant overlap in the cross-linking sites found in PRR_{WT} and PRR_{4P}, with K163 occurring as the most frequent cross-link position for both in the PRR, followed by K174. These residues are found directly adjacent to or within the ~165-179 region identified by HDX-MS as protected from exchange in the presence of tubulin (Figure 2.3). Additional sites present in both PRR_{WT} and PRR_{4P} are K224, K225 and K240. Although not as abundant as the K163 and K174 cross-links K224, K225 and K240 cross-links flank either side of the ~224-239 region identified by HDX-MS as another putative tubulin binding site (Figure 2.3). Interestingly, however, cross-links are notably absent at lysine residues in proximity to two of the phosphorylation sites we tested, T231/S235 (K234). This suggests that the reduced binding observed for phosphomimics at these positions may be primarily due to electrostatic repulsion [211] rather than disruption of specific interactions with these residues and the tubulin surface. PRR shows a preference for interactions with sites located on α-tubulin, with 58% of total PRR-tubulin cross-links (Figure 2.3). The most common cross-link sites on α-tubulin were K96 and K112; however, K370, K394 and K401 were also identified in both PRR samples. On β-tubulin, K58 was the most abundant cross-linking site, with additional sites at K216 and K252 (Figure 2.3).

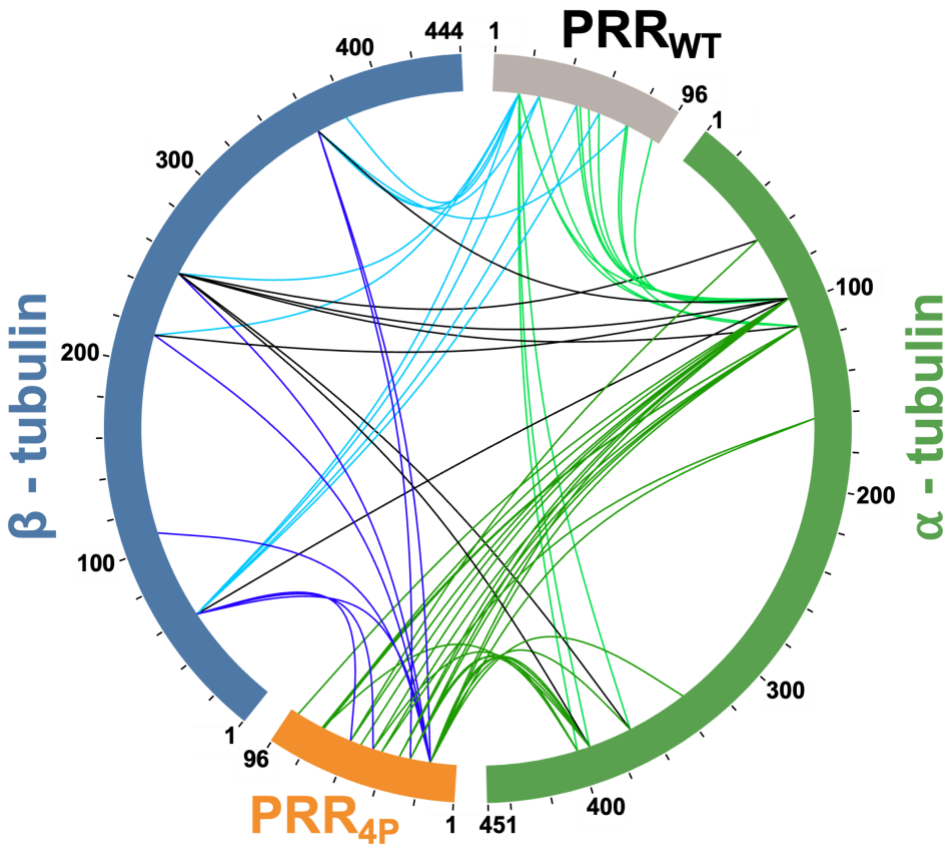

Figure 4.2 Circle diagram of PRR:tubulin cross-links.
PRR constructs (PRR_{WT} or PRR_{4P}) were cross-linked with DSBU in the presence of tubulin. All PRR:tubulin cross-links observed are shown as a circle diagram visualized by xiView [212]. Cross-link colors are as follows: PRRWT:α-tubulin (light green), PRR4P:α-tubulin (dark green), PRRWT:β-tubulin (light blue), PRR4P:β-tubulin (dark blue), and α-tubulin:β-tubulin (black). Refer to Appendix I for list of cross-linked PRR:tubulin residues.

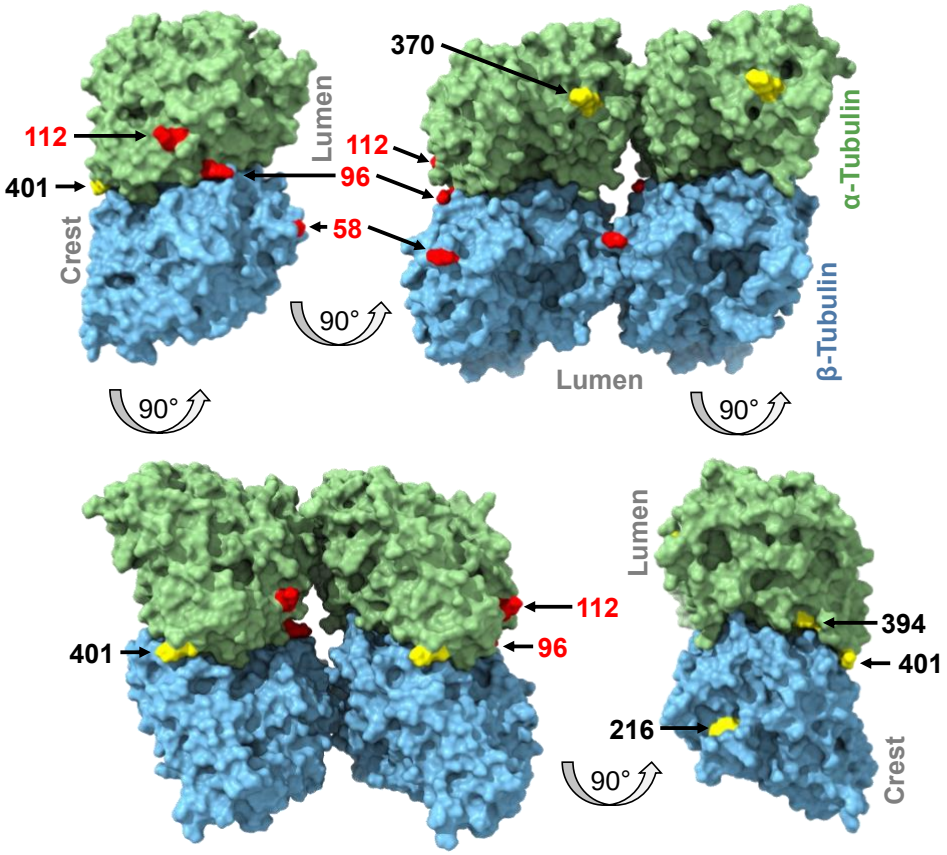

Figure 4.3 Cross-linking reveals specific PRR interactions with tubulin subunits.
PRR constructs (PRR_{WT} or PRR_{4P}) were cross-linked with DSBU in the presence of tubulin. PRR_{WT}:α/β-tubulin and PRR_{4P}:α/β-tubulin cross-links were mapped on the cryo-EM structure of taxol stabilized microtubules (PDB: 6WVL) using ChimeraX 1.5 [213]. The most abundant cross-link sites are colored red (α-tubulin: K96, K112; β-tubulin: K58) with secondary sites in yellow (α-tubulin: K370, K394, K401; β-tubulin: K216, K252). Refer to Appendix I for list of cross-linked PRR:tubulin residues.

As mentioned previously, the cross-linking reactions were analyzed separately for lower molecular weight bands from ~55 – 115 kDa and a second range of higher gel bands from ~115 – 300 kDa (Figure 4.1). Overall, the pattern of PRR:tubulin cross-links is maintained irrespective of the gel fraction examined (Figure 4.4). For the lower range of gel bands, we observe more self-cross-links of both the PRR constructs (PRR_{WT} and PRR_{4P}) and tubulin (Figure 4.4). However, the higher molecular weight range does show some inter-subunit crosslinks that are not present at lower molecular weights. The small differences between the molecular weight ranges highlight that the bands observed by SDS-PAGE are composed of a mixture of PRR:tubulin stoichiometries not dissimilar to the heterogeneity of tau:tubulin complexes previously observed for the MTBR [131].

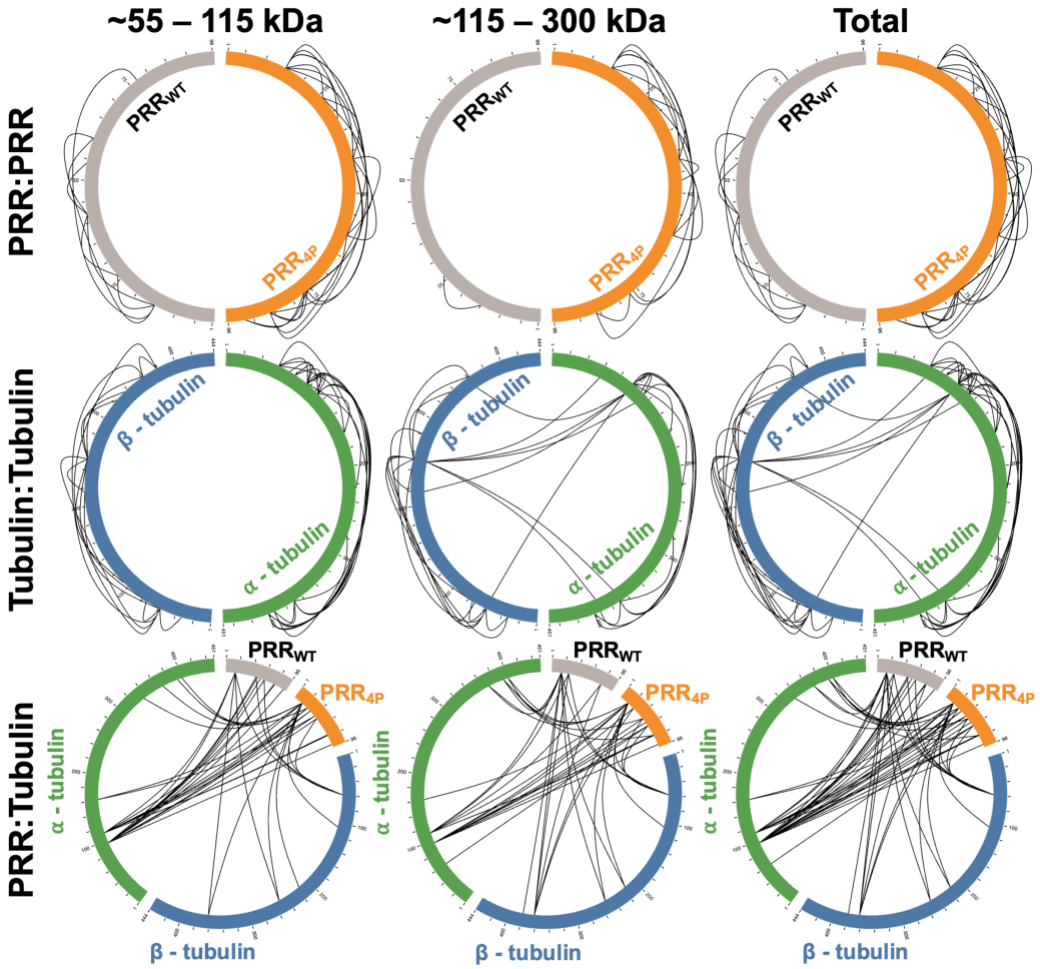

Figure 4.4 Circle diagrams of cross-links separated by gel fraction.
PRR constructs (PRR_{WT} or PRR_{4P}) were cross-linked with DSBU in the presence of tubulin and analyzed by SDS-PAGE (refer to Figure 4.1). Lower (~55 – 115 kDa) and higher (~115 – 300 kDa) gel bands were excised and analyzed separately. Cross-links visualized by xiView [212] are represented as a circle diagram. Refer to Appendix I-III for list of cross-linked residues.

4.3 Discussion

The XL-MS results provide further insight into PRR binding sites on tubulin and, importantly, how these may differ with microtubules. In particular, some tubulin residues available in soluble tubulin are obscured by neighboring tubulin dimers in microtubules. Of the cross-links identified in this study, K370 on α-tubulin and K58 on β-tubulin each face the luminal side of a microtubule, while K96 on α-tubulin and K58 on β-tubulin are buried by lateral or longitudinal contacts between dimers (Figure 4.3). These tubulin sites that are not accessible in microtubules may reflect the interactions important for initial association of PRR with soluble tubulin to initiate polymerization. The cross-linked sites found on the opposite sides of α-tubulin subunit, K112 and K401, are accessible on the outside of the microtubule (Figure 4.3). Moreover, single molecule FRET measures ~90 Å RMS of PRR_{WT} bound to tubulin [141] approximately the span of two laterally adjacent tubulin subunits.

NHS esters like DSBU react primarily with lysine residues but can also react with serine, threonine and tyrosine [204, 214]. In our reactions, we observe predominantly lysine residues with some reactivity with these additional residues. Notably, not every lysine residue in PRR was cross-linked indiscriminately, emphasizing that these observations are relevant to PRR:tubulin binding interactions. For example, we do not observe cross-links with K150 in either PRR construct, and this residue also lies outside of the more dynamic regions identified by HDX-MS (~165-179 and ~224-239, refer to Chapter 3). Conversely, the remaining lysine in the PRR, K234, is likely influenced by neighboring phosphomimics at residues T231 and S235.

Collectively, our data leads us to propose a model whereby PRR stabilizes lateral interactions between tubulin dimers (Figure 4.3). This is in contrast to the structural model derived from full-length tau, where the MTBR was found to bind longitudinally along the crest of the

microtubule protofilament[135]. It is of note that the tubulin binding sites identified for PRR in this study do not overlap with the binding sites of MTBR such that both regions could be bound simultaneously (Figure 4.3). This also allows for the possibility of conditions where MTBR anchors tau to the microtubule, while PRR plays a role in attracting tubulin dimers or other binding partners to the microtubule lattice.

XL-MS can provide distance restraints that are then used to either create structural ensembles [215, 216] or map onto previously identified ensembles [217-219]. A recent study used restraints obtained from XL-MS experiments to generate molecular dynamics simulations to create monomeric model tau structures [220]. However, these models were predominantly globular in nature, despite ample evidence that tau can populate more elongated states within the ensemble of structures possible [37, 43, 221]. This overrepresentation of globular states has also been observed for models based on cross-linking measurements for other systems [218]. Although it remains challenging to accurately model disordered proteins, future studies can use the distance restraints observed here in combination with the other biophysical and biochemical data acquired from this work to assist in the generation of future tau:tubulin models and simulations.

4.4 Appendix I: List of PRR:Tubulin Cross-links

PRR constructs (PRR_{WT} or PRR_{4P}) and tubulin were cross-linked with MS-cleavable cross-linker DSBU. We identified a total of 595 cross-links containing either our PRR construct or tubulin, with 188 and 407 cross-links associated with the PRR_{WT} and PRR_{4P} reactions, respectively.

There are 172 PRR:tubulin cross-links, and of these 57 are associated with PRR_{WT} and 115 with PRR_{4P}. The 26 PRR_{WT}:α-tubulin and 73 PRR_{WT}:α-tubulin cross-links are tabulated below by frequency and sorted by PRR residue.

PRR Residue	α-Tubulin Residue	Frequency		
		PRR_{WT}	PRR_{4P}	Total
163	96	3	4	7
163	112	5	14	19
163	163	0	2	2
163	336	0	2	2
163	370	1	3	4
163	394	1	8	9
163	401	2	2	4
174	96	0	3	3
174	112	2	2	4
174	394	0	1	1
174	401	0	1	1
180	96	0	1	1
180	112	0	2	2
190	112	0	2	2
190	163	0	2	2
195	96	1	5	6
195	394	0	1	1
197	96	1	0	1
202	96	1	2	3
208	60	0	1	1
208	96	1	1	2
224	96	2	3	5
224	112	0	3	3
225	112	5	4	9
225	394	0	1	1
240	96	1	3	4

PRR constructs (PRR_{WT} or PRR_{4P}) and tubulin were cross-linked with MS-cleavable cross-linker DSBU. We identified a total of 595 cross-links containing either our PRR construct or tubulin, with 188 and 407 cross-links associated with the PRR_{WT} and PRR_{4P} reactions, respectively.

There are 172 PRR:tubulin cross-links, and of these 57 are associated with PRR_{WT} and 115 with PRR_{4P}. The 31 PRR_{WT}:β-tubulin and 42 PRR_{WT}:β-tubulin cross-links are tabulated below by frequency and sorted by PRR residue.

PRR Residue	β-Tubulin Residue	Frequency		
		PRR_{WT}	PRR_{4P}	Total
163	58	10	9	19
163	107	0	2	2
163	216	1	7	8
163	252	9	11	20
163	362	4	3	7
163	379	1	0	1
174	58	1	0	1
174	362	1	1	2
195	58	1	3	4
208	58	2	6	8
225	362	1	0	1

4.5 Appendix II: List of PRR:PRR Cross-links

PRR constructs (PRR_{WT} or PRR_{4P}) and tubulin were cross-linked with MS-cleavable cross-linker DSBU. We identified a total of 595 cross-links containing either our PRR construct or tubulin, with 188 and 407 cross-links associated with the PRR_{WT} and PRR_{4P} reactions, respectively.

There are 169 PRR:PRR cross-links. The 37 PRR_{WT}: PRR_{WT} and 132 PRR_{4P}: PRR_{4P} cross-links are tabulated below by frequency and sorted by PRR residue.

PRR Residue	PRR Residue	Frequency		
		PRR_{WT}	PRR_{4P}	Total
163	163	5	5	10
163	174	12	16	28
163	190	3	2	5
163	208	1	3	4
163	225	1	4	5
163	234	0	5	5
180	163	0	7	7
190	163	0	6	6
190	174	12	37	49
190	195	0	1	1
190	202	2	0	2
190	208	1	5	6
190	225	0	3	3
190	234	0	2	2
208	174	0	2	2
208	234	0	1	1
224	163	0	6	6
224	190	0	3	3
224	234	0	6	6
225	225	0	2	2
234	225	0	9	9
240	224	0	1	1
240	225	0	6	6

4.6 Appendix III: List of Tubulin:Tubulin Cross-links

PRR constructs (PRR_{WT} or PRR_{4P}) and tubulin were cross-linked with MS-cleavable cross-linker DSBU. We identified a total of 595 cross-links containing either our PRR construct or tubulin, with 188 and 407 cross-links associated with the PRR_{WT} and PRR_{4P} reactions, respectively.

There are 254 tubulin:tubulin cross-links, and of these 117 are α-tubulin:α-tubulin cross-links. The 43 α-tubulin:α-tubulin cross-links in PRR_{WT} and 74 α-tubulin:α-tubulin cross-links in PRR_{4P} are tabulated below by frequency and sorted by α-tubulin residue.

α-Tubulin Residue	α-Tubulin Residue	Frequency		
		PRR_{WT}	PRR_{4P}	Total
60	96	0	1	1
60	112	0	2	2
60	163	0	1	1
60	394	0	1	1
96	73	0	1	1
96	80	1	0	1
96	96	1	2	3
96	108	4	5	9
96	112	22	27	49
96	163	0	2	2
96	223	0	1	1
96	225	2	0	2
96	370	1	3	4
96	394	3	12	15
96	401	5	4	9
112	80	0	1	1
112	163	1	3	4
112	394	0	1	1
112	401	0	1	1
370	112	1	1	2
370	277	1	1	2
370	394	0	3	3
370	401	1	1	2

PRR constructs (PRR_{WT} or PRR_{4P}) and tubulin were cross-linked with MS-cleavable cross-linker DSBU. We identified a total of 595 cross-links containing either our PRR construct or tubulin, with 188 and 407 cross-links associated with the PRR_{WT} and PRR_{4P} reactions, respectively.

There are 254 tubulin:tubulin cross-links, and of these 115 are β-tubulin:β-tubulin cross-links. The 44 β-tubulin:β-tubulin cross-links in PRR_{WT} and 71 β-tubulin:β-tubulin cross-links in PRR_{4P} are tabulated below by frequency and sorted by β-tubulin residue.

β-Tubulin Residue	β-Tubulin Residue	Frequency		
		PRR_{WT}	PRR_{4P}	Total
33	58	1	3	4
33	252	0	1	1
58	75	3	3	6
58	252	31	47	78
58	281	1	0	1
72	252	1	0	1
75	252	0	2	2
107	252	0	1	1
216	58	1	0	1
216	252	1	2	3
252	252	0	1	1
324	252	0	2	2
336	252	1	1	2
362	58	2	4	6
362	252	0	3	3
362	379	0	1	1
379	58	2	0	2

PRR constructs (PRR_{WT} or PRR_{4P}) and tubulin were cross-linked with MS-cleavable cross-linker DSBU. We identified a total of 595 cross-links containing either our PRR construct or tubulin, with 188 and 407 cross-links associated with the PRR_{WT} and PRR_{4P} reactions, respectively.

There are 254 tubulin:tubulin cross-links, and of these 22 are α-tubulin:β-tubulin cross-links. The 7 α-tubulin:β-tubulin cross-links in PRR_{WT} and 15 α-tubulin:β-tubulin cross-links in PRR_{4P} are tabulated below by frequency and sorted by α-tubulin residue.

α-Tubulin Residue	β-Tubulin Residue	Frequency		
		PRR_{WT}	PRR_{4P}	Total
60	252	2	1	3
96	58	1	1	2
96	216	0	1	1
96	252	2	5	7
96	362	0	1	1
112	252	1	5	6
370	252	1	0	1
394	252	0	1	1

CHAPTER 5: CONCLUSIONS AND PERSPECTIVES

The combination of biophysical approaches provided critical insights between tau and tubulin

In this work we use a collection of structural techniques to highlight the importance of the PRR and expand upon these findings by comparing the effects that increased phosphorylation can have on interactions between the PRR and tubulin. Through a combination of spectroscopic techniques, we find that the accumulation of phosphomimic modifications in the PRR decreases tubulin and microtubule binding affinity, and subsequently decreases tubulin-polymerization capacity (Chapter 2). With structural mass spectrometry we identify two potential tau:tubulin binding sites (~165-179 and ~224-239) (Chapter 3). We also find specific residues on PRR and tubulin that may play an important role in this interaction that also fall within or are directly adjacent to the binding sites identified by HDX-MS (Chapter 4). Namely the most frequently observed cross-links K163 and K174 lie within the P1 binding site (~165-179), and commonly appearing K225, K224, and K240 are associated with the second site (~224-239) (Chapter 4). Our study emphasizes the power of a combination of biophysical approaches to provide critical insights into the molecular details and structural features of a dynamic complex which may be challenging to characterize by traditional structural approaches.

Tau's binding sites for soluble tubulin dimers may not be the same for binding sites on microtubules

It is worth noting that it is frequently assumed that tau:tubulin interactions mirror tau:microtubule interactions. Initially this does appear to be true, since the MTBR binding site lies along the crest of the microtubule. Thus, the MTBR could bind to free tubulin in this position without sterically hindering the addition of these tubulin dimers to a growing microtubule, or binding to an established microtubule, as they do not share binding sites. However, there may be potential binding sites that can only be available in free tubulin, such as sites that are buried within the microtubule lattice or those which face the lumen of the microtubule. Directly challenging this convention of shared tubulin and microtubule binding sites is the PRR. For the PRR, we see that frequently observed crosslink sites lie along the tubulin dimer's side between the crest and the luminal side of the tubulin dimer (Chapter 4), near where tubulin dimers would be likely to interact with other dimers in a microtubule lattice.

This in turn leads us to propose a model whereby PRR enhances lateral interactions between tubulin dimers, with minimal overlap between its interaction with tubulin and the MTBR binding site (Figure 6.1). In which while MTBR anchors tau to the microtubule, PRR is available to play a role in attracting tubulin dimers or other binding partners to the microtubule lattice. In fact, there is evidence to suggest that tau may even bind more tightly to tubulin than to microtubules [222].

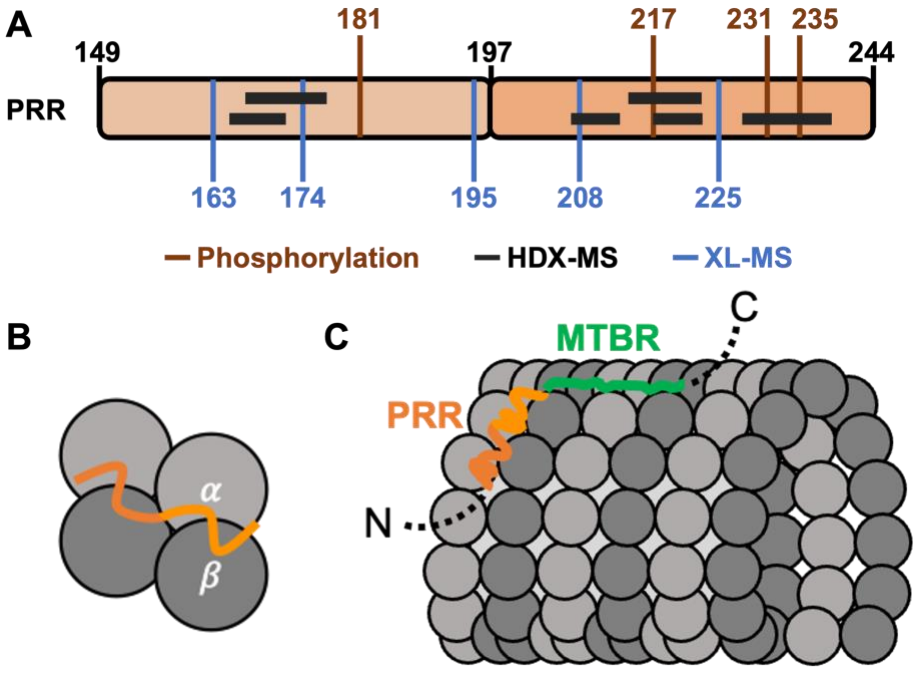

Figure 5.1 Model for PRR-tubulin interactions in full-length tau.
(A) PRR schematic split into two segments for P1 and P2, with phosphorylation sited indicated. Regions of highest protection from exchange and top cross-link sites are indicated. Model of tau with PRR (orange) bound to **(B)** two tubulin dimers or **(C)** microtubules with MTBR (green) along the crest of the protofilament. α-tubulin and β-tubulin are represented in light gray and dark gray respectively.

Tau's PRR: an understudied home of multiple tubulin binding sites

Portions of the PRR have long been identified to help promote microtubule polymerization [138-140]. Over 25 years ago, residues 224-KKVAVVR-230 located within the P2 (identical to 215-221 in their study) were determined to strongly influence microtubule binding and assembly in fragments of tau containing the MTBR [174]. Domain-centric approaches to investigating tau may have also inadvertently ignored the independent function of PRR, in part, due to the widespread use of tau construct K16, which contains P2 and the MTBR (K16 = P2-MTBR: residues 198-372) [140]. Similarly, studies which examine tau's projection domain (N-terminus-P1: residues 1-197) can obfuscate characteristics of the N-terminal inserts with that of the P1. Even though the P1 was recently shown to double tau's binding capacity to tubulin dimers and can bind to tubulin independently [141].

There is a growing amount of evidence to suggest that the PRR has two main binding sites. NMR measurements of a PRR-like construct (residues 166-246) demonstrated binding to stathmin-complexed tubulin and taxol-stabilized microtubules with 1:2 stoichiometry [138]. Previous FCS work with engineered protein construct RB3 bound to tubulin with a 1:2 RB3:tubulin stoichiometry [131] and was used to determine the expected diffusion time of 1:2 tau:tubulin interactions. We find that this diffusion time is consistent with prior PRR:tubulin measurements at saturated concentrations of tubulin (10 μM) [141] as well as FCS measurements from this work (Chapter 2). Through HDX-MS we also observe two major binding sites (Chapter 3), and SDS-PAGE of cross-linked PRR:tubulin reactions show a pronounced band consistent with a 1:2 PRR:tubulin complex (Chapter 4). In conjunction, these results highlight that there are likely two main binding sites located within the PRR that constitute consideration in tau:tubulin binding models.

Phosphorylation as a tool for tuning tau:tubulin interactions

Tau is regulated, in part, by the presence or absence of post-translational modifications. Several PTMs have been identified on tau, including phosphorylation, acetylation, and ubiquitination, amongst others [76]. While much work is still required to fully understand the impact these modifications have on tau function, it is phosphorylation and specifically hyperphosphorylation of tau that is found in post-mortem brain tissue associated with various tauopathies [162]. Despite the MTBR forming the core of disease aggregates [80, 81, 161], potential phosphorylation sites linked both to function and disease cluster with high frequency within the PRR [74].

We find that modification of single phosphorylation sites have mild impacts on the binding affinity of PRR to soluble tubulin dimers, however the decrease in binding is magnified as the number of phosphomimic modifications increase in a single construct (Chapter 2). Subsequent experiments comparing our construct containing the most phosphomimics (PRR_{4P}) to that of wild-type PRR (PRR_{WT}) exhibited the same trend: phosphomimic presence also decreases microtubule binding (Chapter 2), and dynamics (Chapter 3) in addition to tubulin binding, despite interacting with tubulin via similar residues (Chapter 4). Collectively, this indicates that the relative strength of the interaction between tau and tubulin can be 'tuned' by the addition or loss of a phosphate modification. Additionally, the phosphorylation status of tau is developmentally regulated, underscoring the importance of phosphorylation in normal tau function throughout development [68, 69]. Phosphorylation patterns and frequencies may be different in the adult brain, corresponding with different requirements for microtubule growth and stability. Speculatively, as we age, the regulatory mechanisms necessary for proper microtubule function are lost, and this leads to a higher propensity for developing tau-associated diseases.

Revisiting tau:tubulin binding models to incorporate the PRR

Several models have been proposed to characterize tau:tubulin binding. The N-terminal projection domain of tau affects the formation of microtubule bundles [223, 224] and has been described as a polyelectrolyte, polymer brush [225]. Alternatively, tau is proposed to modulate microtubule spacing by dimerization of the projection domain and PRR on neighboring microtubules [223]. However, it is likely that these models are dependent on the ionic strength of the solution due to the importance of electrostatics for these models [226].

In the "jaws" model, the PRR, MTBR and C-terminus bind weakly (if at all) to microtubules and binding is enhanced in the presence of two consecutive domains in a single construct [139, 140, 227]. A later study suggested that residues within the P2 and downstream repeats constitute the 'jaws' to target tau to the microtubule lattice [159]. Then, as a refinement to the 'jaws' model, the addition of a heterogeneous, structural component was included. "Fuzzy complexes" is a term used to describe heterogenous structural conformations that are present between two bound proteins [228]. In tau, these fuzzy complexes appear to be a feature of tau:tubulin interactions for the MTBR, in which multiple weak binding sites result in dynamic, heterogeneous tau-tubulin complexes that correlate with microtubule polymerization [131, 141]. In contrast, the PRR appears to form tight, stochiometric complexes with tubulin dimers. Therefore, fuzzy tau:tubulin complexes are likely due to the combined effects of both PRR and the MTBR.

From our results, we propose a model in which the MTBR binds longitudinally along the microtubule crest, while the PRR supplements binding through lateral interactions between tubulin dimers (Figure 6.1). While tau is typically characterized as binding longitudinally on a microtubule there is some evidence to suggest that tau may also stabilize lateral interactions across microtubule

protofilaments since tau can stabilize tubulin sheets [229]. Furthermore, tau binds tightly to Dolastatin-10 tubulin rings [176], which are analogous to the "ram's horn" of protofilaments during microtubule depolymerization [94, 230]. Tau (2N4R) was also found to promote the formation of Dolastatin-10 tubulin ring stacks suggesting that tau can help bind microtubule protofilaments laterally [176]. Given that lateral bonds have been implied to be the weakest part of the microtubule [92, 231], tau, and specifically the PRR, playing a role in stabilizing these interactions may provide an additional mechanism by which tau is able to stabilize microtubules.

It is of note that the tubulin binding sites identified for PRR in this study do not overlap with the binding sites of MTBR such that both regions could be bound simultaneously (Figure 6.1). This also allows for the possibility of conditions where MTBR anchors tau to the microtubule, while PRR plays a role in attracting tubulin dimers or other binding partners to the microtubule lattice. This work highlights that the PRR-tubulin complex is dynamic, driven primarily by interactions between sequences embedded within the PRR and electrostatic attraction between negative tubulin and positive PRR; and the introduction of phosphomimics or phosphorylation, likely diminishes these favorable interactions.

CHAPTER 6: MATERIALS AND METHODS

6.1 PRR Expression and Purification

The proline rich domain (PRR, tau amino acids 149-244) was cloned into a pET-HT vector containing an N-terminal HisX6 tag with a tobacco etch virus (TEV) cleavage site and expressed in BL21(DE3) cells in 0.5 L growths of LB Amp (100 μg/mL) media until reaching absorbance at 600 nm of 0.5-0.6. At this point, expression was induced by the addition of 1 mM IPTG for 4-6 hours at 37 °C. The cells were pelleted and resuspended in 50 mM Tris pH 8.0, 500 mM NaCl, 10 mM imidazole, 1 mM PMSF, and one cOmplete protease inhibitor cocktail tablet. The lysed cells were flash frozen in liquid nitrogen and stored at -80 °C until use. To thawed lysate 1 mg/mL of lysozyme was added prior to sonication. The sonicated lysate was then centrifuged at 20,000xg for 20 minutes at 4 °C to remove cellular debris. The supernatant was syringe filtered through a 0.22 μm filter and incubated with ~5-7 mL of Ni-NTA resin for 1 hour at 4 °C with rotation. The beads were washed with Buffer A (50 mM Tris pH 8.0, 500 mM NaCl, 10 mM imidazole), and PRR eluted in a single step with Buffer B (50 mM Tris pH 8.0, 500 mM NaCl, 400 mM imidazole). The eluate was concentrated and buffer exchanged into Buffer A using Amicon Ultra Ultracel-3K. The protein was then incubated with TEV protease at 4 °C overnight while rocking. The cleaved protein was once again incubated for 1 hour in Ni-NTA beads at 4 °C with rotation. The cleaved PRR was collected in the flow-through, while the cleaved N-terminal HisX6 tag and any remaining uncleaved PRR and the TEV protease all remained associated with the Ni-NTA beads. The PRR was concentrated and buffer exchanged into Buffer C (25 mM Tris pH 8, 100 mM NaCl, 1 mM EDTA, 1 mM TCEP) using Amicon Ultra Ultracel-3K. The sample was filtered as before and

loaded on Superdex 200 HiLoad 16/600 for further purification. Purified protein was flash frozen in liquid nitrogen and stored at -80 °C until use.

6.2 PRR Cloning

Full length tau was cloned into a pET vector which includes an N-terminal HisX6 tag and a TEV cleavage site. This vector was then used to generate a fragment with PRR (149-244) alone via deletion cloning and stop codon insertion as in [141]. Additional constructs were produced using site-directed mutagenesis. For site-specific fluorescent labeling, cysteines were introduced at the fragment termini at amino acid positions 149 and 244, and glutamate mutations to generate phosphomimics at amino acid positions 181, 217, 231, 235. Primers used for cloning are listed in Table 6.1.

6.3 PRR Fluorescent Labeling

For site-specific labeling of PRR, a cysteine (PRR contains no native cysteines) was introduced at the N-terminus, residue 149. Expression and purification of this construct was as described above. For labeling, ~300 μM PRR (determined by UV-Vis with ε_{280} = 1,490 $M^{-1}cm^{-1}$) was treated with 1 mM DTT and incubated at room temperature for 30 mins to reduce the cysteine. The protein was buffer exchanged as described previously with Amicon concentrators into labeling buffer (20 mM Tris pH 7.4, 50 mM NaCl) with 6M Guanidine HCl. For labeling, Alexa Fluor 488 maleimide (AL488) was added in 3-5X molar excess to protein and incubated overnight with stirring at 4 °C Prior to its use in the labeling reaction, AL488 was dissolved in anhydrous DMSO, aliquoted and flash frozen in liquid nitrogen for storage at -80 °C. For labeling, a single aliquot was quickly thawed prior to a labeling reaction, with any unused dye discarded. Any remaining

Mutation	Primer Direction	Primer
T181E	Forward	5' - CCG CCC GCT CCA AAG GAA CCA - 3'
T181E	Reverse	5' - ACC AGA GCT GGG TGG TTC CTT - 3'
T217E	Forward	5' - ACC CCG TCC CTT CCA GAA CCA - 3'
T217E	Reverse	5' - CTC CCG GGT GGG TGG TTC TGG AA - 3'
T231E	Forward	5' - AAG GTG GCA GTG GTC CGT GAA CCA - 3'
T231E	Reverse	5' - ACG GCG ACT TGG GTG GTT CAC GGA - 3'
S235E	Forward	5' - CCA CCC AAG GAG CCG TCT TCC - 3'
S235E	Reverse	5' - CTT GGC GGA AGA CGG CTC CTT - 3'
Q244C	Forward	5' - CGC CAA GAG CCG CCT GTG TTA AG - 3'
Q244C	Reverse	5' - GCT TGA ATT CTT AAC ACA GGC GGC TC - 3'

Table 6.1 Primers used for site-directed mutagenesis of PRR.

unconjugated dye and Guanidine HCl are removed by buffer exchange into labeling buffer with Amicon concentrators, followed by passing the sample through two coupled 5 mL HiTrap desalting columns. Labeled proteins were aliquoted, flash frozen in liquid nitrogen, and stored at -80 °C until use.

6.4 Tubulin Purification

Tubulin was purified as previously described [232] from young bovine brains with two cycles of polymerization and depolymerization with one modification: the concentration of nucleosides was adjusted to 1.5 mM ATP and 1 mM GTP for the first polymerization, then increased to 2.5 mM ATP and 1.5 mM GTP for the second polymerization step. The resulting tubulin was flash frozen in liquid nitrogen in BRB80 (80 mM PIPES, 1 mM $MgCl_2$, 1 mM EGTA, pH 6.8) and stored at -80 °C. As needed, aliquots were thawed quickly at room temperature, then clarified via centrifugation at 100,000xg for 6 min at 4 °C. BioSpin 6 columns (BioRad) were used to exchange tubulin into the desired buffer. The tubulin concentration was determined by using the absorbance at 280 nm and molar extinction coefficient of 115,000 $M^{-1}cm^{-1}$, and used within 2 hours of clarification.

6.5 Fluorescent Labeling of Tubulin

The tubulin labeling protocol was adapted from a previously published protocol [233]. To 200 µL tubulin (5-10 mg/mL), 22 µL 5X BRB80, 1.6 µL 500 mM $MgCl_2$ and 2.24 µL 100 mM GTP were added, and the solution was incubated on ice for 5 minutes. To this solution, 100 µL 37 °C glycerol was added and mixed well by pipetting. The solution was incubated in a 37 °C water bath for 30 minutes to polymerize tubulin. The tubulin mixture was layered onto 200 µL 37 °C

high pH cushion (0.1 M HEPES, pH 8.6, 1 mM $MgCl_2$,1mM EGTA, 60% v/v glycerol). The microtubules were pelleted by centrifugation at 192,000xg for 45 minutes at 35 °C. The supernatant was removed by pipette aspiration and discarded, followed by gentle rinsing of the supernatant-cushion interface twice with labeling buffer (0.1 M HEPES, pH 8.6, 1 mM $MgCl_2$,1mM EGTA, 40% v/v glycerol). All liquid, including the cushion, was removed by pipette aspiration. The tube was returned to the 37 °C water bath and 120 µL labeling buffer, also at 37 °C, was added. The pellet was resuspended by pipetting, using a pipette tip with the end cut off to avoid shearing the microtubules.

Assuming ~70% recovery of initial tubulin, Rhodamine Red-X succinimidyl ester (from a 13 mM stock in anhydrous DMSO) was added to 10-fold molar excess to the 120 µL microtubule solution. The microtubule-dye solution was incubated for 30-40 minutes in a 37 °C water bath, with vortexing for 5 seconds every 2 minutes. 120 µL quench buffer (2X BRB80, 100 mM K-glutamate, 40% v/v glycerol) was added and mixed well by pipetting. The solution was incubated in a 37 °C water bath for 15 minutes, the pipetted onto 180 µL low pH cushion (1X BRB80 pH 6.9, 60% v/v glycerol). The solution was centrifuged at 300,000xg for 20 minutes at 37 °C. Following centrifugation, the rotor was moved to 4°C and the ultracentrifuge temperature was set to 2 °C.

The supernatant was removed by pipette aspiration and discarded. The supernatant-cushion interface was washed twice with warm BRB80 and discarded. All remaining liquid, including the cushion, was removed by pipetting and 60 µL ice cold BRB80 was added to the pellet. The pellet was resuspended by pipetting, using a pipette tip with the end cut off. Pipetting was continued until no chunks were visible. The solution was incubated on ice for at least 60 minutes, then centrifuged

at 300,000xg for 10 minutes at 2 °C. The supernatant was recovered, and the final tubulin concentration and labeling stoichiometry were determined by absorbance.

6.6 FCS Instrumentation and Analysis

All FCS measurements were performed on our home-built instrument as described previously [157]. The laser (488 nm diode-pumped solid-state laser, Spectra-Physics) was adjusted to ~5 μW prior to entering the inverted Olympus 1X-71 Microscope (Olympus) and focused using a 60x 1.2 NA water immersion objective. Fluorescence emission was collected through the objective and separated from excitation light by a Z488RDC long pass dichroic and a 500LP long pass filter (Chroma). Collected emission was focused onto the aperture of a 50 μm diameter optical fiber (OzOptics) directly coupled to an avalanche photodiode (Perkin-Elmer). A digital correlator (FLEX03LQ-12, Correlator.com) was used to calculate the autocorrelation curves. Alignment of instrument and analysis were verified using Alexa Fluor 488 hydrazine (Fisher).

Measurements were made in 8-chamber coverslips (Nunc, Lab-Tek) passivated by incubation with PEG-PLL to reduce protein adsorption [158]. For each measurement, ~15-25 nM labeled PRR was incubated with tubulin (a range of concentrations was used) for 5 min in Nunc chambers in phosphate buffer (20 mM phosphate buffer pH 7.4, 20 mM KCl, 1 mM MgCl2, 0.5 mM EGTA, and 1 mM DTT) at 20 °C. Each measurement consisted of 25 traces of 10 seconds. The autocorrelation curves were averaged and fit to a one-component (Eqn 1: PRR alone) or a two-component (Eqn2: PRR + tubulin) 3D diffusion equation using lab-written scripts in MATLAB (Mathworks). These measurements were run in triplicate on different days and averaged to obtain statistical variations.

Eqn 1: $G(\tau) = \frac{1}{N}\left[1 + \frac{\tau}{\tau_{un}}\right]^{-1}\left[1 + \frac{\tau}{\omega^2\tau_{un}}\right]^{-\frac{1}{2}}$

Eqn 2: $G(\tau) = \frac{1}{N}\left(f \times \left[1 + \frac{\tau}{\tau_{un}}\right]^{-1}\left[1 + \frac{\tau}{\omega^2\tau_{un}}\right]^{-\frac{1}{2}} + (1-f) \times \left[1 + \frac{\tau}{\tau_b}\right]^{-1}\left[1 + \frac{\tau}{\omega^2\tau_b}\right]^{-\frac{1}{2}}\right)$

G(τ) is the autocorrelation function as a function of time, where τ_{un} and τ_b are the diffusion times of free PRR_{WT} and PRR_{WT} with 10 μM tubulin, respectively; N is the average number of fluorescent species in the focal volume; f is the fraction of free PRR; and s is the ratio of the radial to axial dimensions of the focal volume. For our instrument, s was determined using Alexa 488 hydrazine (Invitrogen) as a reference standard to be 0.2 and subsequently fixed for all fitting. We note that the apparent decrease in the fraction bound plateau for PRR_{2P} and PRR_{4P} likely reflects dynamic exchange of tubulin in the PRR-tubulin complex as it diffuses through the observation volume, resulting in a decrease in the apparent τ_b of those constructs. We thus chose to use the τ_b of PRR_{WT} at 10 μM tubulin for fitting of all FCS curves to underscore differences in binding by the phosphomimics.

Binding curves were constructed by plotting the fraction bound, f_b=(1-f) from the FCS fits as a function of tubulin, which were then fit to the Hill equation (Eqn 3).

Eqn 3: $f_b = y^{max}\frac{[tubulin]^n}{K_D + [tubulin]^n}$

The curves were fit with the Hill coefficient (n) as a global parameter, y^{max} fixed to the maximum value of f_b for each construct, and the apparent dissociation constants (K_D) as individual parameters.

6.7 FRET Instrumentation and Analysis

All FRET measurements were performed on a MicroTime 200 inverse time-resolved confocal microscope (Picoquant) in pulsed interleaved excitation FRET (PIE-FRET) mode as described previously [234]. The laser power was adjusted to ~30 μW for both 485 nm and 561 nm diode-pumped solid-state lasers and operated at 40 MHz pulse rate before reaching the objective. Fluorescence emission was collected through the objective and passed through a 150 μm diameter pinhole. The emission was separated from excitation light by a 405/488/561/635 nm quad-edge laser dichroic beamsplitter (AVR Optics), and ET525/50M and HQ600LP filters coupled to avalanche photodiodes for detection. Alignment of instrument and analysis were verified using 10 base pair, 14 base pair and 18 base pair double stranded DNA standards labeled with Alexa Fluor 488 and Alexa Fluor 594 maleimide (Integrated DNA Technologies).

Measurements were made in 8-chamber Nunc coverslips (Thermo-Fisher) passivated by incubation with PEG-PLL to reduce protein adsorption. ~30 pM of labelled PRR was incubated with listed tubulin concentrations for 5 min in Nunc chambers prior to each measurement in phosphate buffer (40 mM potassium phosphate pH 7.4, 50 mM KCl) at 20 °C unless otherwise indicated. Each photon trace was collected in 1ms time bins for one hour and a cutoff of 25 photons per PIE FRET event was used to determine fluorescent protein events over background noise. ET_{eff} and stoichiometry factors were calculated using SymphoTime 64 software and these histograms

were fit using Gaussian distributions to determine the peak ETeff values. These measurements were run in triplicate on different days and averaged to obtain statistical variations.

Eqn 4: $$ET_{eff} = \frac{I_a - \beta I_d}{(I_a - \beta I_d) + \gamma(I_d - \beta I_d)}$$

ET_{eff} is the energy transfer efficiency where the fluorescence intensity of the acceptor and donor channels are I_a and I_d, respectively. Whereas β is the bleed through of the donor channel into the acceptor channel. For our instrument, the difference in the total quantum efficiency of the system and fluorophores (γ) was determined to be 1.08 using Alexa Fluor 488 and Alexa Fluor 594 hydrazine (Invitrogen) as reference standards and subsequently fixed.

6.8 Microtubule Polymerization Assay

Polymerization of soluble tubulin into microtubules was monitored through the increase of scattered light at 340 nm as described previously [141]. Tubulin aliquots were clarified via centrifugation and buffer exchanged into phosphate buffer (20 mM phosphate buffer pH 7.4, 20 mM KCl, 1 mM $MgCl_2$, 0.5 mM EGTA, and 1 mM DTT). For each reaction 10 μM tubulin was incubated with 10 μM PRR for 2.5 minutes on ice. After the addition of 1 mM GTP, the reaction was immediately transferred to a cuvette and measured for 10 min at 37 °C in a fluorometer (FP-8300 with temperature accessory ETC-815, JASCO) with excitation and emission at 340 nm. Thereafter, the samples were returned at 4 °C for 5 min to establish the absence of protein aggregation with cold depolymerization. These measurements were run in triplicate and averaged to obtain statistical variations. Polymerization curves were fit to a sigmoidal equation (Eqn 5).

Eqn 5: $$y = y^{min} + \frac{y^{max} - y^{min}}{1 + \left(\frac{T_{50}}{T}\right)^{m}}$$

In which y^{min} and y^{max} are the minimum and maximum values for the signal of light at 340 nm over time (T) in seconds to obtain half-times (T_{50}). The slope (m) is the light scattering of $y^{max} - y^{min}$.

6.9 Preparation of Taxol-Stabilized Microtubules

Taxol stabilized microtubules were made following a previously published protocol, with minor adaptions [235]. All tubulin solutions were thawed on ice. Tubulin (38 µM), Rhodamine Red-X tubulin (1 µM) and biotin tubulin (1 µM) were added to final volume of 20 µL in BRB80. The solution was pipetted to mix and then clarified by centrifugation at 100,000xg for 6 minutes at 4 °C. Following centrifugation, the rotor was moved to 37 °C and the ultracentrifuge temperature was set to 37 °C.

The supernatant was removed to a new ultracentrifuge tube and 1 µL GTP (from a 20 mM stock in water) was added. The solution was incubated in a 37 °C water bath for 20 minutes to polymerize tubulin. Following incubation, 50 µM taxol in BRB80 was added in 2 µL increments for a total of 8 µL. Following each incremental taxol addition, the tube was flicked several times to mix. The solution was incubated in a 37 °C water bath for 15 minutes to polymerize the tubulin. The microtubules were pelleted by centrifugation at 353,000xg for 5 minutes at 37 °C. Following centrifugation, the supernatant was removed and discarded, and the pellet was resuspended in 10 µL of 20 µM taxol in BRB80.

6.10 Preparation of Sample Chambers for TIRF Imaging

Coverslips and glass slides were cleaned according to a previously published protocol [236]. Briefly, coverslips and glass slides were wiped with Kimwipes then placed in a holding chamber filled with 100% acetone and sonicated at room temperature for 15 minutes. The acetone was discarded, the coverslips and glass slides rinsed with ultrapure water before being sonicated in ultrapure water for 15 minutes. The water was discarded and replaced with 95% ethanol and sonicated for 15 minutes. The coverslips and glass slides were then placed directly in containers containing fresh 95% ethanol where they were stored until use.

A clean coverslip stored in ethanol was air dried and then plasma cleaned for 5 minutes on the highest setting. The coverslip was placed into a coplin jar with a sufficient volume of RainX (polysiloxane blend in ethanol, isopropanol, and water) to completely submerge it. After 1 minute incubation, the coverslip was removed, thoroughly dried with lens wipes and then returned to the coplin jar for an additional minute. The coverslip was then thoroughly dried and cleaned with lens wipes once more. A clean glass slide stored in ethanol was flame dried. Upon cooling, a chamber of approximately 5 µL capacity were created using strips of double-sided tape. The coverslip was then placed clean side down onto the tape and secured.

To functionalize the surface, a 1% neutravidin solution in phosphate buffered saline was added into the chamber and incubated for 10 minutes. The chamber was rinsed with 10 volumes of phosphate buffer (20 mM phosphate buffer pH 7.4, 20 mM KCl, 1 mM $MgCl_2$, 0.5 mM EGTA, and 1 mM DTT). Two volumes of a 5% Pluronic F-127 solution in phosphate buffer were added to the chamber and incubated for 10 minutes. The chambers were rinsed with 10 volumes of phosphate buffer and left filled with buffer until ready for use.

6.11 Imaging of PRR-Microtubules by TIRF

Taxol stabilized microtubules (described above) were diluted 1:400 in phosphate buffer supplemented with 20 µM taxol. PRR_{WT} or PRR_{4P} labeled with Alexa 488 was added to a final 1:4 molar ratio with the microtubules (in tubulin concentration units). The microtubule/PRR solutions were incubated for 10 minutes and then loaded into sample chambers. The chambers were sealed with CoverGrip to prevent evaporation prior to imaging.

Imaging of PRR/microtubules by TIRF microscopy was conducted at ambient temperature on an inverted Eclipse Ti2 microscope (Nikon) with 100x Apo TIRF objective lens (1.49 NA) and sCMOS camera, running NIS Elements version 5.11.01. The PRR was imaged by excitation with a 488nm laser (green channel) while the microtubules were excited with a 561 nm laser (red channel). All images were obtained with a 1 s exposure. For each laser, the same illumination power was used for all images to allow for comparison.

TIRF microscopy images were analyzed using FIJI (ImageJ; National Institutes of Health). Overlapping areas of uniform illumination within the red and green channels were determined and only microtubules within this area were analyzed. Microtubules were randomly selected from the red channel images; selected microtubules were copied directly into the corresponding green channel image using the ROI Manager feature to select for microtubule bound PRR. For each microtubule, the length and average brightness was calculated in both the green and red channels. For the analysis, 131 (PRR_{WT}) or 116 (PRR_{4P}) microtubules from 10 different images were analyzed.

6.12 Prolyl Endopeptidase Purification

Aspergillus niger Prolyl endopeptidase (AnPEP) was purified from dietary supplement (GliadinX) by dissolving one capsule in 2 mL of Buffer D (100 mM phosphate pH 4, 100 mM

NaCl). The mixture was syringe filtered through a 0.22 μm filter then 1 mL of the solution was run on a Superdex 200 HiLoad 16/600 size exclusion column. Fractions containing AnPEP were pooled, concentrated and buffer exchanged into Buffer E (100 mM phosphate pH 8, 20 mM NaCl) using Amicon Ultra Ultracel-30K. The sample was filtered as before and loaded on a 5 mL HiTrap Q HP. For separation, a 10-70% Buffer F (100 mM phosphate pH 8, 1 M NaCl) gradient was applied over 25 column volumes. AnPEP eluted at approximately 300 mM salt. This was repeated with the second 1 mL of the filtered enzyme solution before ultimately pooling relevant fractions post anion exchange. Purified AnPEP was buffer exchanged into Buffer D and stored at 4 °C overnight prior to coupling to column resin. The AnPEP concentration was determined by using the absorbance at 280 nm, molar extinction coefficient of 125,305 $M^{-1}cm^{-1}$, with molecular weight of 72.1 kDa and final yield of ~50 mg per capsule.

6.13 Prolyl Endopeptidase Coupling

AnPEP was coupled to POROS-20AL (Fisher) resin by forming covalent bonds between primary protein amines and the reactive aldehyde groups on the column resin. To prepare the column, 0.2 g of POROS-20AL resin was added to 100 mg of AnPEP in 1 mL of Buffer D (100 mM phosphate pH 4, 100 mM NaCl). 320 μL of Buffer H (100 mM sodium citrate pH 4.4, 1.5 M sodium sulphate) and 100 μL of Buffer K (1 M sodium cyanoborohydride) were added slowly. Then, a total of 660 μL of Buffer H was added over a 2 hr period (27.5 μL every 5 min), with the solution placed on a rocker at room temperature between additions. The mixture was incubated overnight at room temperature with continuous rocking. The reaction was quenched with 150 μL of Buffer I (100 mM sodium citrate pH 4.4, 0.1 M ethanolamine, 5 mM sodium cyanoborohydride) and then placed back on the rocker for 1 hr at room temperature. Using a sintered glass funnel the

resin was washed with 12 mL of Buffer G (100 mM sodium citrate pH 4.4), 10 mL Buffer J (100 mM sodium citrate pH 4.4, 1 M NaCl), then 12 mL of Buffer G. The resin was resuspended in a 50:50 solution (v/v) of resin:Buffer G and immediately used to prepare a column for HDX-MS. Any remaining resin was stored at 4 °C until use.

6.14 HDX-MS Peptide List Preparation

For initial peptide list generation 10 µM PRR_{WT} (or PRR_{4P}) in phosphate buffer (100 mM NaPO4, 150 mM NaCl, pH 7.45) was injected on to a home-built system for combined protease degradation and subsequent LC-MS^2 identification of peptide fragments(Kan et al., 2019)1. Briefly, the injected sample passed through two columns packed with protease-loaded resin (as described above; proteases used are pepsin and AnPEP) for 4 min at 0 ^{0}C. The resulting peptides were desalted on a C8 trap column. After desalting, peptides were eluted through an analytical C8 column and introduced to a Thermo Q Exactive ESI-MS. The elution profile of the analytical separation was a H_2O/ACN gradient of 5%-40% over 15 mins. LC-MS^2 data was analyzed with Proteome Discover (v. 2.4 Thermo-Fisher) to detect and identify peptide fragments based on the initial sequence of the PRR constructs. The initial list was then used to generate reported peptide coverage maps were generated using EXMS2 analysis software [237, 238].

6.15 HDX-MS Sample Preparation Data Acquisition

For each exchange reaction concentrated PRR was diluted 4x in deuterated exchange buffer (100 mM NaPO4, 150 mM NaCl, pD 7.45) and allowed to exchange at RT for 30s. The reaction was quenched at 0 °C via 2x dilution in deuterated quench buffer (100 mM NaPO4, 150 mM NaCl, 2M Guanidine HCl, pD = 2.5l). The final concentration of PRR in all HDX reactions was 10 µM.

"All-H" control samples were prepared in the same manner, but standard protonated formulations of the above exchange and deuterated buffers were used. Samples HDX were analyzed in the same manner as those used for peptide list generation except MS^1 spectrometry was conducted to detect to the total mass difference in each detected peptide. For measurements in the presence of tubulin, PRR_{WT} (or PRR_{4P}) was combined in a 2:1 (tubulin:PRR) molar ratio in phosphate buffer (100 mM $NaPO_4$, 150 mM NaCl, pH = 7.45) and incubated for 3 min at room temperature. The mixture was then diluted 4x in deuterated exchange buffer and analyzed in the same manner as PRR-only samples.

6.16 HDX-MS Data Analysis

Deuterated peptides from each HDX-MS sample were detected and analyzed using EXMS2 software as previously published [237]. Briefly, each HDX-MS sample was compared to the "All-H" protonated to determine the retention time of each peptide generated from the protease digest. Changes in m/z ratio of each peptide are interpreted as incorporation of deuterons. Peptide maps showing comparative deuteration were generated using python (v 3.11), pandas (2.1.2), and matplotlib (v 3.8.0). Percent deuteration was determined was determined by comparing the observed mass change to the maximum possible deuteration sites. Coloration on peptide maps were normalized according to this percentage.

6.17 Cross-linking Sample Preparation

50 μg of purified tau and 50 μg of purified tubulin were mixed with 6 mM DSBU (Thermo) in phosphate buffer (20 mM phosphate buffer pH 7.4, 20 mM KCl, 1 mM MgCl2, 0.5 mM EGTA, and 1 mM DTT) and incubated on ice for 1 hour. The reaction was quenched by adding 50 mM

ammonium bicarbonate then incubated on ice for 30 min. The cross-linked material was separated by SDS-PAGE and gel bands were cut into ca. 1 mm^3 pieces. The gel pieces were destained in 30% (v/v) ethanol at 60 °C for 30 min, dehydrated with 100% acetonitrile at room temperature for 1 hour, and dried in a laminar flow hood overnight. Gel pieces were stored at −20°C for analysis by MS.

6.18 Cross-linking Sample Preparation for Mass Spectrometry

Gel pieces were rehydrated and dehydrated a few more times with 25mM Ammonium Bicarbonate (AB) and Acetonitrile (ACN;) respectively. Gel pieces were incubated with 500ul of 25mM AB with final 20ng/ul of trypsin (Thermo Fisher Scientific) at room temperature overnight. Digested peptides were recovered by incubating gel pieces with 400ul of 60% ACN, 0.1% 0.1% (v/v) trifluoroacetic acid (TFA; Thermo Fisher Scientific) for 10 min in the shaker (3x). The peptides were then evaporated to dryness and resuspended with 0.1% (v/v) trifluoroacetic acid (TFA; Thermo Fisher Scientific) to fractionate peptides with PierceTM High pH Reversed-Phase Peptide Fractionation Kit (Thermo Fisher Scientific) according to the recommended protocol by the supplier. All fractions were vacuum-dried and resuspended with LC-MS grade water containing 0.1% (v/v) TFA for MS analysis.

Each fraction was analyzed by a Q-Exactive HF mass spectrometer (Thermo Fisher Scientific) coupled to a Dionex Ultimate 3000 UHPLC system (Thermo Fisher Scientific) equipped with an in-house–made 15-cm-long fused silica capillary column (75 μm inner diameter), packed with a reversed-phase ReproSil-Pur C18-AQ 2.4-μm resin (Dr. Maisch GmbH, Ammerbuch, Germany) column. Elution was performed using a gradient from 5 to 45 % B (90 min), followed by 90 % B (5 min), and re-equilibration from 90 to 5 % B (5 min) with a flow rate

of 3-400 nL/min (mobile phase A: water with 0.1 % formic acid; mobile phase B: 80 % acetonitrile with 0.1 % formic acid). Data were acquired in data-dependent tandem MS (MS/MS) mode. Full-scan MS settings were as follows: mass range, 300 to 1800 (mass/charge ratio); resolution, 120,000; MS1 AGC target 1^{E6}; MS1 Maximum IT, 200 ms. MS/MS settings were as follows: resolution, 30,000; AGC target 2^{E5}; MS2 Maximum IT, 300 ms; fragmentation was enforced by higher-energy collisional dissociation with stepped collision energy of 25, 27, 30; loop count, top 12; isolation window, 1.5 m/z; fixed first mass, 130; MS2 Minimum AGC target, 800; charge exclusion: unassigned, 1, 2, 3, 8 and > 8; peptide match, off; exclude isotope, on; dynamic exclusion, 45 s [239].

6.19 Cross-linked Peptide Search

Raw files were converted to mzML format with ThermoRawFileParser 1.2.3[240]. Search engine MeroX 2.0.1.4 [207] was used to identify and validate cross-linked peptides. Fasta file was generated manually with proteins of interest entries with Uniprot *Escherichia coli* (strain B / BL21-DE3) proteome and EBI Reference proteome of *Bos taurus* (Uniprot Release 2021_03). MeroX was run in RISEUP mode, with default crosslinker mass and fragmentation parameters for DSBU with minor tweaks: precursor mass range, 1000 to 10,000 Da; minimum precursor charge, 4; precursor and fragment ion precisions, 5.0 and 10.0 ppm, respectively; maximum number of missed cleavages, 3; oxidation of methionine, as variable modification; results were filtered for score (>10) and target-decoy approach FDR (<1 %). All search results from each fraction's MS acquisition were combined and filtered by recalculated FDR at 1 %. K-K residue pairs were selected for the site-localization when crosslinked peptides contained miscleaved lysine residues

and site localization scores were tie. Visualization of the crosslinks were performed with xiView[212] and ChimeraX 1.5[213].

APPENDIX: SMALL MOLECULES DEM AND RO INHIBIT ALPHA-SYNUCLEIN OLIGOMERS BUT NOT MONOMER PROTEIN

This appendix chapter is adapted from Anthony R Braun, Elly E Liao, Mian Horvath, Prakriti Kalra, **Karen Acosta**, Malaney C Young, Noah Nathan Kochen, Chih Hung Lo, Roland Brown, Michael D Evans, William C K Pomerantz, Elizabeth Rhoades, Kelvin Luk, Razvan L Cornea, David D Thomas, Jonathan N Sachs (2021). Potent inhibitors of toxic alpha-synuclein identified via cellular time-resolved FRET biosensors. *npj Parkinson's Disease*. 7, 52. doi: 10.1038/s41531-021-00195-6

I prepared the recombinant, fluorescently labeled alpha-synuclein and collected the single-molecule FRET data shown below as Figure A.1 and Table A.1.

A.1 Summary

To detect pre-fibrillar oligomers in living cells, the Sachs lab has developed a high-throughput drug discovery platform based on measuring the fluorescence resonance energy transfer of fluorescent alpha-synuclein biosensors. Both inter-protomeric and intra-protomeric FRET biosensors were transiently transfected into HEK293 cells to investigate alpha-synuclein oligomerization and conformation. High-throughput screening of a 1280-compound Library of Pharmacologically Active Compounds validated screening before testing the efficacy of these hits in SH-SY5Y cells overexpressing unlabeled alpha-synuclein to eliminate labeling artifacts. Ultimately two small molecules Demeclocycline HCl (DEM) and Ro 90–7501 (RO) were found to protect SH-SY5Y cells from alpha-synuclein induced death with nanomolar potency. Additional lead compounds, like (±)-Bay K 8644 (Bay) were also examined, but Bay was not found to be effective in SH-SY5Y models. In addition to other biochemical and biophysical assays, *in vitro* single-molecule FRET measurements highlighted here demonstrate that these compounds modulate alpha-synuclein oligomers but not monomers.

A.2 Results

Intra-protomeric biosensors were unable to distinguish between conformational changes in monomer or oligomeric alpha-synuclein. Thus, it is possible that the alpha-synuclein biosensor FRET response of hit compounds RO, Bay, and DEM may act on alpha-synuclein by altering protein conformation. Thus, to investigate the mechanism of action for these small molecules on monomeric alpha-synuclein we used single-molecule FRET. Alpha-synuclein constructs were fluorescently labeled with Alexa Fluor 488 (donor) or Alexa Fluor 594 (acceptor) maleimide either at residues 9 and 72 (αS 9-72) or residues 54 and 130 (αS 54-130) to examine the N-terminus and C-terminus of alpha-synuclein, respectively. Neither Bay or DEM showed significant changes in energy transfer efficiencies nor histograms for either alpha-synuclein constructs suggesting that these compounds do not modulate monomer conformation (Figure A.1). We were unable to evaluate RO with smFRET, due to interactions of RO with the AlexaFluor-594 maleimide. However, taken in conjunction with protein-observed fluorine (PrOF) nuclear magnetic resonance (NMR) (not shown here) it is likely that these small molecules operate using a mechanism of action that does not include the direct binding or interaction with alpha-synuclein.

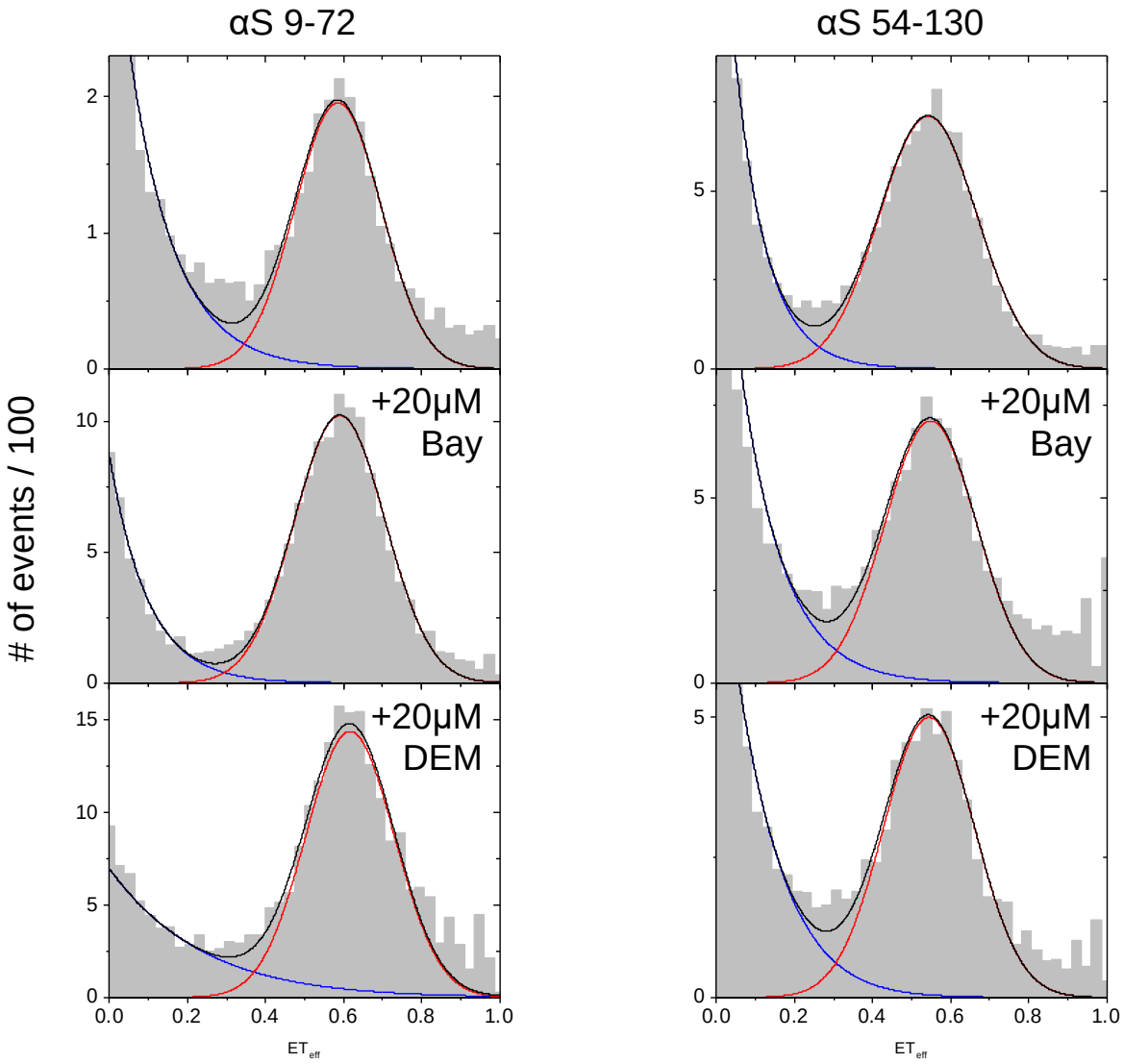

Figure A.1 Hit compounds Bay and DEM do not interact with monomeric alpha-synuclein. Representative histograms from smFRET measurements in the presence and absence of Bay and DEM. αS labeled at residues 9 and 72 (*left*) or at residues 54 and 130 (*right*). FRET measurements of αS with Ro are not shown due to interactions between Ro and acceptor dye, Alexa Fluor 594 maleimide.

Labeling Positions	ET_{eff} (buffer)	ET_{eff} (+Bay)	ET_{eff} (+DEM)
9C-72C	0.54 ± 0.009	0.54 ± 0.013	0.55 ± 0.005
54C-130C	0.59 ± 0.013	0.58 ± 0.005	0.60 ± 0.008

Table A.1 Energy transfer efficiencies (ET_{eff}) of alpha-synuclein constructs with Bay and DEM. ETeff values for αS labeled at residues 9 and 72 or at residues 54 and 130 in the presence and absence of Bay and DEM. Values tabulated are mean ± standard deviation for a minimum of three measurements.

BIBLIOGRAPHY

1. Fischer, E., *Einfluss der Configuration auf die Wirkung der Enzyme.* Berichte der deutschen chemischen Gesellschaft, 1894. **27**(3): p. 2985-2993.
2. Uversky, V.N., *Intrinsically disordered proteins and their (disordered) proteomes in neurodegenerative disorders.* Front Aging Neurosci, 2015. **7**: p. 18.
3. Sigler, P.B., *Transcriptional activation. Acid blobs and negative noodles.* Nature, 1988. **333**(6170): p. 210-2.
4. Kriwacki, R.W., et al., *Structural studies of p21Waf1/Cip1/Sdi1 in the free and Cdk2-bound state: conformational disorder mediates binding diversity.* Proc Natl Acad Sci U S A, 1996. **93**(21): p. 11504-9.
5. Uversky, V.N., *Intrinsically Disordered Proteins and Their "Mysterious" (Meta)Physics.* Frontiers in Physics, 2019. **7**.
6. Xue, B., A.K. Dunker, and V.N. Uversky, *Orderly order in protein intrinsic disorder distribution: disorder in 3500 proteomes from viruses and the three domains of life.* J Biomol Struct Dyn, 2012. **30**(2): p. 137-49.
7. Kulkarni, P. and V.N. Uversky, *Intrinsically Disordered Proteins: The Dark Horse of the Dark Proteome.* Proteomics, 2018. **18**(21-22): p. e1800061.
8. Darling, A.L. and V.N. Uversky, *Intrinsic Disorder in Proteins with Pathogenic Repeat Expansions.* Molecules, 2017. **22**(12).
9. Jorda, J., et al., *Protein tandem repeats - the more perfect, the less structured.* FEBS J, 2010. **277**(12): p. 2673-82.
10. Uversky, V.N., *Unusual biophysics of intrinsically disordered proteins.* Biochim Biophys Acta, 2013. **1834**(5): p. 932-51.
11. Oldfield, C.J., et al., *Flexible nets: disorder and induced fit in the associations of p53 and 14-3-3 with their partners.* BMC Genomics, 2008. **9 Suppl 1**(Suppl 1): p. S1.
12. Wright, P.E. and H.J. Dyson, *Intrinsically disordered proteins in cellular signalling and regulation.* Nat Rev Mol Cell Biol, 2015. **16**(1): p. 18-29.
13. Peng, Z., et al., *A creature with a hundred waggly tails: intrinsically disordered proteins in the ribosome.* Cell Mol Life Sci, 2014. **71**(8): p. 1477-504.
14. Fung, H.Y.J., M. Birol, and E. Rhoades, *IDPs in macromolecular complexes: the roles of multivalent interactions in diverse assemblies.* Curr Opin Struct Biol, 2018. **49**: p. 36-43.
15. Murata, K. and M. Wolf, *Cryo-electron microscopy for structural analysis of dynamic biological macromolecules.* Biochim Biophys Acta Gen Subj, 2018. **1862**(2): p. 324-334.
16. Jensen, M.R., R.W. Ruigrok, and M. Blackledge, *Describing intrinsically disordered proteins at atomic resolution by NMR.* Curr Opin Struct Biol, 2013. **23**(3): p. 426-35.
17. Chowdhury, A., D. Nettels, and B. Schuler, *Interaction Dynamics of Intrinsically Disordered Proteins from Single-Molecule Spectroscopy.* Annu Rev Biophys, 2023. **52**: p. 433-462.
18. Liu, X.R., M.M. Zhang, and M.L. Gross, *Mass Spectrometry-Based Protein Footprinting for Higher-Order Structure Analysis: Fundamentals and Applications.* Chem Rev, 2020. **120**(10): p. 4355-4454.
19. Beveridge, R. and A.N. Calabrese, *Structural Proteomics Methods to Interrogate the Conformations and Dynamics of Intrinsically Disordered Proteins.* Front Chem, 2021. **9**: p. 603639.

20. Weingarten, M.D., et al., *A protein factor essential for microtubule assembly.* Proc Natl Acad Sci U S A, 1975. **72**(5): p. 1858-62.
21. Shea, T.B. and C.M. Cressman, *The order of exposure of tau to signal transduction kinases alters the generation of "AD-like" phosphoepitopes.* Cell Mol Neurobiol, 1999. **19**(2): p. 223-33.
22. Nunez, J. and I. Fischer, *Microtubule-associated proteins (MAPs) in the peripheral nervous system during development and regeneration.* J Mol Neurosci, 1997. **8**(3): p. 207-22.
23. Wang, Y., et al., *A novel tau transcript in cultured human neuroblastoma cells expressing nuclear tau.* J Cell Biol, 1993. **121**(2): p. 257-67.
24. Cross, D.C., et al., *Nuclear and cytoplasmic tau proteins from human nonneuronal cells share common structural and functional features with brain tau.* J Cell Biochem, 2000. **78**(2): p. 305-17.
25. Luo, M.H., et al., *Novel isoforms of tau that lack the microtubule-binding domain.* J Neurochem, 2004. **90**(2): p. 340-51.
26. Liu, C. and J. Gotz, *Profiling murine tau with 0N, 1N and 2N isoform-specific antibodies in brain and peripheral organs reveals distinct subcellular localization, with the 1N isoform being enriched in the nucleus.* PLoS One, 2013. **8**(12): p. e84849.
27. Holehouse, A.S., et al., *CIDER: Resources to Analyze Sequence-Ensemble Relationships of Intrinsically Disordered Proteins.* Biophys J, 2017. **112**(1): p. 16-21.
28. Li, P., et al., *Liquid - liquid phase separation of tau: Driving forces, regulation, and biological implications.* Neurobiol Dis, 2023. **183**: p. 106167.
29. Li, X., et al., *Predicting Protein Disorder for N-, C-, and Internal Regions.* Genome Inform Ser Workshop Genome Inform, 1999. **10**: p. 30-40.
30. Romero, Obradovic, and K. Dunker, *Sequence Data Analysis for Long Disordered Regions Prediction in the Calcineurin Family.* Genome Inform Ser Workshop Genome Inform, 1997. **8**: p. 110-124.
31. Dosztanyi, Z., *Prediction of protein disorder based on IUPred.* Protein Sci, 2018. **27**(1): p. 331-340.
32. Chen, Y., et al., *14-3-3/Tau Interaction and Tau Amyloidogenesis.* J Mol Neurosci, 2019. **68**(4): p. 620-630.
33. Schweers, O., et al., *Structural studies of tau protein and Alzheimer paired helical filaments show no evidence for beta-structure.* Journal of Biological Chemistry, 1994. **269**(39): p. 24290-24297.
34. Schwalbe, M., et al., *Predictive atomic resolution descriptions of intrinsically disordered hTau40 and alpha-synuclein in solution from NMR and small angle scattering.* Structure, 2014. **22**(2): p. 238-49.
35. Mukrasch, M.D., et al., *Highly populated turn conformations in natively unfolded tau protein identified from residual dipolar couplings and molecular simulation.* J Am Chem Soc, 2007. **129**(16): p. 5235-43.
36. Mukrasch, M.D., et al., *Structural polymorphism of 441-residue tau at single residue resolution.* PLoS Biol, 2009. **7**(2): p. e34.
37. Mylonas, E., et al., *Domain conformation of tau protein studied by solution small-angle X-ray scattering.* Biochemistry, 2008. **47**(39): p. 10345-53.

38. Nath, A., et al., *The conformational ensembles of alpha-synuclein and tau: combining single-molecule FRET and simulations.* Biophys J, 2012. **103**(9): p. 1940-9.
39. Bibow, S., et al., *Structural impact of proline-directed pseudophosphorylation at AT8, AT100, and PHF1 epitopes on 441-residue tau.* J Am Chem Soc, 2011. **133**(40): p. 15842-5.
40. Luo, Y., et al., *Structural Insight into Tau Protein's Paradox of Intrinsically Disordered Behavior, Self-Acetylation Activity, and Aggregation.* J Phys Chem Lett, 2014. **5**(17): p. 3026-3031.
41. Wegmann, S., et al., *Competing interactions stabilize pro- and anti-aggregant conformations of human Tau.* J Biol Chem, 2011. **286**(23): p. 20512-24.
42. Jeganathan, S., et al., *Proline-directed pseudo-phosphorylation at AT8 and PHF1 epitopes induces a compaction of the paperclip folding of Tau and generates a pathological (MC-1) conformation.* J Biol Chem, 2008. **283**(46): p. 32066-76.
43. Elbaum-Garfinkle, S. and E. Rhoades, *Identification of an aggregation-prone structure of tau.* J Am Chem Soc, 2012. **134**(40): p. 16607-13.
44. Manger, L.H., et al., *Revealing Conformational Variants of Solution-Phase Intrinsically Disordered Tau Protein at the Single-Molecule Level.* Angew Chem Int Ed Engl, 2017. **56**(49): p. 15584-15588.
45. Foote, A.K., et al., *Time-resolved multirotational dynamics of single solution-phase tau proteins reveals details of conformational variation.* Phys Chem Chem Phys, 2019. **21**(4): p. 1863-1871.
46. Barber, K.W. and J. Rinehart, *The ABCs of PTMs.* Nat Chem Biol, 2018. **14**(3): p. 188-192.
47. Darling, A.L. and V.N. Uversky, *Intrinsic Disorder and Posttranslational Modifications: The Darker Side of the Biological Dark Matter.* Front Genet, 2018. **9**: p. 158.
48. Jeganathan, S., et al., *The natively unfolded character of tau and its aggregation to Alzheimer-like paired helical filaments.* Biochemistry, 2008. **47**(40): p. 10526-39.
49. Uversky, V.N., *Natively unfolded proteins: a point where biology waits for physics.* Protein Sci, 2002. **11**(4): p. 739-56.
50. Park, S., et al., *Degradation or aggregation: the ramifications of post-translational modifications on tau.* BMB Rep, 2018. **51**(6): p. 265-273.
51. Haj-Yahya, M. and H.A. Lashuel, *Protein Semisynthesis Provides Access to Tau Disease-Associated Post-translational Modifications (PTMs) and Paves the Way to Deciphering the Tau PTM Code in Health and Diseased States.* J Am Chem Soc, 2018. **140**(21): p. 6611-6621.
52. Alquezar, C., S. Arya, and A.W. Kao, *Tau Post-translational Modifications: Dynamic Transformers of Tau Function, Degradation, and Aggregation.* Front Neurol, 2020. **11**: p. 595532.
53. Keller, J.N., K.B. Hanni, and W.R. Markesbery, *Impaired proteasome function in Alzheimer's disease.* J Neurochem, 2000. **75**(1): p. 436-9.
54. Reynolds, C.H., et al., *Phosphorylation sites on tau identified by nanoelectrospray mass spectrometry: differences in vitro between the mitogen-activated protein kinases ERK2, c-Jun N-terminal kinase and P38, and glycogen synthase kinase-3beta.* J Neurochem, 2000. **74**(4): p. 1587-95.

55. Lothrop, A.P., M.P. Torres, and S.M. Fuchs, *Deciphering post-translational modification codes.* FEBS Lett, 2013. **587**(8): p. 1247-57.
56. Sacco, F., et al., *The human phosphatase interactome: An intricate family portrait.* FEBS Lett, 2012. **586**(17): p. 2732-9.
57. Humphrey, S.J., D.E. James, and M. Mann, *Protein Phosphorylation: A Major Switch Mechanism for Metabolic Regulation.* Trends Endocrinol Metab, 2015. **26**(12): p. 676-687.
58. Hunter, T., *Protein kinases and phosphatases: the yin and yang of protein phosphorylation and signaling.* Cell, 1995. **80**(2): p. 225-36.
59. Ferrer, I., et al., *Current advances on different kinases involved in tau phosphorylation, and implications in Alzheimer's disease and tauopathies.* Curr Alzheimer Res, 2005. **2**(1): p. 3-18.
60. Ji, C., et al., *BAG3 and SYNPO (synaptopodin) facilitate phospho-MAPT/Tau degradation via autophagy in neuronal processes.* Autophagy, 2019. **15**(7): p. 1199-1213.
61. Hanger, D.P., B.H. Anderton, and W. Noble, *Tau phosphorylation: the therapeutic challenge for neurodegenerative disease.* Trends Mol Med, 2009. **15**(3): p. 112-9.
62. Gong, C.X., et al., *Phosphoprotein phosphatase activities in Alzheimer disease brain.* J Neurochem, 1993. **61**(3): p. 921-7.
63. Braithwaite, S.P., et al., *Protein phosphatases and Alzheimer's disease.* Prog Mol Biol Transl Sci, 2012. **106**: p. 343-79.
64. Wadhwa, P., P. Jain, and H.R. Jadhav, *Glycogen Synthase Kinase 3 (GSK3): Its Role and Inhibitors.* Curr Top Med Chem, 2020. **20**(17): p. 1522-1534.
65. Morishima-Kawashima, M., et al., *Proline-directed and non-proline-directed phosphorylation of PHF-tau.* J Biol Chem, 1995. **270**(2): p. 823-9.
66. Cook, C., et al., *Acetylation: a new key to unlock tau's role in neurodegeneration.* Alzheimers Res Ther, 2014. **6**(3): p. 29.
67. Matsuo, E.S., et al., *Biopsy-derived adult human brain tau is phosphorylated at many of the same sites as Alzheimer's disease paired helical filament tau.* Neuron, 1994. **13**(4): p. 989-1002.
68. Mandelkow, E.M. and E. Mandelkow, *Biochemistry and cell biology of tau protein in neurofibrillary degeneration.* Cold Spring Harb Perspect Med, 2012. **2**(7): p. a006247.
69. Yu, Y., et al., *Developmental regulation of tau phosphorylation, tau kinases, and tau phosphatases.* J Neurochem, 2009. **108**(6): p. 1480-94.
70. Hernandez, F., et al., *GSK-3 dependent phosphoepitopes recognized by PHF-1 and AT-8 antibodies are present in different tau isoforms.* Neurobiol Aging, 2003. **24**(8): p. 1087-94.
71. Li, T., et al., *Cyclin-dependent protein kinase 5 primes microtubule-associated protein tau site-specifically for glycogen synthase kinase 3beta.* Biochemistry, 2006. **45**(10): p. 3134-45.
72. Kimura, T., K. Ishiguro, and S. Hisanaga, *Physiological and pathological phosphorylation of tau by Cdk5.* Front Mol Neurosci, 2014. **7**: p. 65.
73. Lee, V.M., M. Goedert, and J.Q. Trojanowski, *Neurodegenerative tauopathies.* Annu Rev Neurosci, 2001. **24**: p. 1121-59.
74. Mair, W., et al., *FLEXITau: Quantifying Post-translational Modifications of Tau Protein in Vitro and in Human Disease.* Anal Chem, 2016. **88**(7): p. 3704-14.
75. Sato, C., et al., *Tau Kinetics in Neurons and the Human Central Nervous System.* Neuron, 2018. **97**(6): p. 1284-1298 e7.

76. Wesseling, H., et al., *Tau PTM Profiles Identify Patient Heterogeneity and Stages of Alzheimer's Disease.* Cell, 2020. **183**(6): p. 1699-1713 e13.
77. Braak, H. and E. Braak, *Staging of Alzheimer's disease-related neurofibrillary changes.* Neurobiol Aging, 1995. **16**(3): p. 271-8; discussion 278-84.
78. Fitzpatrick, A.W. and H.R. Saibil, *Cryo-EM of amyloid fibrils and cellular aggregates.* Curr Opin Struct Biol, 2019. **58**: p. 34-42.
79. Scheres, S.H., et al., *Cryo-EM structures of tau filaments.* Curr Opin Struct Biol, 2020. **64**: p. 17-25.
80. Fitzpatrick, A.W.P., et al., *Cryo-EM structures of tau filaments from Alzheimer's disease.* Nature, 2017. **547**(7662): p. 185-190.
81. Falcon, B., et al., *Structures of filaments from Pick's disease reveal a novel tau protein fold.* Nature, 2018. **561**(7721): p. 137-140.
82. Goedert, M. and M.G. Spillantini, *Propagation of Tau aggregates.* Mol Brain, 2017. **10**(1): p. 18.
83. Wang, Y. and E. Mandelkow, *Tau in physiology and pathology.* Nat Rev Neurosci, 2016. **17**(1): p. 5-21.
84. Zhou, X.W., et al., *Assessments of the accumulation severities of amyloid beta-protein and hyperphosphorylated tau in the medial temporal cortex of control and Alzheimer's brains.* Neurobiol Dis, 2006. **22**(3): p. 657-68.
85. Neddens, J., et al., *Phosphorylation of different tau sites during progression of Alzheimer's disease.* Acta Neuropathol Commun, 2018. **6**(1): p. 52.
86. Rankin, C.A., Q. Sun, and T.C. Gamblin, *Pseudo-phosphorylation of tau at Ser202 and Thr205 affects tau filament formation.* Brain Res Mol Brain Res, 2005. **138**(1): p. 84-93.
87. Akhmanova, A. and L.C. Kapitein, *Mechanisms of microtubule organization in differentiated animal cells.* Nat Rev Mol Cell Biol, 2022. **23**(8): p. 541-558.
88. Desai, A. and T.J. Mitchison, *Microtubule polymerization dynamics.* Annu Rev Cell Dev Biol, 1997. **13**: p. 83-117.
89. Brouhard, G.J. and L.M. Rice, *Microtubule dynamics: an interplay of biochemistry and mechanics.* Nat Rev Mol Cell Biol, 2018. **19**(7): p. 451-463.
90. Gudimchuk, N.B. and J.R. McIntosh, *Regulation of microtubule dynamics, mechanics and function through the growing tip.* Nat Rev Mol Cell Biol, 2021. **22**(12): p. 777-795.
91. Hirokawa, N. and R. Takemura, *Molecular motors and mechanisms of directional transport in neurons.* Nat Rev Neurosci, 2005. **6**(3): p. 201-14.
92. Alushin, G.M., et al., *High-resolution microtubule structures reveal the structural transitions in alphabeta-tubulin upon GTP hydrolysis.* Cell, 2014. **157**(5): p. 1117-29.
93. Zhang, R., et al., *Mechanistic Origin of Microtubule Dynamic Instability and Its Modulation by EB Proteins.* Cell, 2015. **162**(4): p. 849-59.
94. Mandelkow, E.M., E. Mandelkow, and R.A. Milligan, *Microtubule dynamics and microtubule caps: a time-resolved cryo-electron microscopy study.* J Cell Biol, 1991. **114**(5): p. 977-91.
95. Muller-Reichert, T., et al., *Structural changes at microtubule ends accompanying GTP hydrolysis: information from a slowly hydrolyzable analogue of GTP, guanylyl (alpha,beta)methylenediphosphonate.* Proc Natl Acad Sci U S A, 1998. **95**(7): p. 3661-6.

96. Chretien, D., S.D. Fuller, and E. Karsenti, *Structure of growing microtubule ends: two-dimensional sheets close into tubes at variable rates.* J Cell Biol, 1995. **129**(5): p. 1311-28.
97. Buey, R.M., J.F. Diaz, and J.M. Andreu, *The nucleotide switch of tubulin and microtubule assembly: a polymerization-driven structural change.* Biochemistry, 2006. **45**(19): p. 5933-8.
98. Rice, L.M., E.A. Montabana, and D.A. Agard, *The lattice as allosteric effector: structural studies of alphabeta- and gamma-tubulin clarify the role of GTP in microtubule assembly.* Proc Natl Acad Sci U S A, 2008. **105**(14): p. 5378-83.
99. Nawrotek, A., M. Knossow, and B. Gigant, *The determinants that govern microtubule assembly from the atomic structure of GTP-tubulin.* J Mol Biol, 2011. **412**(1): p. 35-42.
100. Ayaz, P., et al., *A tethered delivery mechanism explains the catalytic action of a microtubule polymerase.* Elife, 2014. **3**: p. e03069.
101. Pecqueur, L., et al., *A designed ankyrin repeat protein selected to bind to tubulin caps the microtubule plus end.* Proc Natl Acad Sci U S A, 2012. **109**(30): p. 12011-6.
102. Estevez-Gallego, J., et al., *Structural model for differential cap maturation at growing microtubule ends.* Elife, 2020. **9**.
103. Cleary, J.M. and W.O. Hancock, *Molecular mechanisms underlying microtubule growth dynamics.* Curr Biol, 2021. **31**(10): p. R560-R573.
104. Mitchison, T. and M. Kirschner, *Dynamic instability of microtubule growth.* Nature, 1984. **312**(5991): p. 237-42.
105. Roostalu, J. and T. Surrey, *Microtubule nucleation: beyond the template.* Nat Rev Mol Cell Biol, 2017. **18**(11): p. 702-710.
106. Vemu, A., et al., *Severing enzymes amplify microtubule arrays through lattice GTP-tubulin incorporation.* Science, 2018. **361**(6404).
107. Kuo, Y.W., et al., *Spastin is a dual-function enzyme that severs microtubules and promotes their regrowth to increase the number and mass of microtubules.* Proc Natl Acad Sci U S A, 2019. **116**(12): p. 5533-5541.
108. Kuo, Y.W. and J. Howard, *Cutting, Amplifying, and Aligning Microtubules with Severing Enzymes.* Trends Cell Biol, 2021. **31**(1): p. 50-61.
109. Jiang, K., et al., *Microtubule minus-end regulation at spindle poles by an ASPM-katanin complex.* Nat Cell Biol, 2017. **19**(5): p. 480-492.
110. Jiang, K., et al., *Microtubule minus-end stabilization by polymerization-driven CAMSAP deposition.* Dev Cell, 2014. **28**(3): p. 295-309.
111. Sinsky, J., et al., *Physiological Tau Interactome in Brain and Its Link to Tauopathies.* Journal of Proteome Research, 2020. **19**(6): p. 2429-2442.
112. Kampers, T., et al., *RNA stimulates aggregation of microtubule-associated protein tau into Alzheimer-like paired helical filaments.* FEBS Lett, 1996. **399**(3): p. 344-9.
113. Krylova, S.M., et al., *Tau protein binds single-stranded DNA sequence specifically--the proof obtained in vitro with non-equilibrium capillary electrophoresis of equilibrium mixtures.* FEBS Lett, 2005. **579**(6): p. 1371-5.
114. Sultan, A., et al., *Nuclear tau, a key player in neuronal DNA protection.* J Biol Chem, 2011. **286**(6): p. 4566-75.

115. Brandt, R., J. Leger, and G. Lee, *Interaction of tau with the neural plasma membrane mediated by tau's amino-terminal projection domain.* J Cell Biol, 1995. **131**(5): p. 1327-40.
116. Meier, S., et al., *Identification of Novel Tau Interactions with Endoplasmic Reticulum Proteins in Alzheimer's Disease Brain.* J Alzheimers Dis, 2015. **48**(3): p. 687-702.
117. Farah, C.A., et al., *Tau interacts with Golgi membranes and mediates their association with microtubules.* Cell Motil Cytoskeleton, 2006. **63**(11): p. 710-24.
118. Noble, W., et al., *The importance of tau phosphorylation for neurodegenerative diseases.* Front Neurol, 2013. **4**: p. 83.
119. Dawson, H.N., et al., *Inhibition of neuronal maturation in primary hippocampal neurons from tau deficient mice.* J Cell Sci, 2001. **114**(Pt 6): p. 1179-87.
120. Zuo, Y.C., et al., *Overexpression of Tau Rescues Nogo-66-Induced Neurite Outgrowth Inhibition In Vitro.* Neurosci Bull, 2016. **32**(6): p. 577-584.
121. Spittaels, K., et al., *Glycogen synthase kinase-3beta phosphorylates protein tau and rescues the axonopathy in the central nervous system of human four-repeat tau transgenic mice.* J Biol Chem, 2000. **275**(52): p. 41340-9.
122. Tatebayashi, Y., et al., *Role of tau phosphorylation by glycogen synthase kinase-3beta in the regulation of organelle transport.* J Cell Sci, 2004. **117**(Pt 9): p. 1653-63.
123. Dixit, R., et al., *Differential regulation of dynein and kinesin motor proteins by tau.* Science, 2008. **319**(5866): p. 1086-9.
124. Merino-Serrais, P., et al., *The influence of phospho-tau on dendritic spines of cortical pyramidal neurons in patients with Alzheimer's disease.* Brain, 2013. **136**(Pt 6): p. 1913-28.
125. Konzack, S., et al., *Swimming against the tide: mobility of the microtubule-associated protein tau in neurons.* J Neurosci, 2007. **27**(37): p. 9916-27.
126. Janning, D., et al., *Single-molecule tracking of tau reveals fast kiss-and-hop interaction with microtubules in living neurons.* Mol Biol Cell, 2014. **25**(22): p. 3541-51.
127. Baas, P.W. and L. Qiang, *Tau: It's Not What You Think.* Trends Cell Biol, 2019. **29**(6): p. 452-461.
128. Lee, G., R.L. Neve, and K.S. Kosik, *The microtubule binding domain of tau protein.* Neuron, 1989. **2**(6): p. 1615-24.
129. Goedert, M., et al., *Cloning and sequencing of the cDNA encoding an isoform of microtubule-associated protein tau containing four tandem repeats: differential expression of tau protein mRNAs in human brain.* EMBO J, 1989. **8**(2): p. 393-9.
130. Himmler, A., *Structure of the bovine tau gene: alternatively spliced transcripts generate a protein family.* Molecular and Cellular Biology, 1989. **9**(4): p. 1389-1396.
131. Li, X.H. and E. Rhoades, *Heterogeneous Tau-Tubulin Complexes Accelerate Microtubule Polymerization.* Biophys J, 2017. **112**(12): p. 2567-2574.
132. Goode, B.L. and S.C. Feinstein, *Identification of a novel microtubule binding and assembly domain in the developmentally regulated inter-repeat region of tau.* J Cell Biol, 1994. **124**(5): p. 769-82.
133. Nogales, E., et al., *High-resolution model of the microtubule.* Cell, 1999. **96**(1): p. 79-88.
134. Okada, Y. and N. Hirokawa, *Mechanism of the single-headed processivity: diffusional anchoring between the K-loop of kinesin and the C terminus of tubulin.* Proc Natl Acad Sci U S A, 2000. **97**(2): p. 640-5.

135. Kellogg, E.H., et al., *Near-atomic model of microtubule-tau interactions.* Science, 2018. **360**(6394): p. 1242-1246.
136. Niewidok, B., et al., *Presence of a carboxy-terminal pseudorepeat and disease-like pseudohyperphosphorylation critically influence tau's interaction with microtubules in axon-like processes.* Mol Biol Cell, 2016. **27**(22): p. 3537-3549.
137. Kadavath, H., et al., *Tau stabilizes microtubules by binding at the interface between tubulin heterodimers.* Proc Natl Acad Sci U S A, 2015. **112**(24): p. 7501-6.
138. Fauquant, C., et al., *Systematic identification of tubulin-interacting fragments of the microtubule-associated protein Tau leads to a highly efficient promoter of microtubule assembly.* J Biol Chem, 2011. **286**(38): p. 33358-68.
139. Trinczek, B., et al., *Domains of tau protein, differential phosphorylation, and dynamic instability of microtubules.* Mol Biol Cell, 1995. **6**(12): p. 1887-902.
140. Gustke, N., et al., *Domains of tau protein and interactions with microtubules.* Biochemistry, 1994. **33**(32): p. 9511-22.
141. McKibben, K.M. and E. Rhoades, *Independent tubulin binding and polymerization by the proline-rich region of Tau is regulated by Tau's N-terminal domain.* J Biol Chem, 2019. **294**(50): p. 19381-19394.
142. Chung, P.J., et al., *Direct force measurements reveal that protein Tau confers short-range attractions and isoform-dependent steric stabilization to microtubules.* Proc Natl Acad Sci U S A, 2015. **112**(47): p. E6416-25.
143. Charafeddine, R.A., et al., *Tau repeat regions contain conserved histidine residues that modulate microtubule-binding in response to changes in pH.* J Biol Chem, 2019. **294**(22): p. 8779-8790.
144. Cohen, T.J., et al., *The acetylation of tau inhibits its function and promotes pathological tau aggregation.* Nat Commun, 2011. **2**: p. 252.
145. Reynolds, M.R., et al., *Tau nitration occurs at tyrosine 29 in the fibrillar lesions of Alzheimer's disease and other tauopathies.* J Neurosci, 2006. **26**(42): p. 10636-45.
146. Trzeciakiewicz, H., et al., *A Dual Pathogenic Mechanism Links Tau Acetylation to Sporadic Tauopathy.* Sci Rep, 2017. **7**: p. 44102.
147. Biernat, J. and E.M. Mandelkow, *The development of cell processes induced by tau protein requires phosphorylation of serine 262 and 356 in the repeat domain and is inhibited by phosphorylation in the proline-rich domains.* Mol Biol Cell, 1999. **10**(3): p. 727-40.
148. Drewes, G., et al., *Microtubule-associated protein/microtubule affinity-regulating kinase (p110mark). A novel protein kinase that regulates tau-microtubule interactions and dynamic instability by phosphorylation at the Alzheimer-specific site serine 262.* J Biol Chem, 1995. **270**(13): p. 7679-88.
149. Biernat, J., et al., *Phosphorylation of Ser262 strongly reduces binding of tau to microtubules: distinction between PHF-like immunoreactivity and microtubule binding.* Neuron, 1993. **11**(1): p. 153-63.
150. Brandt, R., et al., *Differential effect of phosphorylation and substrate modulation on tau's ability to promote microtubule growth and nucleation.* J Biol Chem, 1994. **269**(16): p. 11776-82.
151. Sillen, A., et al., *NMR investigation of the interaction between the neuronal protein tau and the microtubules.* Biochemistry, 2007. **46**(11): p. 3055-64.

152. EidenmÜLler, J., et al., *Phosphorylation-mimicking glutamate clusters in the proline-rich region are sufficient to simulate the functional deficiencies of hyperphosphorylated tau protein.* Biochemical Journal, 2001. **357**(3): p. 759-767.
153. Cho, J.H. and G.V. Johnson, *Glycogen synthase kinase 3beta phosphorylates tau at both primed and unprimed sites. Differential impact on microtubule binding.* J Biol Chem, 2003. **278**(1): p. 187-93.
154. Hasegawa, M., et al., *Characterization of mAb AP422, a novel phosphorylation-dependent monoclonal antibody against tau protein.* FEBS Lett, 1996. **384**(1): p. 25-30.
155. Haase, C., et al., *Pseudophosphorylation of tau protein alters its ability for self-aggregation.* J Neurochem, 2004. **88**(6): p. 1509-20.
156. Drubin, D.G. and M.W. Kirschner, *Tau protein function in living cells.* J Cell Biol, 1986. **103**(6 Pt 2): p. 2739-46.
157. Melo, A.M., et al., *A functional role for intrinsic disorder in the tau-tubulin complex.* Proc Natl Acad Sci U S A, 2016. **113**(50): p. 14336-14341.
158. Fung, H.Y.J., et al., *Structural Characterization of Tau in Fuzzy Tau:Tubulin Complexes.* Structure, 2020. **28**(3): p. 378-384 e4.
159. Mukrasch, M.D., et al., *The "jaws" of the tau-microtubule interaction.* J Biol Chem, 2007. **282**(16): p. 12230-9.
160. Butner, K.A. and M.W. Kirschner, *Tau protein binds to microtubules through a flexible array of distributed weak sites.* J Cell Biol, 1991. **115**(3): p. 717-30.
161. Zhang, W., et al., *Novel tau filament fold in corticobasal degeneration.* Nature, 2020. **580**(7802): p. 283-287.
162. Arendt, T., J.T. Stieler, and M. Holzer, *Tau and tauopathies.* Brain Res Bull, 2016. **126**(Pt 3): p. 238-292.
163. Guo, T., W. Noble, and D.P. Hanger, *Roles of tau protein in health and disease.* Acta Neuropathol, 2017. **133**(5): p. 665-704.
164. Ballatore, C., V.M. Lee, and J.Q. Trojanowski, *Tau-mediated neurodegeneration in Alzheimer's disease and related disorders.* Nat Rev Neurosci, 2007. **8**(9): p. 663-72.
165. Winklhofer, K.F., J. Tatzelt, and C. Haass, *The two faces of protein misfolding: gain- and loss-of-function in neurodegenerative diseases.* EMBO J, 2008. **27**(2): p. 336-49.
166. Martinez-Moro, M., D. Di Silvio, and S.E. Moya, *Fluorescence correlation spectroscopy as a tool for the study of the intracellular dynamics and biological fate of protein corona.* Biophys Chem, 2019. **253**: p. 106218.
167. Elson, E.L. and D. Magde, *Fluorescence correlation spectroscopy. I. Conceptual basis and theory.* Biopolymers, 2004. **13**(1): p. 1-27.
168. Tan, R., et al., *Microtubules gate tau condensation to spatially regulate microtubule functions.* Nat Cell Biol, 2019. **21**(9): p. 1078-1085.
169. Melo, A.M., S. Elbaum-Garfinkle, and E. Rhoades, *Insights into tau function and dysfunction through single-molecule fluorescence.* Methods Cell Biol, 2017. **141**: p. 27-44.
170. Wickramasinghe, S.P. and E. Rhoades, *Measuring Interactions Between Tau and Aggregation Inducers with Single-Molecule Forster Resonance Energy Transfer.* Methods Mol Biol, 2020. **2141**: p. 755-775.
171. Stryer, L. and R.P. Haugland, *Energy transfer: a spectroscopic ruler.* Proc Natl Acad Sci U S A, 1967. **58**(2): p. 719-26.

172. Hendrix, J. and D.C. Lamb, *Pulsed interleaved excitation: principles and applications.* Methods Enzymol, 2013. **518**: p. 205-43.
173. Schuler, B., *Single-molecule FRET of protein structure and dynamics - a primer.* J Nanobiotechnology, 2013. **11 Suppl 1**(Suppl 1): p. S2.
174. Goode, B.L., et al., *Functional interactions between the proline-rich and repeat regions of tau enhance microtubule binding and assembly.* Mol Biol Cell, 1997. **8**(2): p. 353-65.
175. Weissmann, C., et al., *Microtubule binding and trapping at the tip of neurites regulate tau motion in living neurons.* Traffic, 2009. **10**(11): p. 1655-68.
176. Duan, A.R., et al., *Interactions between Tau and Different Conformations of Tubulin: Implications for Tau Function and Mechanism.* J Mol Biol, 2017. **429**(9): p. 1424-1438.
177. Castle, B.T., et al., *Tau Avoids the GTP Cap at Growing Microtubule Plus-Ends.* iScience, 2020. **23**(12): p. 101782.
178. Maurer, S.P., et al., *EBs recognize a nucleotide-dependent structural cap at growing microtubule ends.* Cell, 2012. **149**(2): p. 371-82.
179. Zanic, M., et al., *EB1 recognizes the nucleotide state of tubulin in the microtubule lattice.* PLoS One, 2009. **4**(10): p. e7585.
180. Bechstedt, S., K. Lu, and G.J. Brouhard, *Doublecortin recognizes the longitudinal curvature of the microtubule end and lattice.* Curr Biol, 2014. **24**(20): p. 2366-75.
181. Folker, E.S., B.M. Baker, and H.V. Goodson, *Interactions between CLIP-170, tubulin, and microtubules: implications for the mechanism of Clip-170 plus-end tracking behavior.* Mol Biol Cell, 2005. **16**(11): p. 5373-84.
182. Samsonov, A., et al., *Tau interaction with microtubules in vivo.* J Cell Sci, 2004. **117**(Pt 25): p. 6129-41.
183. Brion, J.P., J.N. Octave, and A.M. Couck, *Distribution of the phosphorylated microtubule-associated protein tau in developing cortical neurons.* Neuroscience, 1994. **63**(3): p. 895-909.
184. Kenessey, A. and S.H. Yen, *The extent of phosphorylation of fetal tau is comparable to that of PHF-tau from Alzheimer paired helical filaments.* Brain Res, 1993. **629**(1): p. 40-6.
185. Arendt, T., et al., *Reversible paired helical filament-like phosphorylation of tau is an adaptive process associated with neuronal plasticity in hibernating animals.* J Neurosci, 2003. **23**(18): p. 6972-81.
186. Guisle, I., et al., *Circadian and sleep/wake-dependent variations in tau phosphorylation are driven by temperature.* Sleep, 2020. **43**(4).
187. Wickramasinghe, S.P., et al., *Polyphosphate Initiates Tau Aggregation through Intra- and Intermolecular Scaffolding.* Biophys J, 2019. **117**(4): p. 717-728.
188. Englander, J.J., J.R. Rogero, and S.W. Englander, *Protein hydrogen exchange studied by the fragment separation method.* Anal Biochem, 1985. **147**(1): p. 234-44.
189. Chalmers, M.J., et al., *Differential hydrogen/deuterium exchange mass spectrometry analysis of protein-ligand interactions.* Expert Rev Proteomics, 2011. **8**(1): p. 43-59.
190. Dunker, A.K., et al., *Intrinsically disordered protein.* J Mol Graph Model, 2001. **19**(1): p. 26-59.
191. Stepniak, D., et al., *Highly efficient gluten degradation with a newly identified prolyl endoprotease: implications for celiac disease.* Am J Physiol Gastrointest Liver Physiol, 2006. **291**(4): p. G621-9.

192. Salden, B.N., et al., *Randomised clinical study: Aspergillus niger-derived enzyme digests gluten in the stomach of healthy volunteers.* Aliment Pharmacol Ther, 2015. **42**(3): p. 273-85.
193. Tack, G.J., et al., *Consumption of gluten with gluten-degrading enzyme by celiac patients: a pilot-study.* World J Gastroenterol, 2013. **19**(35): p. 5837-47.
194. Janssen, G., et al., *Ineffective degradation of immunogenic gluten epitopes by currently available digestive enzyme supplements.* PLoS One, 2015. **10**(6): p. e0128065.
195. Sebela, M., et al., *Identification of N-glycosylation in prolyl endoprotease from Aspergillus niger and evaluation of the enzyme for its possible application in proteomics.* J Mass Spectrom, 2009. **44**(11): p. 1587-95.
196. Tsiatsiani, L., et al., *Aspergillus niger Prolyl Endoprotease for Hydrogen-Deuterium Exchange Mass Spectrometry and Protein Structural Studies.* Anal Chem, 2017. **89**(15): p. 7966-7973.
197. Zhu, S., et al., *Hyperphosphorylation of intrinsically disordered tau protein induces an amyloidogenic shift in its conformational ensemble.* PLoS One, 2015. **10**(3): p. e0120416.
198. Beveridge, R., et al., *Mass spectrometry locates local and allosteric conformational changes that occur on cofactor binding.* Nat Commun, 2016. **7**: p. 12163.
199. Davey, N.E., et al., *Attributes of short linear motifs.* Mol Biosyst, 2012. **8**(1): p. 268-81.
200. Sinz, A., et al., *Chemical cross-linking and native mass spectrometry: A fruitful combination for structural biology.* Protein Sci, 2015. **24**(8): p. 1193-209.
201. Leitner, A., et al., *Crosslinking and Mass Spectrometry: An Integrated Technology to Understand the Structure and Function of Molecular Machines.* Trends Biochem Sci, 2016. **41**(1): p. 20-32.
202. Orban-Nemeth, Z., et al., *Structural prediction of protein models using distance restraints derived from cross-linking mass spectrometry data.* Nat Protoc, 2018. **13**(3): p. 478-494.
203. Kalkhof, S. and A. Sinz, *Chances and pitfalls of chemical cross-linking with amine-reactive N-hydroxysuccinimide esters.* Anal Bioanal Chem, 2008. **392**(1-2): p. 305-12.
204. Madler, S., et al., *Chemical cross-linking with NHS esters: a systematic study on amino acid reactivities.* J Mass Spectrom, 2009. **44**(5): p. 694-706.
205. Leitner, A., et al., *Expanding the chemical cross-linking toolbox by the use of multiple proteases and enrichment by size exclusion chromatography.* Mol Cell Proteomics, 2012. **11**(3): p. M111 014126.
206. Gotze, M., et al., *Automated assignment of MS/MS cleavable cross-links in protein 3D-structure analysis.* J Am Soc Mass Spectrom, 2015. **26**(1): p. 83-97.
207. Iacobucci, C., et al., *A cross-linking/mass spectrometry workflow based on MS-cleavable cross-linkers and the MeroX software for studying protein structures and protein-protein interactions.* Nat Protoc, 2018. **13**(12): p. 2864-2889.
208. Schneider, M., A. Belsom, and J. Rappsilber, *Protein Tertiary Structure by Crosslinking/Mass Spectrometry.* Trends Biochem Sci, 2018. **43**(3): p. 157-169.
209. Chavez, J.D. and J.E. Bruce, *Chemical cross-linking with mass spectrometry: a tool for systems structural biology.* Curr Opin Chem Biol, 2019. **48**: p. 8-18.
210. Iacobucci, C., M. Gotze, and A. Sinz, *Cross-linking/mass spectrometry to get a closer view on protein interaction networks.* Curr Opin Biotechnol, 2020. **63**: p. 48-53.
211. Nash, P., et al., *Multisite phosphorylation of a CDK inhibitor sets a threshold for the onset of DNA replication.* Nature, 2001. **414**(6863): p. 514-21.

212. Graham, M., et al., *xiView: A common platform for the downstream analysis of Crosslinking Mass Spectrometry data.* 2019.
213. Pettersen, E.F., et al., *UCSF ChimeraX: Structure visualization for researchers, educators, and developers.* Protein Sci, 2021. **30**(1): p. 70-82.
214. Iacobucci, C., et al., *First Community-Wide, Comparative Cross-Linking Mass Spectrometry Study.* Anal Chem, 2019. **91**(11): p. 6953-6961.
215. Ding, Y.H., et al., *Modeling Protein Excited-state Structures from "Over-length" Chemical Cross-links.* J Biol Chem, 2017. **292**(4): p. 1187-1196.
216. Webb, B., et al., *Integrative structure modeling with the Integrative Modeling Platform.* Protein Sci, 2018. **27**(1): p. 245-258.
217. Degiacomi, M.T., et al., *Accommodating Protein Dynamics in the Modeling of Chemical Crosslinks.* Structure, 2017. **25**(11): p. 1751-1757 e5.
218. Calabrese, A.N., et al., *Inter-domain dynamics in the chaperone SurA and multi-site binding to its outer membrane protein clients.* Nat Commun, 2020. **11**(1): p. 2155.
219. Bullock, J.M.A., K. Thalassinos, and M. Topf, *Jwalk and MNXL web server: model validation using restraints from crosslinking mass spectrometry.* Bioinformatics, 2018. **34**(20): p. 3584-3585.
220. Popov, K.I., et al., *Insight into the Structure of the "Unstructured" Tau Protein.* Structure, 2019. **27**(11): p. 1710-1715 e4.
221. Narayanan, R.L., et al., *Automatic assignment of the intrinsically disordered protein Tau with 441-residues.* J Am Chem Soc, 2010. **132**(34): p. 11906-7.
222. Elbaum-Garfinkle, S., et al., *Tau mutants bind tubulin heterodimers with enhanced affinity.* Proc Natl Acad Sci U S A, 2014. **111**(17): p. 6311-6.
223. Rosenberg, K.J., et al., *Complementary dimerization of microtubule-associated tau protein: Implications for microtubule bundling and tau-mediated pathogenesis.* Proceedings of the National Academy of Sciences, 2008. **105**(21): p. 7445-7450.
224. Chen, J., et al., *Projection domains of MAP2 and tau determine spacings between microtubules in dendrites and axons.* Nature, 1992. **360**(6405): p. 674-677.
225. Mukhopadhyay, R. and J.H. Hoh, *AFM force measurements on microtubule-associated proteins: the projection domain exerts a long-range repulsive force.* FEBS Letters, 2001. **505**(3): p. 374-378.
226. Donhauser, Z.J., et al., *Dimerization and Long-Range Repulsion Established by Both Termini of the Microtubule-Associated Protein Tau.* Biochemistry, 2017. **56**(44): p. 5900-5909.
227. Preuss, U., et al., *The 'jaws' model of tau-microtubule interaction examined in CHO cells.* Journal of Cell Science, 1997. **110**(6): p. 789-800.
228. Tompa, P. and M. Fuxreiter, *Fuzzy complexes: polymorphism and structural disorder in protein–protein interactions.* Trends in Biochemical Sciences, 2008. **33**(1): p. 2-8.
229. Santarella, R.A., et al., *Surface-decoration of microtubules by human tau.* J Mol Biol, 2004. **339**(3): p. 539-53.
230. McIntosh, J.R., et al., *Tubulin depolymerization may be an ancient biological motor.* Journal of Cell Science, 2010. **123**(20): p. 3425-3434.
231. Sept, D., N.A. Baker, and J.A. McCammon, *The physical basis of microtubule structure and stability.* Protein Sci, 2003. **12**(10): p. 2257-61.

232. Castoldi, M. and A.V. Popov, *Purification of brain tubulin through two cycles of polymerization-depolymerization in a high-molarity buffer.* Protein Expr Purif, 2003. **32**(1): p. 83-8.
233. Hirst, W.G., et al., *In Vitro Reconstitution and Imaging of Microtubule Dynamics by Fluorescence and Label-free Microscopy.* STAR Protoc, 2020. **1**(3): p. 100177.
234. Lo, C.H., et al., *Targeting the ensemble of heterogeneous tau oligomers in cells: A novel small molecule screening platform for tauopathies.* Alzheimers Dement, 2019. **15**(11): p. 1489-1502.
235. Schiff, P.B., J. Fant, and S.B. Horwitz, *Promotion of microtubule assembly in vitro by taxol.* Nature, 1979. **277**(5698): p. 665-667.
236. Jijumon, A.S., et al., *Lysate-based pipeline to characterize microtubule-associated proteins uncovers unique microtubule behaviours.* Nat Cell Biol, 2022. **24**(2): p. 253-267.
237. Kan, Z.Y., et al., *ExMS2: An Integrated Solution for Hydrogen-Deuterium Exchange Mass Spectrometry Data Analysis.* Anal Chem, 2019. **91**(11): p. 7474-7481.
238. Masson, G.R., et al., *Recommendations for performing, interpreting and reporting hydrogen deuterium exchange mass spectrometry (HDX-MS) experiments.* Nat Methods, 2019. **16**(7): p. 595-602.
239. Slavin, M. and N. Kalisman, *Structural Analysis of Protein Complexes by Cross-Linking and Mass Spectrometry*, in *Protein Complex Assembly: Methods and Protocols*, J.A. Marsh, Editor. 2018, Springer New York: New York, NY. p. 173-183.
240. Hulstaert, N., et al., *ThermoRawFileParser: Modular, Scalable, and Cross-Platform RAW File Conversion.* J Proteome Res, 2020. **19**(1): p. 537-542.